Adv. Manuf. (2025) 13:105–154
https://doi.org/10.1007/s40436-024-00508-x

High-speed grinding: from mechanism to machine tool

Yu-Long Wang[1] · Yan-Bin Zhang[1] · Xin Cui[1] · Xiao-Liang Liang[2] · Run-Ze Li[3] · Ruo-Xin Wang[4] · Shubham Sharma[5] · Ming-Zheng Liu[1] · Teng Gao[1] · Zong-Ming Zhou[6] · Xiao-Ming Wang[1] · Yusuf Suleiman Dambatta[1,7] · Chang-He Li[1]

Received: 26 October 2023 / Revised: 11 December 2023 / Accepted: 24 April 2024 / Published online: 5 October 2024

Abstract High-speed grinding (HSG) is an advanced technology for precision machining of difficult-to-cut materials in aerospace and other fields, which could solve surface burns, defects and improve surface integrity by increasing the linear speed of the grinding wheel. The advantages of HSG have been preliminarily confirmed and the equipment has been built for experimental research, which can achieve a high grinding speed of more than 300 m/s. However, it is not yet widely used in manufacturing due to the insufficient understanding on material removal mechanism and characteristics of HSG machine tool. To fill this gap, this paper provides a comprehensive overview of HSG technologies. A new direction for adding auxiliary process in HSG is proposed. Firstly, the combined influence law of strain hardening, strain rate intensification, and thermal softening effects on material removal mechanism was revealed, and models of material removal strain rate, grinding force and grinding temperature were summarized. Secondly, the constitutive models under high strain rate boundaries were summarized by considering various properties of material and grinding parameters. Thirdly, the change law of material removal mechanism of HSG was revealed when the thermodynamic boundary conditions changed, by introducing lubrication conditions such as minimum quantity lubrication (MQL), nano-lubricant minimum quantity lubrication (NMQL) and cryogenic air (CA). Finally, the mechanical and dynamic characteristics of the key components of HSG machine tool were summarized, including main body, grinding wheel, spindle and dynamic balance system. Based on the content summarized in this paper, the prospect of HSG is put forward. This study establishes a solid foundation for future developments in the field and points to promising directions for further exploration.

Keywords High speed grinding (HSG) · Material removal mechanism · Typical material · Lubrication methods · Machine tool

List of symbols

CBN	Cubic boron nitride
q_t	Total heat flux
q_s	Heat flux into the grinding wheel

✉ Chang-He Li
sy_lichanghe@163.com

Yan-Bin Zhang
Zhangyanbin1_QDLG@163.com

[1] School of Mechanical and Automotive Engineering, Qingdao University of Technology, Qingdao 266520, Shandong, People's Republic of China

[2] Key Laboratory of High Efficiency and Clean Mechanical Manufacture of MOE, School of Mechanical Engineering, Shandong University, Jinan 250061, People's Republic of China

[3] Department of Mechanical Engineering, Massachusetts Institute of Technology, Cambridge, MA, USA

[4] State Key Laboratory of Ultra-precision Machining Technology, Department of Industrial and Systems Engineering, The Hong Kong Polytechnic University, Hong Kong, People's Republic of China

[5] Department of Mechanical Engineering and Advanced Materials Science, Council of Scientific and Industrial Research (CSIR)-Central Leather Research Institute (CLRI), Regional Center for Extension and Development, Jalandhar 144021, India

[6] Hanergy (Qingdao) Lubrication Technology Co., Ltd., Qingdao 266200, Shandong, People's Republic of China

[7] Department of Mechanical Engineering, Ahmadu Bello University, Zaria, Nigeria

P_i	Effective input power
v_s	Peripheral speed of grinding wheel
S_v	Cross section area of debris
HSG	High-speed grinding
U_0	Initial unevenness measure
MQL	Minimum quantity lubrication
NMQL	Nano-lubricant minimum quantity lubrication
MoS_2	Molybdenum disulfide
φ	The shearing angle
β_f	Frictional angle
F_s	Material fracture force
F_r	Resultant force of material
Σ_{b1}	Breaking limit
γ_0	Rake angle
γ	Strain
$\dot{\gamma}$	Strain rate
F_f	Friction force
F_n	Squeezing force
P^*	Dimensionless pressure
T^*	Maximum dimensionless tensile strength
K	Heat conductivity
F_{gts}	Frictional tangential grinding force of a single abrasive
τ_f	Frictional stress
σ_n	Positive stress on the contact surface
F_{gt}	Tangential grinding force of a single abrasive
F_{gtc}	Single abrasive cutting deformation tangential grinding force
σ^*_{gmax}	Dimensionless breaking strength of materials
$a_{g\,max}$	Maximum undeformed chip thickness
$\overline{A_g}$	Average grinding layer area
β_w	Thermal contact factor
r_0	Effective contact radius of abrasives
l_i	Heat source curves
d_e	Equivalent diameter
e_s	Specific grinding energy
e_{sl}	Specific grazing energy
$\dot{\varepsilon}^*$	Dimensionless strain rate
$\dot{\varepsilon}_0$	Reference strain rate
P	Actual pressure
σ^*_{fmax}	Dimensionless fracture strength
q_w	Heat flux into the workpiece
q_{ch}	Heat flux into the chip
q_f	Heat flux into the coolant
v_w	Feed speed
a_p	Grinding depth
μ	Friction coefficient
α	Swing angle of single abrasive
λ	Space between continuous cutting abrasive
h	Height of debris cross section
PTMCs	Particulate reinforced titanium matrix composites
σ	Equivalent flow stress
A	Yield stress
B	Strain hardening constant
C	Strain rate enhancement factor
n	Strain hardening factor
m	Thermal softening factor
ε	Equivalent plastic strain
$\dot{\varepsilon}$	Equivalent plastic strain rate
T_m	Material melting point
T_0	Environmental temperature
σ^*_i	Normalized strength of intact material
σ^*_f	Normalized fracture stress
D	Damage factor of the material
F_{gn}	Normal grinding force of a single abrasive
F_{gnc}	Single abrasive cutting deformation normal grinding force
dS	Area of contact area
F_p	Unit grinding force
F_{gns}	Frictional normal grinding force of a single abrasive
σ_{HEL}	Equivalent stress at the Hugoniot elastic limit
ρ	Contact cone busbar length
σ_0	Unit grinding force constant
$\overline{p}$	Average pressure
k_g	Thermal conductivity of abrasive
l_k	Motion contact arc length
θ_m	Maximum temperature in the grinding zone
l_c	Contact arc length
e_{ch}	Specific chipping energy
e_{pl}	Specific plowing energy
θ	CBN abrasive cone top half angle
P_{HEL}	Hugoniot elastic ultimate pressure
T	Maximum tensile strength
MRM	Material removal mechanism

1 Introduction

Material removal from grinding processes accounts for more than 60% of all processes in aerospace and various other fields. In 1931, high-speed machining was first proposed by Salomon, and it has since evolved into an indispensable processing technology in the realm of mechanical manufacturing, owing to its distinctive advantage in speed [1]. High-speed grinding (HSG) stands as the current frontier in advanced processing, enabling the precision manufacturing of components such as camshafts and crankshafts for automobile engines, as well as plates, shafts, blades, and other parts for aviation engines [2–8], all of which require high machining accuracy [9–13]. The handling of difficult-to-machine materials has perpetually posed a technical challenge in the field of grinding, necessitating the elevation of grinding speeds to achieve superior surface quality [14–16].

Currently, grinding speeds equal to or greater than 45 m/s are referred to as HSG, which represents an advanced processing technology aimed at achieving efficient material removal with a focus on high quality and high efficiency [17, 18]. When the ratio of v_s (grinding speed) to v_w (feed speed) remains constant, an increase in v_s alone leads to an increase in grinding force and temperature, while an increase in only the feed speed (v_w) results in a decrease in both grinding force and temperature. When the v_s/ v_w ratio is not constant, a decrease in grinding temperature and force occurs as v_s is increased to the critical speed associated with the workpiece material.

The research on HSG is mainly in the grinding mechanism, grinding equipment and other aspects of the research. The mechanism of HSG with single abrasive was investigated in Refs. [3, 19–21]. Zhao et al. [22–25] for the first time built a quasi-liquid phase impact chip formation model based on the theoretical model of the indentation experiment of brittle materials and the concept of impact chip formation, put forward the chip formation hypothesis, and found that the material removal mechanism (MRM) under HSG conditions was completely different from that of ordinary grinding. Zhang et al. [26] found that WC/Co and RB-SiC/Si had different MRMs. Yin et al. [27] found that the v_s affected the material removal effect of SiC_f/SiC. Cheng et al. [28] found that the HSG of GH4169 alloy resulted in the formation of jagged abrasive chips due to concentrated shear slip caused by adiabatic shear. Wang [29] found that the grinding process of a single abrasive was divided into three stages: sliding friction, ploughing and material removal, and chips were produced when the grinding depth (a_p) reached the critical. Li [30] indicated that material removal was achieved by dislocation movement in the crystal through HSG of silicon carbide. Zhou et al. [31] found that brittle removal of TiC_p and plastic removal of the Ti-6Al-4V matrix occurred simultaneously during the material removal process for HSG of particulate reinforced titanium matrix composites (PTMCs). Chen [32] studied the dynamic characteristics of the components of HSG machines. Yeo et al. [33] investigated spindle characteristics on HSG using oil/air mist lubrication. Sun and Yao [34] found that lowering the spindle temperature could be achieved by optimizing the operating parameters of the spindle. Liu et al. [35] found an improved thermal resistance network model for high-speed motorized spindle. Liang [36] built a vibration characteristic analysis model of balancing head rotor system.

Despite extensive research on the grinding mechanism, force, and temperature models within the context of HSG, there remains an insufficiency in comprehensive reviews summarizing prior investigations. As a response to this gap, a consolidation of previous studies has been undertaken to offer insights for future research directions, providing guidance for scholars to pursue deeper understanding and research in this area. The schematic representation of this review is depicted in Fig. 1.

2 Mechanism of HSG

HSG represents a sophisticated manufacturing technology that enhances machining precision through elevated v_s, enabling mill-turn or even superior removal rates. Within the HSG process, the deformation zone of grinding experiences significant strain (γ), elevated strain rates ($\dot{\gamma}$), and high temperatures. Consequently, modeling the dynamic properties of materials and providing an accurate depiction of their inherent models are fundamental in characterizing material deformation behaviors. These aspects serve as crucial prerequisites for the numerical simulation of the machining process. This chapter aims to deliver an exhaustive analysis of the MRM and a comprehensive overview of the force, temperature, and material constitutive models, as depicted in Fig. 2.

The advancement in surface quality has experienced a significant qualitative enhancement with the development of technology. This improvement in surface quality can be attributed to the underlying mechanisms of material removal, which are elucidated through the study of v_s, as depicted in Fig. 3 [5, 37–43]. Furthermore, the material removal process during HSG is intricate and multifaceted. The alterations occurring during this process have been meticulously analyzed through numerical simulations, as illustrated in Fig. 4 [37, 44–50].

2.1 Modelling of material removal strain rate

The strain rate effect embodies an intrinsic mechanical response property of materials [51]. This response varies markedly between quasi-static and high $\dot{\gamma}$, leading to distinct deformation and fracture mechanisms [52, 53]. Variations in $\dot{\gamma}$ during the cutting process are a primary factor influencing MRM. Under HSG conditions, an increase in $\dot{\gamma}$ alters the material response, which can be classified into static, quasi-static, and dynamic categories. These responses further bifurcate into medium $\dot{\gamma}$ and high $\dot{\gamma}$ regimes, each characterized by unique mechanical behaviors.

The single abrasive grinding formation zone has zone I deformation and zone II deformation. Chen et al. [54] also observed the above phenomenon by simulating the HSG of single abrasives of high-temperature nickel-based alloys. A single abrasive's grinding force and deformation mechanism can be described as follows.

In zone I deformation A point force diagram, as shown in Fig. 5 [55], the material fracture into chip direction (shear band direction F_s) and the angle of the combined force F_r

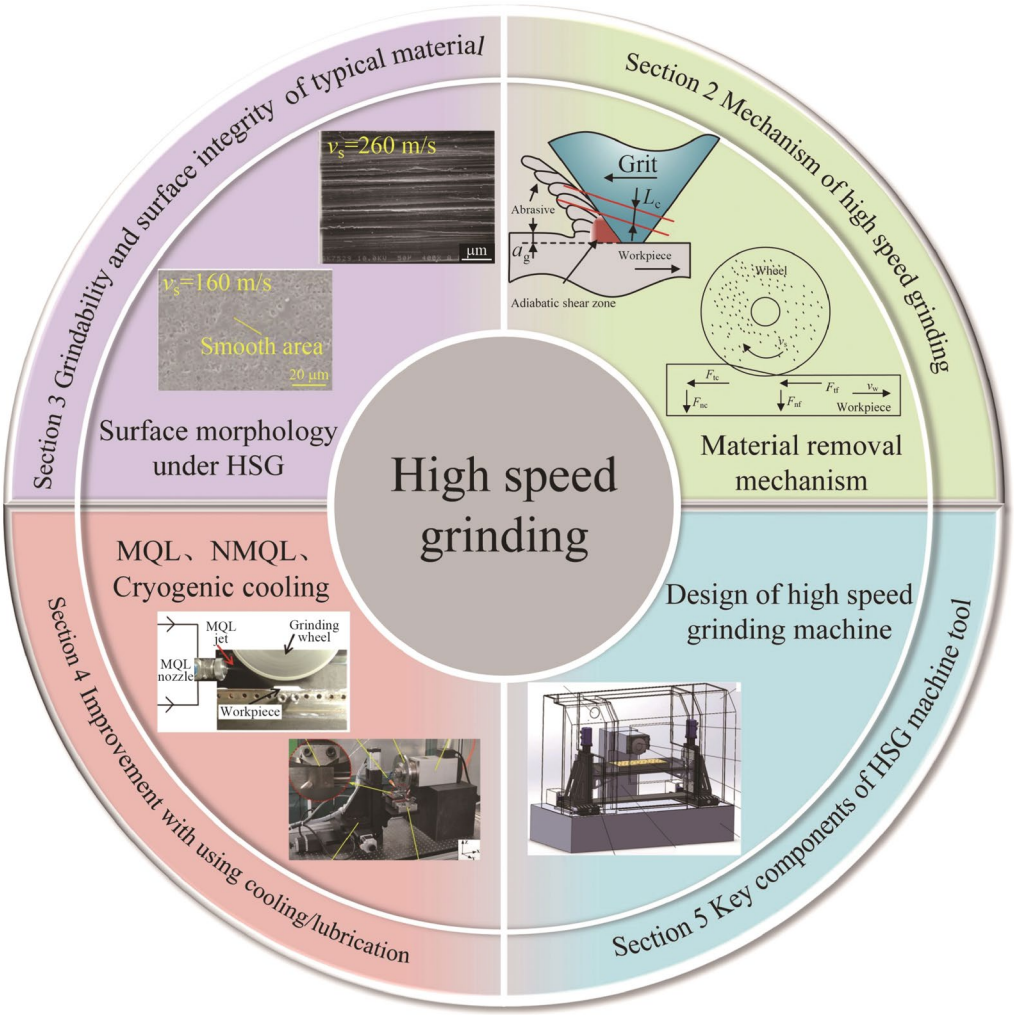

Fig. 1 Structure of this study

is π/4, shear angle φ_1 in the horizontal direction; during this period, the friction force F_f ascends along the interface between the abrasive and chip, thereby facilitating the fragmentation of the material into chips, denoted as φ_1

$$\varphi_1 = \frac{\pi}{4} + \beta_f - \gamma_0. \tag{1}$$

For abrasive cutting processing chip thickness to length ratio of about 1% [56], so the negative front angle of abrasive cutting for $\gamma_0 \approx \theta/2$, the friction angle for $\beta_f = \arctan \mu$, substitute it into Eq. (1) as

$$\varphi_1 = \frac{\pi}{4} + \arctan \mu - \frac{\theta}{2}. \tag{2}$$

In zone II deformation C point force diagram, as shown in Fig. 5b, F_f and F_n is F_r; the angle between F_s and F_r is π/4; φ_2 is under the horizontal direction. During this period, F_f is downward along the interface between abrasive and chip, thereby obstructing the fragmentation of the material into chips, denoted as φ_2

$$\varphi_2 = \beta_f + \gamma_0 - \frac{\pi}{4} = \arctan \mu + \frac{\theta}{2} - \frac{\pi}{4}. \tag{3}$$

The deformation of materials causes γ hardening and $\dot{\gamma}$ strengthening, which significantly affects the removal mechanism of materials under HSG. Jin et al. [57, 58] established the formula for strain and $\dot{\gamma}$ in the abrasive shear zone

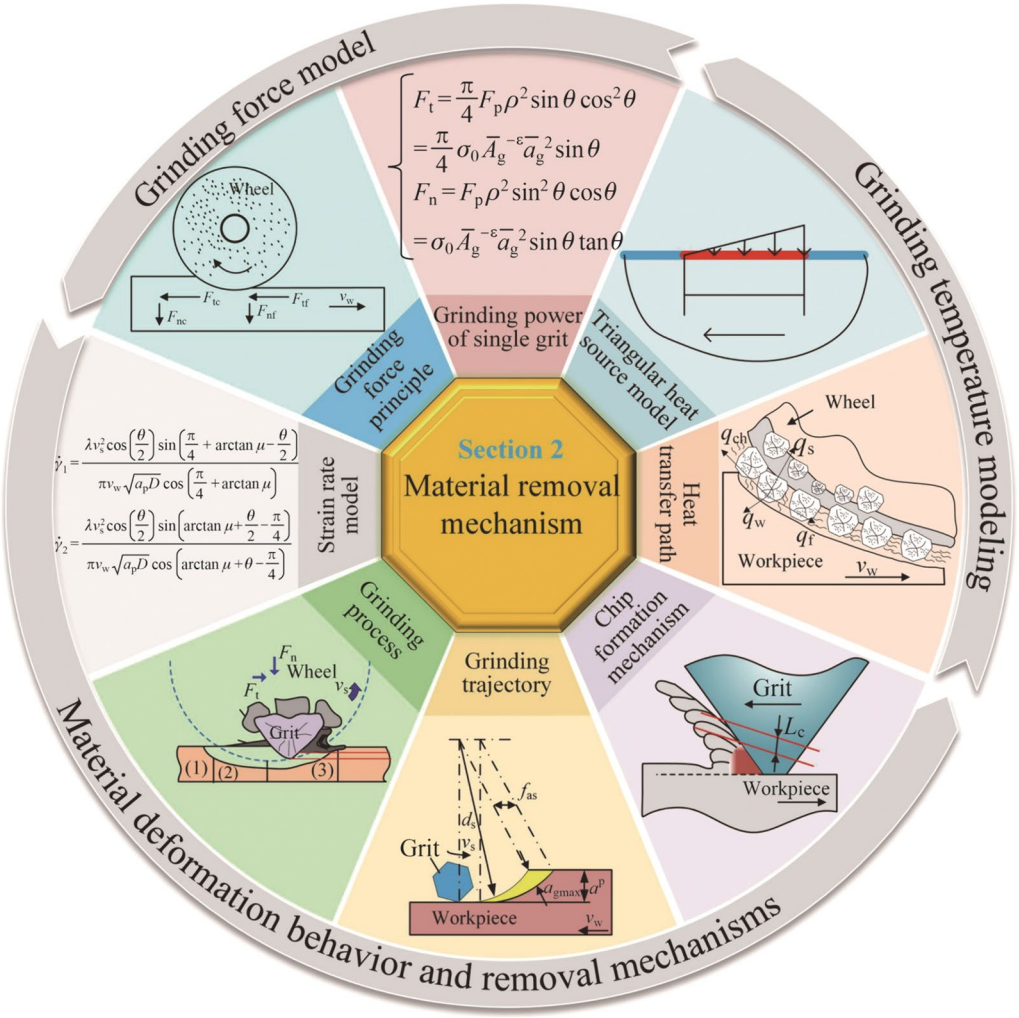

Fig. 2 Structure of material removal mechanism

$$\gamma = \frac{\cos\left(\frac{\theta}{2}\right)}{\sin\varphi\cos\left(\varphi+\frac{\theta}{2}\right)}, \tag{4}$$

$$\dot{\gamma} = \frac{2\lambda_1 v\cos\left(\frac{\theta}{2}\right)\sin\phi}{a_{\mathrm{g\,max}}\cos\left(\phi+\frac{\theta}{2}\right)}. \tag{5}$$

Substituting Eq. (16), Eq. (3) and Eq. (4) into Eq. (5), respectively, $\dot{\gamma}$ of the abrasive chips in two deformation zones is obtained as

$$\dot{\gamma}_1 = \frac{\lambda v_s^2\cos\left(\frac{\theta}{2}\right)\sin\left(\frac{\pi}{4}+\arctan\mu-\frac{\theta}{2}\right)}{\pi v_w\sqrt{a_p D}\cos\left(\frac{\pi}{4}+\arctan\mu\right)}, \tag{6}$$

$$\dot{\gamma}_2 = -\frac{\lambda v_s^2\cos\left(\frac{\theta}{2}\right)\sin\left(\arctan\mu+\frac{\theta}{2}-\frac{\pi}{4}\right)}{\pi v_w\sqrt{a_p D}\cos\left(\arctan\mu+\theta-\frac{\pi}{4}\right)}. \tag{7}$$

$\dot{\gamma}$ in both shear zones shows a linear increasing trend, as shown in Fig. 6a. When μ increases, $\dot{\gamma}$ in zone I deformation increases due to the gain effect of F_f on the material removal; $\dot{\gamma}$ in zone II deformation decreases due to the obstruction effect of F_f on the flow of debris, as shown in Fig. 6b. $\dot{\gamma}$ decreases with the increase of a_p, as shown in Fig. 6c. The velocity effect and lubrication effect produced during HSG processing affect $\dot{\gamma}$ variation trend in the two deformation zones, as shown in Fig. 6d.

The removal of metallic material during the process is a result of plastic deformation occurring when the material undergoes an increase in γ. Previous research has extensively utilized dynamic material tensile tests to illustrate the occurrences of γ hardening and $\dot{\gamma}$ strengthening [59]. Material

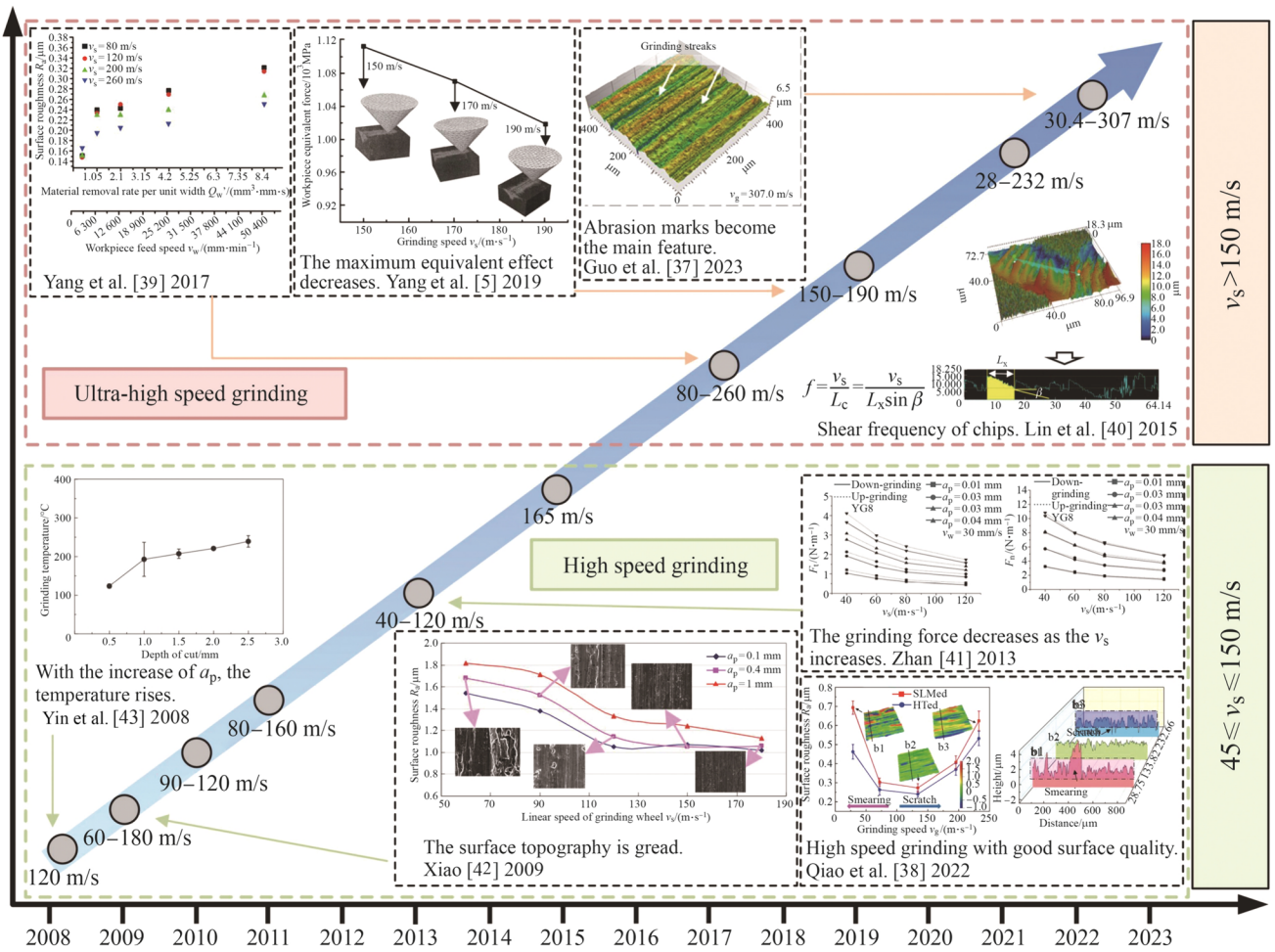

Fig. 3 Grinding speed milestone diagram [5, 37–43]

removal can be divided into three parts due to the softening of the material after grinding heat and the reduction of deformation resistance during $\dot{\gamma}$ strengthening, as shown in Fig. 7 [54].

Yang [39] found that the relationship between $\dot{\gamma}$ strengthening and thermal softening changed with the increase of v_s in the HSG of GH4169 using single abrasive. The materials under high $\dot{\gamma}$ loading would produce embrittlement effect [53, 60], which was conducive to reducing subsurface depth damage of the workpiece materials and formation of the "damage peeling" effect. Dislocation diffusion and slip are the main causes of plastic deformation and fracture during grinding of plastic metal materials and hard and brittle materials [61]. Liu [62] found that there were dual removal mechanisms of ductile flow and brittle fracture in the grinding process of nanoceramic materials. Wang et al. [63] found that the chip morphology gradually became discontinuous with the increase of $\dot{\gamma}$. Ma et al. [64] found that with the increase of v_s, brittle fracture and ductile fracture were obvious when brittle fracture occurred on the free surface of chips. Zhang et al. [65] found that the average fragment size of brittle materials decreased with the increase of $\dot{\gamma}$ at high $\dot{\gamma}$.

2.2 Modelling of material removal constitutive

During the grinding of metallic materials, the workpiece material is subjected to significant structural transformations when the heat generated from deformation and friction exceeds a critical threshold [66, 67]. These transformations are effectively captured by the intrinsic model of the material, which delineates the variations in flow stresses experienced during material deformation. Table 1

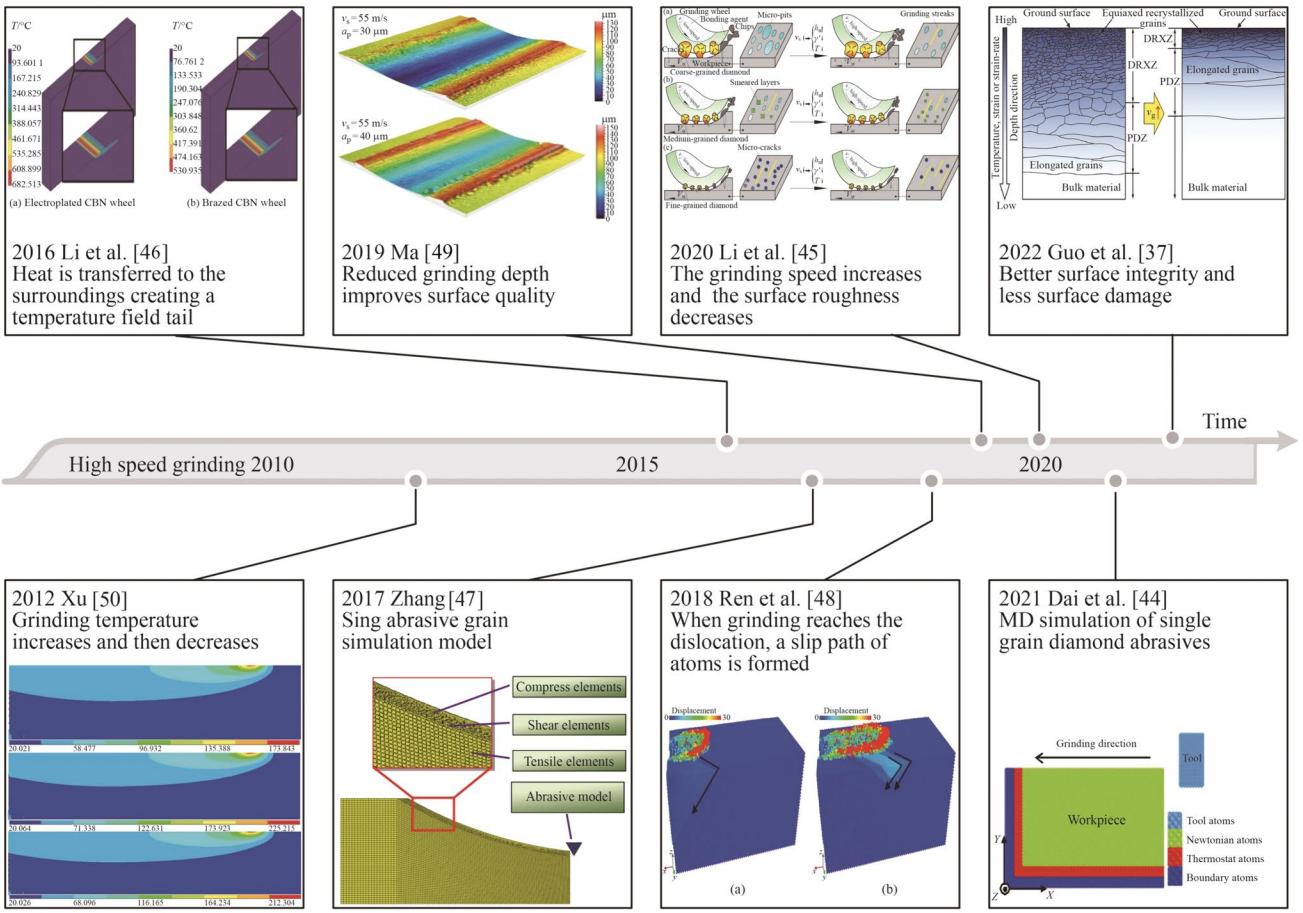

Fig. 4 Numerical modelling research milestones [37, 44–50]

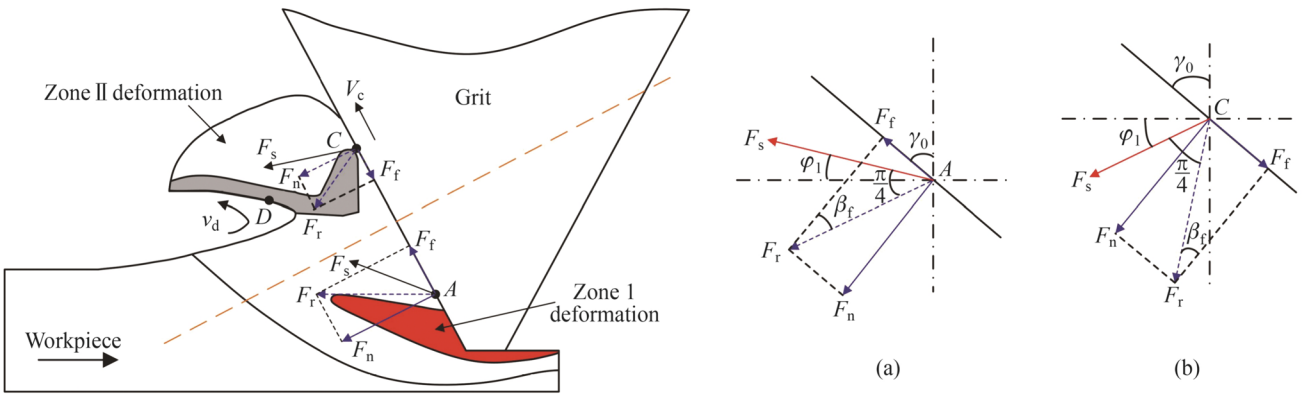

Fig. 5 Mechanism of material deformation in the chip-forming region **a** force analysis of the first deformation zone of workpiece material, **b** force analysis of the second deformation zone of workpiece material [55]

presents the principal parameters of the Johnson-Cook (J-C) model, outlining their values for several types of workpiece materials [37, 66, 68–72].

The J-C model considers the changes of γ, $\dot{\gamma}$, temperature and other factors, and can be expressed as [73]

$$\sigma = (A + B\varepsilon^{n})\left(1 + C\ln\frac{\dot{\varepsilon}}{\dot{\varepsilon}_0}\right)\left(1 - \left(\frac{T - T_0}{T_{\text{melt}} - T_0}\right)^{m}\right). \quad (8)$$

Johnson and Holmquist [74, 75] proposed a J-H constitutive model for brittle materials

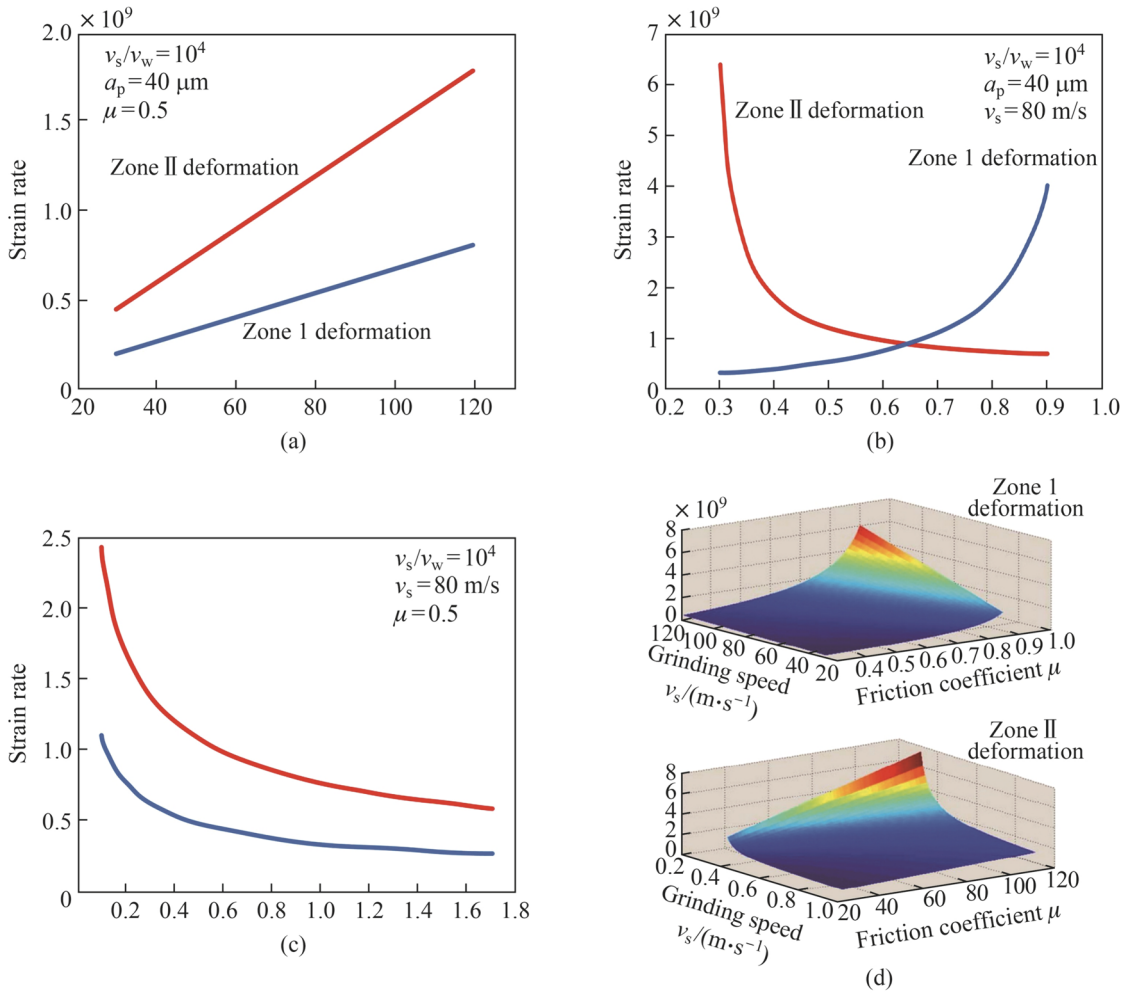

Fig. 6 Strain rate under different grinding parameters and frictional coefficients **a** effect of grinding speed on strain rate, **b** influence of different friction coefficients on strain rate, **c** effect of different grinding depths on strain rate, **d** strain rate under different grinding parameters and friction coefficients [54]

$$\sigma^* = \sigma_i^* - D\left(\sigma_i^* - \sigma_f^*\right). \tag{9}$$

The dimensionless expression is

$$\sigma^* = \sigma/\sigma_{HEL}. \tag{10}$$

The strength of the intact material σ_i^* is

$$\sigma_i^* = A(P^* + T^*)^N(1 + C\ln\dot{\varepsilon}^*). \tag{11}$$

The dimensionless pressure P^* and the maximum tensile strength T^* are

$$P^* = \frac{P}{P_{HEL}}, \tag{12}$$

$$T^* = \frac{T}{P_{HEL}}. \tag{13}$$

The dimensionless strength σ_f^* of the partially damaged material is

$$\begin{cases} \sigma_f^* = B(P^*)^M(1 + C\ln\dot{\varepsilon}^*), \\ \sigma_f^* \le \sigma_{fmax}^*. \end{cases} \tag{14}$$

J-C constitutive model considers the effects of γ, $\dot{\gamma}$ and temperature on material load response in machining simulation. In order to adapt to the response of different parameters to dynamic load under different materials and loading conditions, a modified model is proposed based on the J-C constitutive model, as shown in Table 2 [77–84].

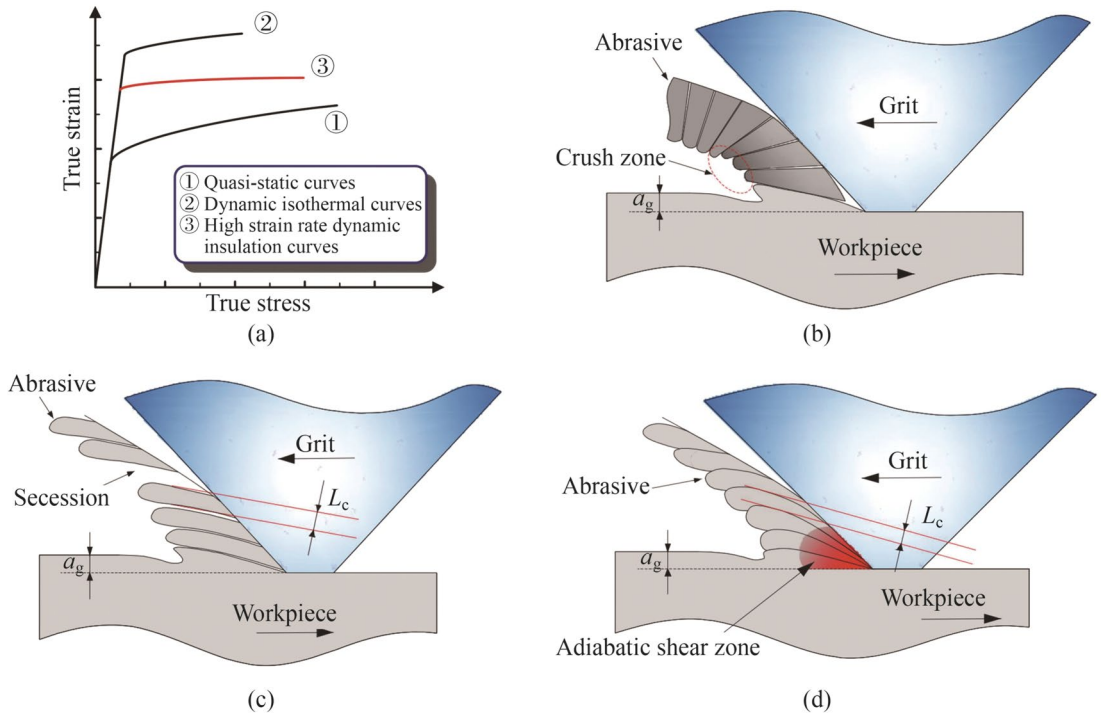

Fig. 7 Effect of strain hardening, strain rate strengthening and thermal softening in material removal after grinding **a** stress-strain curves under "speed effect", **b** debris forming mechanism under quasi-static condition, **c** debris forming mechanism under high strain-isothermal condition, **d** debris forming mechanism under high strain condition [54]

Table 1 Workpiece material J-C model main parameters

	A/MPa	*B*/MPa	*n*	*C*	T_0/°C	T_{melt}/°C	*m*
GH4169 [68]	1 241	622	0.652 2	0.013 4	25	1 300	1.300
AISI1045 [69]	835	780	0.3070	0.413 0	25	1 492	0.804
Ti-6Al-4V [70, 71]	875	793	0.3860	0.0100	20	1 560	0.710
Ai6061T6 [37]	201.55	2 501.87	0.2060	0.2060	293	855	1.310
Inconel 718 [66]	450	1 700	1.300 0	0.0170	20	1 320	0.650
20CrMo [72]	626	347	0.480 0	0.028 4	25	1 800	0.610

2.3 Modelling of debris geometry

The foundational concept of the HSG mechanism can be traced to the seminal high-speed cutting theory postulated by the renowned German physicist Solomon in 1931 [1]. This theory posits a critical velocity threshold, beyond which the cutting temperature notably decreases. This phenomenon is effectively illustrated in Fig. 8 [76].

The deformation behavior of materials under HSG and their corresponding removal mechanisms markedly differ from those observed in traditional grinding. This distinction arises primarily from the interactions between the abrasives and the workpiece material. The complexity of the MRM in HSG is heightened due to variables such as the quantity and shape of abrasives, the randomness of their positioning, and the variability in cutting strength. In the context of grinding, each abrasive represents a microcosmic view of the cutting process, which manifests in three distinct stages: the elastic deformation phase, the elastic-plastic deformation stage, and the chip formation stage, as depicted in Fig. 9a.

For a single abrasive HSG with the same chip shape each time, the maximum chip thickness is called the maximum undeformed chip thickness $a_{g\,max}$ [54]. The a_g function is discussed into A-B and B-C, because the cutting thickness changes differently before and after point B, as shown in Fig. 9b [54].

In phase A-B the α interval is $[0, \alpha_1]$ can be obtained

Table 2 Several typical modified J-C constitutive models [76]

Refs.	Workpiece	Modified J-C models	The highest $\dot{\gamma}$	Remarks
[77, 78]	OFHC, 7050-T7451	$\sigma = (A + B\varepsilon^n)\left(1 + C\ln\left(1 + \frac{\dot{\varepsilon}}{\dot{\varepsilon}_0}\right)\right)\left(1 - \left(\frac{T - T_r}{T_m - T_r}\right)^m\right)\left(\frac{(\sigma_f)_{def}u(T) + (\sigma_f)_{rec} - (\sigma_f)_{def}}{(\sigma_f)_{def}u(T)}\right)$	$10^4\ s^{-1}$	Considering softening effect induced by dynamic recrystallization
[79]	Ti6Al4V	$\sigma = \left(A + B\varepsilon^n\left(\frac{1}{\exp(\varepsilon^a)}\right)\right)\left(1 + C\ln\frac{\dot{\varepsilon}}{\dot{\varepsilon}_0}\right)\left(1 - \left(\frac{T - T_r}{T_m - T_r}\right)^m\right)\left(D + (1 - D)\tanh\left(\frac{1}{(\varepsilon + S)^c}\right)\right)$	$10^3\ s^{-1}$	Considering γ softening effect
[80]	Pure titanium	$\tau = B\gamma^n\left(1 + C\ln\frac{\dot{\varepsilon}}{\dot{\varepsilon}_0}\right)\left(\alpha e^{\beta\left(\frac{T_m - T}{T_m - T_r}\right)}\right)$	$10^2\ s^{-1}$	Change γ hardening and heat softening
[81]	1045 steel	$\sigma = \left(A\left(HRC + B\varepsilon^{n(HRC)}\right)\right)\left(1 + C\ln\frac{\dot{\varepsilon}}{\dot{\varepsilon}_0}\right)\exp\left(-\left(\frac{T^* - m_1}{m_2}\right)^2\right)$	$10^4\ s^{-1}$	The influence of hardness on γ hardening is considered
[82]	Inconel 718	$C = C_1 - \left(C_2 + C_3\sin\left(\frac{T - 500}{150}\pi\right)\right)$	$10^4\ s^{-1}$	Considering $\dot{\gamma}$ softening effect
[83]	Haynes 282	$\sigma = (A + B\varepsilon^n)(1 + C_1\ln\dot{\varepsilon})\exp((\lambda_1 + \lambda_2\ln\dot{\varepsilon})(T - T_r))$	$10^3\ s^{-1}$	Consider the coupling of $\gamma/\dot{\gamma}$ with temperature
[84]	7050-T7451	$\sigma = (A + B\varepsilon^n)\left(1 - \frac{\tanh(\varepsilon)}{\exp(\varepsilon^p)}m_1\ln\left(\frac{T}{T_r}\right)\right)\left(1 + C\left(1 - \left(\frac{T}{T_m}\right)^{m^2}\right)\ln\frac{\dot{\varepsilon}}{\dot{\varepsilon}_0}\right)\left(1 - \left(\frac{T - T_r}{T_m - T_r}\right)^{m^3}\right)$	$10^4\ s^{-1}$	Consider the coupling of $\gamma/\dot{\gamma}$ with temperature

$$\alpha_1 = \arccos\frac{D-2a_p}{D-2a_{g\max}}. \tag{15}$$

When the abrasive cuts to point B, the abrasive spacing λ is equal to the circumference of the grinding wheel disc πD, so $a_{g\max}$ can be expressed as

$$a_{g\max} = 2\pi\frac{v_w}{v_s}\sqrt{a_p D}. \tag{16}$$

When the abrasive cuts to α ($0 \le \alpha \le \alpha_1$) and α_1 ($\alpha_1 \le \alpha \le \alpha_2$), the chip thickness formula of abrasives can be calculated as

$$a_g(\alpha) = \begin{cases} \pi D\frac{v_w}{v_s}\sqrt{2(1-\cos\alpha)}, 0 \le \alpha < \alpha_1, \\ \dfrac{a_p - \frac{D}{2}(1-\cos\alpha)}{\cos\alpha}, \alpha_1 \le \alpha \le \alpha_2. \end{cases} \tag{17}$$

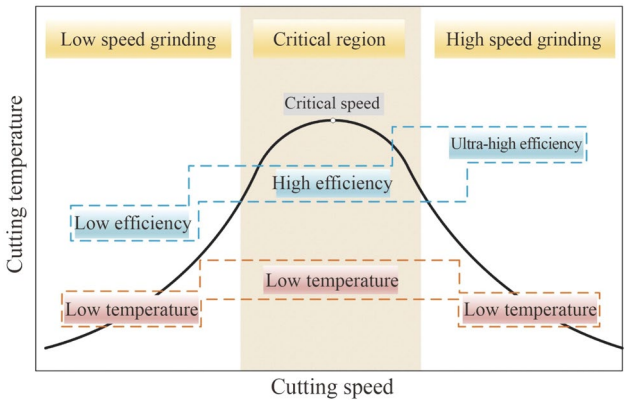

Fig. 8 Solomon "speed-temperature" curve diagram [76]

According to the geometric relationship between the abrasive cutting path and the abrasive chip section height, the calculation formula of the abrasive chip cross-sectional area S can be obtained, as shown in Fig. 9c

$$S(\alpha) = \begin{cases} a_g(\alpha)\tan\frac{\theta}{2}\left(2h(\alpha) - a_g(\alpha)\right), 0 \le \alpha < \alpha_1, \\ h(\alpha)^2\tan\frac{\theta}{2}, \alpha_1 \le \alpha \le \alpha_2. \end{cases} \tag{18}$$

The study of chip morphology is the most direct way to explore the mechanism of cutting and grinding of metal materials, but it is rarely studied. During the formation of chips and scratches in HSG, the workpiece undergoes plastic deformation and fracture removal. Yang [39] found that with the increase of v_s, chips became longer and thinner; the equivalent stress, plastic strain, strain and grinding temperature increased; and the grinding force, residual stress and strain decreased, as shown in Fig. 10a. Liu et al. [85] found that the removal process of PTMCs material was divided into four stages: plastic removal of matrix material, crack initiation of reinforced abrasives, crack propagation of reinforced abrasives and brittle destruction of reinforced abrasives, as shown in Fig. 10b. Wu et al. [86] performed HSG of enamel surfaces, in which the fracture modes of the occlusal surface were steady-state shear material removal, flexural shear complex fracture material removal and ironing, as shown in Fig. 10c, tongue in cheek/surface for the unsteady shear complex material removal, bending shear fracture material removal and ironing, as shown in Fig. 10d.

Setti et al. [87] found that chip morphology changed greatly under different grinding conditions. The shapes of abrasive chips were mainly divided into bands, nodules and spheres [88, 89]. Wu et al. [86] found that the steady-state grinding process of the occlusal surface was less at high

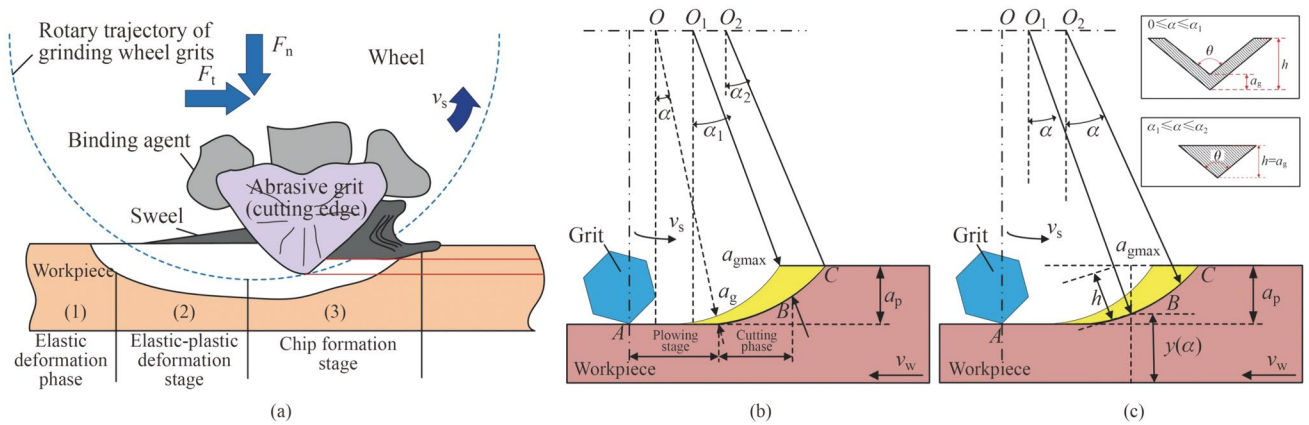

Fig. 9 Single abrasive slip model in grinding process **a** grinding process diagram [47], **b** thickness of abrasive chips, **c** cross-sectional shape and area of abrasive [54]

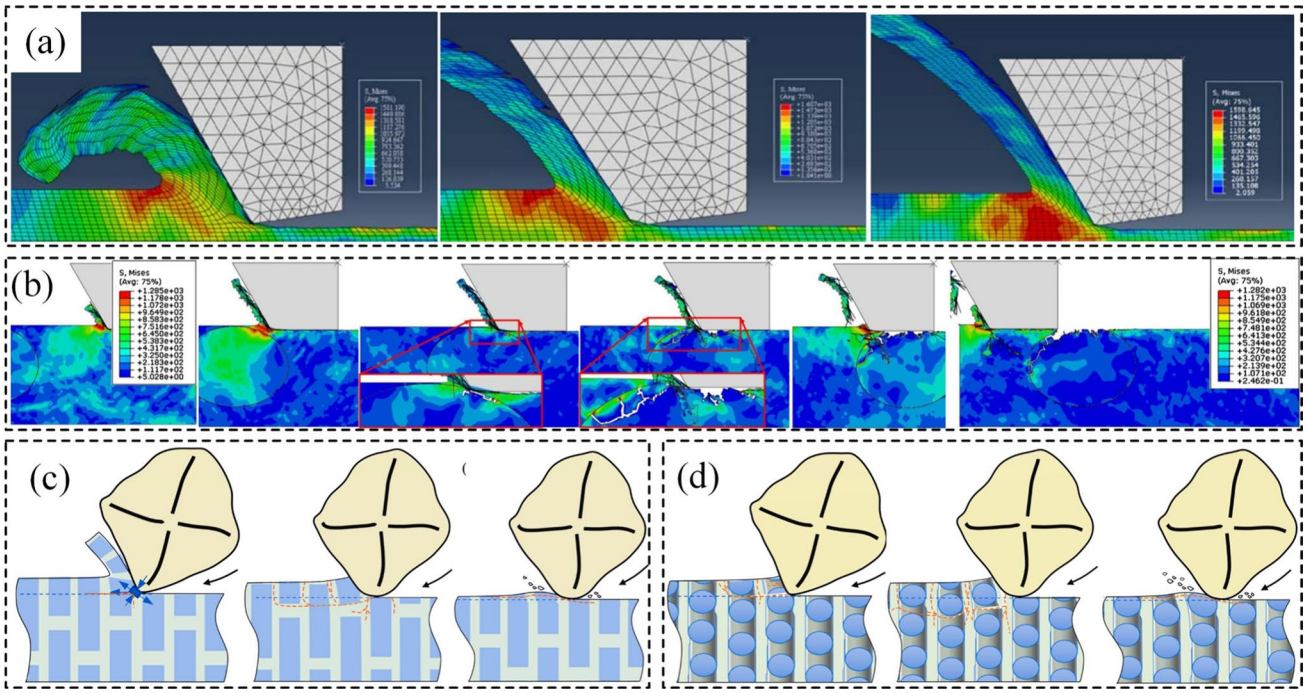

Fig. 10 HSG of different materials to remove the changes produced by grinding chips **a** plastic strain and $\dot{\gamma}$ of GH4169 at v_s=240 m/s [39], **b** material removal process in grinding of PTMCs [85], **c** mechanism of occlusal surface material removal [86], **d** mechanism for removal of buccal/lingual material [86]

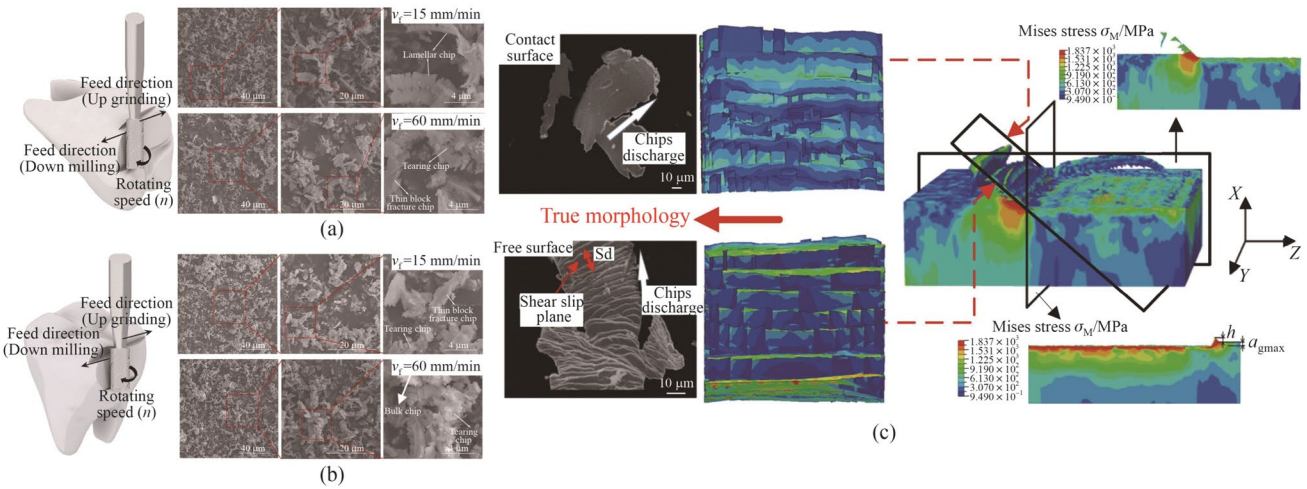

Fig. 11 Chip morphology of different workpiece materials after HSG **a** enamel surface grinding of occlusal surfaces and chip shape of occlusal surface grinding [86], **b** buccal/lingual enamel surface grinding and chip shape of buccal/lingual surface grinding [86], **c** morphology of abrasive chips and workpiece surface for grinding GH4169 with a single abrasive [90]

feed rate, and the chips under the cheek/tongue surface were larger and more irregular, which was more difficult to be broken by magic shear, as shown in Figs. 11a, b. Xia et al. [90] found that the wear chips had adiabatic shear sliding properties when grinding GH4169 alloy with a single abrasive, as shown in Fig. 11c. Cheng et al. [28] found that with the increase of v_s on the free surface of GH4169 alloy scraps, the thermal softening effect was enhanced and the grinding resistance decreased.

2.4 Modelling and change rule of grinding force

The grinding force mainly consists of the cutting force and friction force in the removal of abrasive grinding materials, surface friction and material adhesion [69, 91]. In different stages of friction cutting, the grinding force mainly comes from the grinding abrasive overcoming the deformation of parts and the friction of parts materials. The grinding force model of a single abrasive is [92]

$$\begin{cases} F_{gt} = F_{gtc} + F_{gts}, \\ F_{gn} = F_{gnc} + F_{gns}. \end{cases} \tag{19}$$

On the *X*-*X* plane, the grinding force model is simplified by considering the cutting force, and the cutting force dF_{gc} perpendicular to the contact surface between a single abrasive and the sample is decomposed into normal and tangential grinding forces, as shown in Fig. 12a.

$$dF_{gc} = \frac{1}{2} F_p \rho^2 \sin\theta \cos\theta \cos\alpha d\alpha. \tag{20}$$

Therefore, the grinding force of the abrasive is

$$\begin{cases} F_{gtc} = \int_{-\frac{\pi}{2}}^{\frac{\pi}{2}} dF_{gtc} = \frac{\pi}{4} F_p \rho^2 \sin\theta \cos^2\theta = \frac{\pi}{4} F_p \overline{a_g}^2 \sin\theta, \\ F_{gnc} = \int_{-\frac{\pi}{2}}^{\frac{\pi}{2}} dF_{gnc} = F_p \rho^2 \sin^2\theta \cos\theta = F_p \overline{a_g}^2 \sin\theta \tan\theta. \end{cases} \tag{21}$$

Unit grinding force F_p represents the main cutting force acting on abrasive per unit area

$$F_P = \sigma_0 \overline{A_g}^{-\varepsilon} \; 0.5 < \varepsilon < 0.95. \tag{22}$$

Then the single abrasive cutting force equation is

$$\begin{cases} F_{gtc} = \int_{-\frac{\pi}{2}}^{\frac{\pi}{2}} dF_{gtc} = \frac{\pi}{4} F_p \rho^2 \sin\theta \cos^2\theta = \frac{\pi}{4} \sigma_0 \overline{A_g}^{-\varepsilon} \overline{a_g}^2 \sin\theta, \\ F_{gnc} = \int_{-\frac{\pi}{2}}^{\frac{\pi}{2}} dF_{gnc} = F_p \rho^2 \sin^2\theta \cos\theta = \sigma_0 \overline{A_g}^{-\varepsilon} \overline{a_g}^2 \sin\theta \tan\theta. \end{cases} \tag{23}$$

When a single abrasive acts on the workpiece, the part is plastic-deformed and slides along the abrasive surface; and friction is generated. For the spherical cone wear abrasive model, the workpiece material has dynamic friction in the conical surface of the wear abrasive, and the sphere top surface region, then the conflict of a single wear abrasive is [73]

$$\begin{cases} F_{gts} = \mu \overline{p} \overline{A}_g, \\ F_{gns} = \overline{p} \overline{A}_g. \end{cases} \tag{24}$$

In the grinding process, the abrasive cutting workpiece will produce elastic deformation force, plastic deformation force, chip deformation force, friction between the sand and the workpiece, and the fluid resistance of the coolant to the grinding wheel. For single-abrasive grinding, there is no friction between the workpiece and the use of the binder because of the control of the a_p; the total grinding force is

$$\begin{cases} F_t = F_{tc} + F_{ts} = \frac{\pi}{4} \sigma_0 \overline{A_g}^{-\varepsilon} \overline{a_g}^2 \sin\theta + \mu \overline{p} \overline{A}_g, \\ F_n = F_{nc} + F_{ns} = F_{nc} = \sigma_0 \overline{A_g}^{-\varepsilon} \overline{a_g}^2 \sin\theta \tan\theta + \overline{p} \overline{A}_g. \end{cases} \tag{25}$$

There are four contacts between the abrasive and the workpiece, as shown in Fig. 12b: shear deformation, friction between the chip and the abrasive, cutting edge related to abrasive sharpness, and friction between the abrasive and the workpiece [93]. The normal force F_t (F_{tc}+F_{tf}) and tangential force F_n (F_{nc}+F_{nf}) are the combined normal and tangential components of the chip-forming and friction forces, as shown in Fig. 12c.

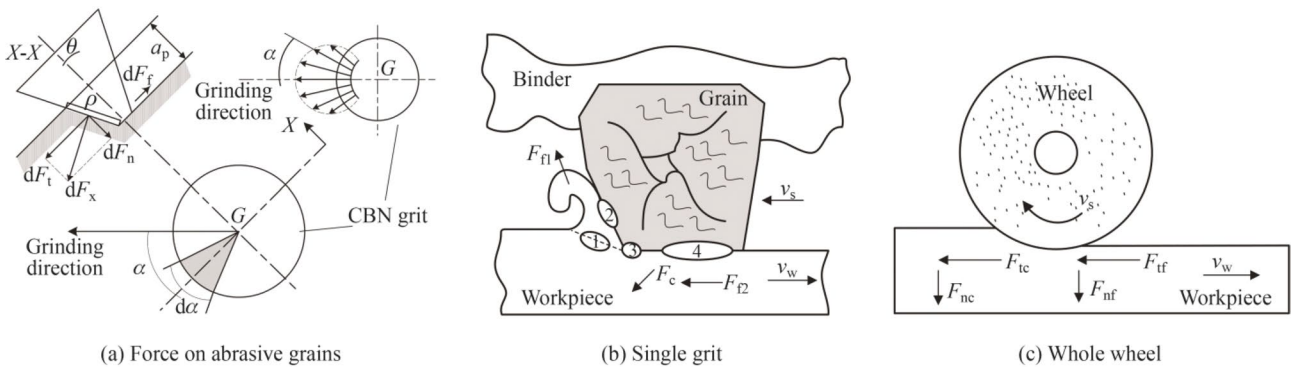

(a) Force on abrasive grains (b) Single grit (c) Whole wheel

Fig. 12 Grinding force model in HSG **a** force on abrasive [5], **b**, **c** schematic diagram of grinding force [93]

Dai et al. [66] found that in the HSG of Inconel 718 alloy, the chip formation stage began, accompanied by the shear slip of the adiabatic shear band, and finally the chip formation was completed, among which the chip was the cause of the grinding force jitter [94]. Liu et al. [95] found that in HSG 18CrNiMo7-6 with a certain material removal rate, the grinding force decreased with the increase of v_s, and the cutting thickness of a single abrasive became thinner, as shown in Fig. 13a. Patidar et al. [96] found that the grinding force of yttrium-stabilized zirconia (YZS) in HSG decreased with the increase of v_s, and the grinding force ratio was close to that of metal alloy, as shown in Fig. 13b. Liu et al. [85] found that the rise and fall of the grinding force during the removal of reinforced abrasivs in HSG PTMCs was related to the interaction between abrasive and reinforced abrasives, as shown in Fig. 13c. Cheng et al. [28] found that as the grinding force of GH4169 decreased during HSG with a single grit, as shown in Fig. 13d. Zhang [47] found that after AISI 1045 steel of HSG, the plastic deformation and adiabatic shear effect of the material increased and the grinding force decreased with the increase of v_s; the number of abrasives involved in grinding and grinding force increased with the increase of a_p; the force of the abrasive along the cutting direction became smaller; and the cutting efficiency increased with the increase of the angle of the front end of the abrasive, as shown in Fig. 13e.

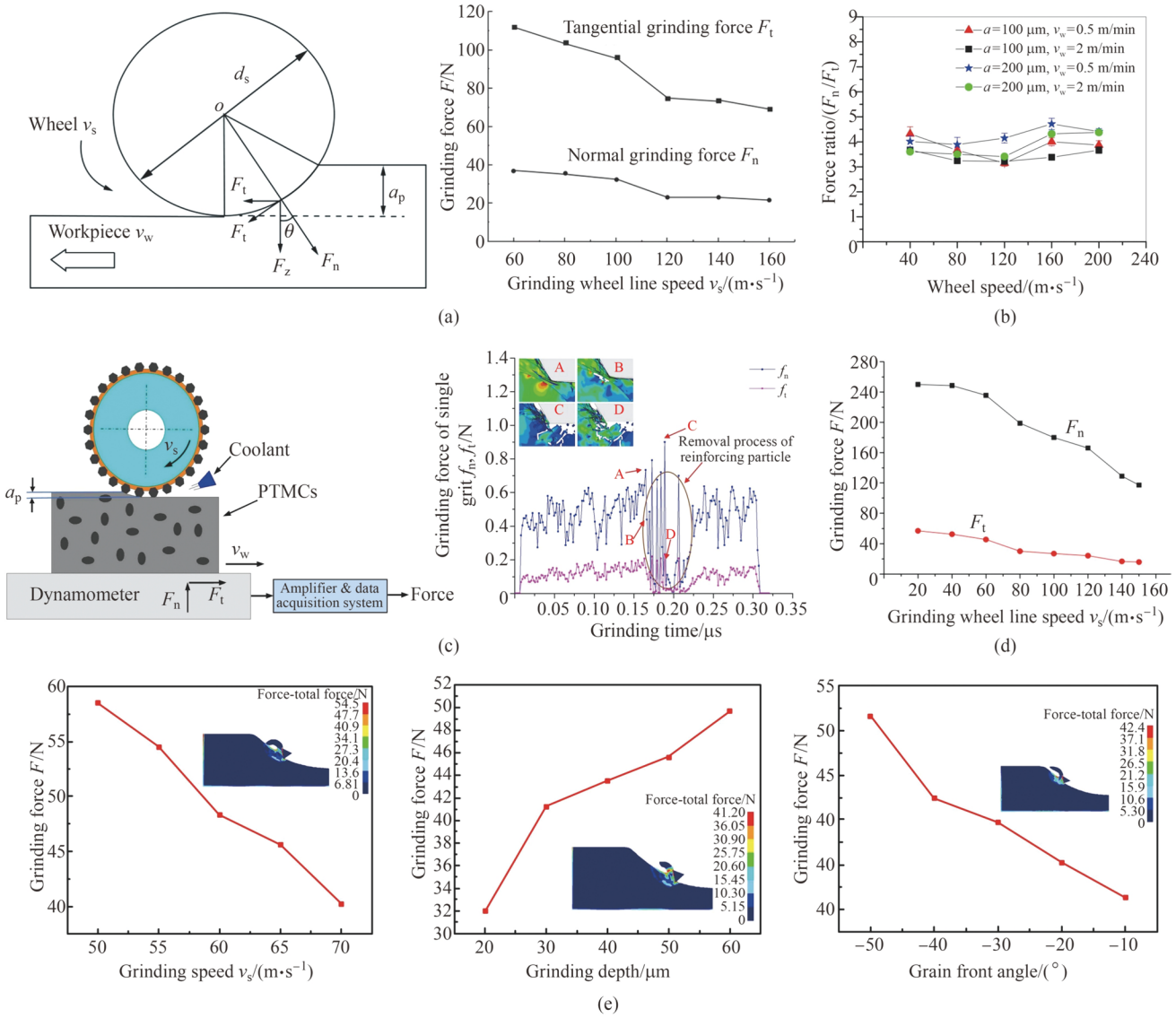

Fig. 13 Change of grinding force of different workpiece materials in HSG **a** HSG of 18CrNiMo7-6 material to obtain the relationship between grinding force and the v_s [95], **b** variation of force ratio with the v_s [96], **c** grinding force profile of PTMC material obtained by finite element modeling [85], **d** HSG of GH4169 alloy to obtain the variation of single abrasive grinding force versus grinding speed [28], **e** effect of the v_s, a_p, and abrasive front angle on grinding force [47]

2.5 Modelling and change rule of grinding temperature

The material removal rate of HSG is higher than that of other processing. About 60%–95% of the heat is transferred to the workpiece, and less than 10% of the heat is taken away by the chips, which easily leads to the temperature of the grinding wheel and the workpiece [97, 98]. Because the v_s is very high, the heat can not be transferred to the depth of the workpiece and the thin layer temperature continues to rise to a certain point. The machined surface will produce various thermal damage and thermal deformation affecting the quality of the machined surface. Controlling and reducing grinding temperature is an important step to improve grinding quality.

The heat generated by the contact between the workpiece and the grinding wheel is mainly transferred to the workpiece, the grinding wheel, the chip and the coolant, as shown in Fig. 14a

$$q_t = q_w + q_{ch} + q_s + q_f. \tag{26}$$

The total heat flux q_t is

$$q_t = \frac{F_t \times v_s}{b \times l_c}. \tag{27}$$

Rowe [99] proposed the heat distribution theory and obtained the grinding temperature as follows

$$T_{max} = \frac{q_w}{h_w} = \frac{(q_t - q_{ch} - q_f)R_{ws}}{h_w} \tag{28}$$

The analysis of grinding temperature takes into account the shape and distribution of heat source. Makino et al. [101] discovered that the length of the grinding heat source was 2–3 times of the geometric length. Tönshoff et al. [102] discovered that contact length could be predicted by considering both geometric contact length and deformable contact length caused by stress-induced deformation. Guo and Malkin [103] discovered that more than 60% of the grinding heat was transferred to the workpiece through the geometric contact length.

So far, three heat source distribution shapes have been proposed based on the different contact states between the grinding wheel and the workpiece: the heat source region is approximately flat and regarded as moving on a semi-infinite surface, as shown in Fig. 14b; the heat source in the grinding zone is applied to the angle between the grinding surface and the unground surface to cause the temperature rise of the workpiece, as shown in Fig. 14c; the circular heat source model, as shown in Fig. 14d [100]. The temperature predicted by the uniformly distributed heat source is not in good agreement with the measured temperature, as shown in Fig. 14e. So a triangular heat source distribution with good agreement with the measured temperature distribution is proposed, as shown in Fig. 14f.

Based on the circular heat source model, a coordinate system, is established, as shown in Fig. 14g. According to the distribution of the grinding force, the conical surface of the grinding contact surface can be regarded as a heat source with a moving speed of v_f. The motion contact arc length is l_k; the heat source contact surface is differentiated into the heat source curve l_i. Then the temperature rise in time t is

$$\theta = \frac{1}{\pi k}\int_0^{l_k} q e^{-\frac{(x-x_i)v_x+(y-y_i)v_y}{2\alpha}} K_t\left(\frac{vr_i}{2\alpha}\right) dl_i. \tag{29}$$

The corresponding dimensionless temperature can be obtained as

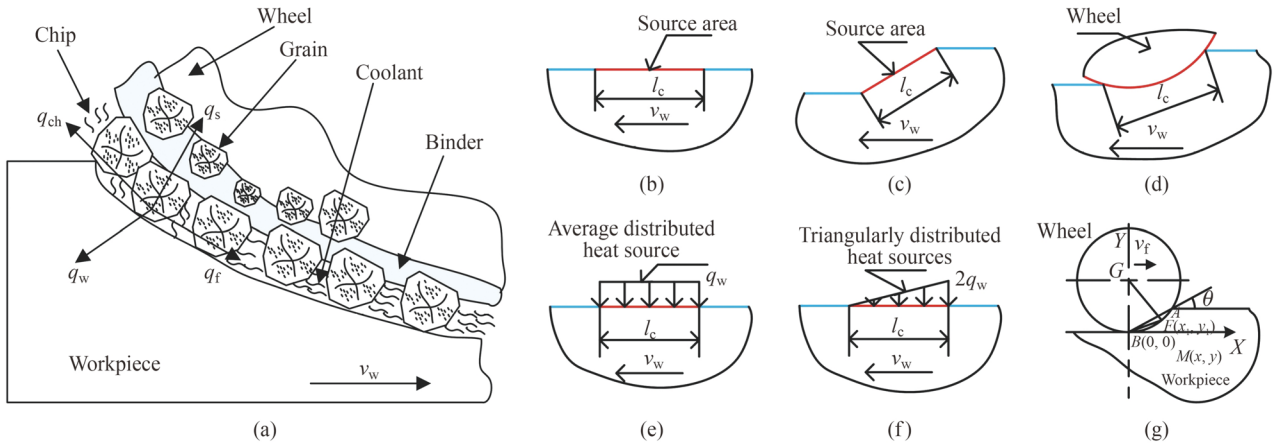

Fig. 14 Distribution of grinding heat and grinding heat source model in HSG **a** heat transfer path [93], **b–f** several grinding heat source distribution models, **g** coordinate system for circular heat source modeling [69, 100]

$$\overline{\theta} = \frac{\pi K v_s}{2\alpha \overline{q}} T. \tag{30}$$

The maximum grinding temperature θ_m is when the heat source of the 2D heat transfer model is uniformly distributed

$$\theta_m = \frac{2.256\alpha q L^{\frac{1}{2}}}{kV}. \tag{31}$$

The heat source half-length l is half the contact arc length l_c

$$l = \frac{l_c}{2} = \frac{\left(a_p d_e\right)^{\frac{1}{2}}}{2}. \tag{32}$$

Combining Eq. (31) and Eq. (32) gives the max temperature rise in the grinding zone as

$$\theta_m = \frac{1.128 q \alpha^{\frac{1}{2}} a_p^{\frac{1}{4}} d_s^{\frac{1}{4}}}{k v_w^{\frac{1}{2}}}. \tag{33}$$

3 Grindability and surface integrity of typical material

Different workpiece materials necessitate distinct grinding parameters, each exerting a unique impact on grinding efficiency. Among these parameters, surface roughness stands as a critical metric for assessing the machining outcome. This chapter provides a comprehensive analysis of how various workpiece materials influence surface roughness, as illustrated in Fig. 15. Additionally, it delves into the effects of these materials on the HSG testing process, detailed in Table 3 [5, 45, 47, 72, 107, 109, 118–132].

3.1 Alloy and steel

The incorporation of elements such as iron, carbon, chromium, and nickel into alloy steel imbues it with superior properties, including high strength, cost-effectiveness, and enhanced corrosion resistance. In their research on JIS SUJ2 bearing steel, Ichida et al. [104] observed that an increase in v_s led to a reduction in grinding-induced grooves and surface roughness, alongside an elevation in the grinding force ratio, as depicted in Fig. 16a. Concurrently, Zhang [47] reported

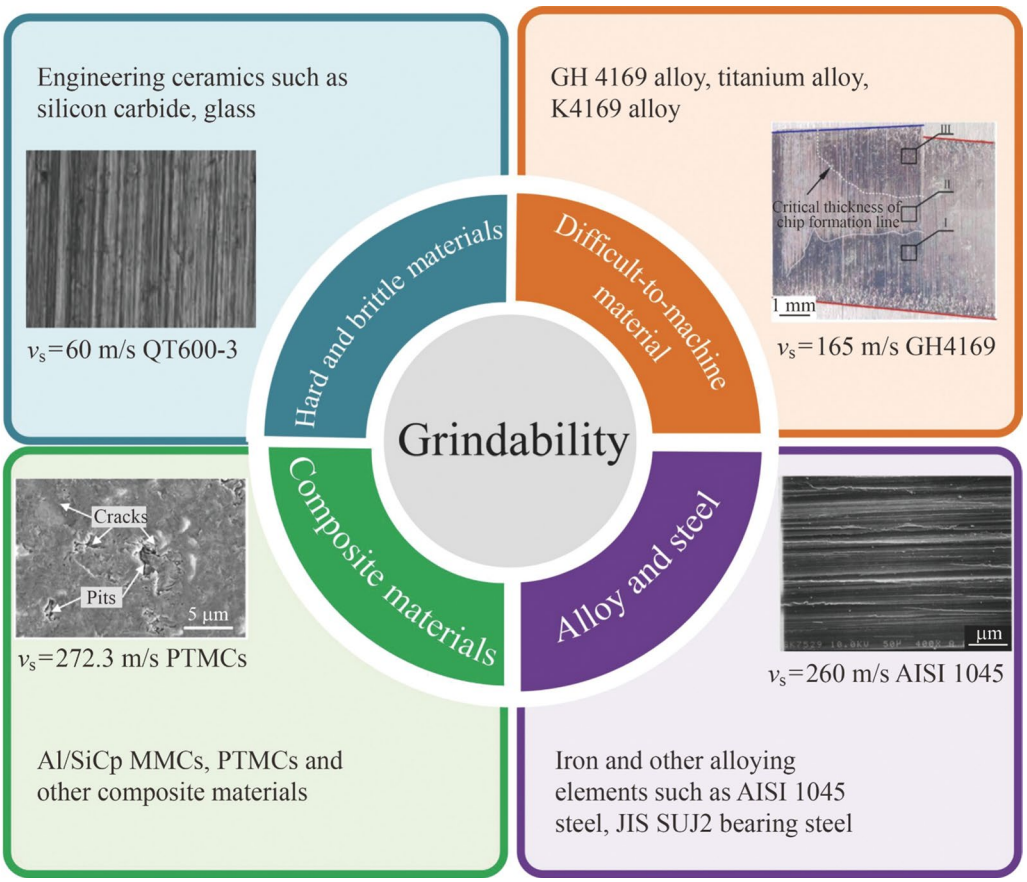

Fig. 15 Surface topography and structure of different workpiece materials

Table 3 Influence of different workpiece materials on grinding experiment

References	Workpiece	Grinding speed ($m \cdot s^{-1}$)	Research content	Result
Steels				
[47]	AISI 1045 alloy	55–70	Grinding force	The grinding force decreases with the increase of v_s
[5]	Q45	150–190	Grinding force	As v_s increases, the grinding force decreases
[118]	Stainless steel	40–200	Surface quality	Under HSG conditions, good surface quality can be obtained
[119]	18CrNiMo7-6	60–120	Residual stress	The surface residual stress increases with the increase of v_s
[72]	20CrMo	10–150	Finite element simulation	The increasing degree of grinding force at low speed is obviously higher than that at high speed
[120]	18CrNiMo7-6	60–160	Residual stress	The v_s has the greatest influence on the residual stress
Ni and Ni alloys				
[121]	Inconel718	65	Grinding force	Grinding force ratio increases and then decreases during grinding
[122]	GH4169	135	Grinding force	Single layer brazed CBN grinding wheel is more suitable for grinding difficult materials at high speed
[123]	Inconel 718	20–140	Grinding temperature	The optimal grinding wheel speed for Inconel 718 alloy grinding is 100–120 m/s
[107]	K4169 alloy	150	Grinding morphology	The K4169 alloy chips show a zigzag shape due to shear slip
Ti and Ti alloys				
[124]	TC4	60–150	Surface roughness	The surface roughness decreases as the v_s increases
[125]	Ti6Al4V	120	Grinding force	The grinding forces and specific energy decrease slightly while the v_s rises, whereas the grinding temperature increases
[109]	TC4-DT	60–120	Grinding force, temperature	The v_s and a_p have significant influence on TC4-DT
Composite materials				
[126]	YG8	80–160	Surface roughness	With the increase of v_s, the surface quality is improved
[127]	YG6	80–160	Grinding force	As the v_s increases, the grinding force decreases
[128]	PA30	80–160	Surface quality	The increase in the v_s leads to an increase in plastic marks on the surface of hard alloys and a decrease in brittle fracture
[129]	PTMCs	120	Grinding temperature	The empirical formula of grinding temperature was established: $T = 1.38 a_p^{0.55} v_s^{0.73} v_w^{0.31}$
[130]	WC-10Co4Cr	70–150	HSG force model	The average error rates of normal and tangential grinding force prediction are 6.29% and 5.55%
Hard and brittle materials				
[131]	Alumina	40–200	Surface roughness	Surface roughness of aluminum oxide decreases with increasing the v_s and decreasing working speed
[132]	Silicon carbide	20–140	Ductile grinding of SiC	The combination of v_s and a_p enables ductile grinding of silicon carbide
[45]	Glass-ceramics	30–150	Surface roughness	The v_s affects the surface roughness during grinding

that augmenting v_s attenuated the grinding scratch intensity on AISI 1045 steel surfaces when subjected to single abrasive grinding, as illustrated in Fig. 16b. Furthermore, Fan [69] discovered that reducing the a_p during the single abrasive grinding of AISI 1045 steel significantly enhanced the surface quality of the workpiece, a finding demonstrated in Fig. 16c.

Chen et al. [105] found that the residual stress and pressure first increased and then decreased with the increase of v_s during HSG of 18GrNiMo7-6 gear steel. Xiao [106] conducted HSG experiments on GCr15 bearing steel and found that tangential grinding force and surface roughness gradually decreased with the increase of v_s, and increased with the increase of v_w.

3.2 Difficult-to-machine material

Inefficiencies in machining performance and pronounced tool wear during the processing of challenging materials pose significant hurdles in various industries, including aerospace, automotive, and medical sectors. Materials notoriously difficult to machine, such as titanium alloy, GH4169 alloy, and K4169 alloy, are frequently employed in aerospace applications. HSG has been identified as an effective method for high-efficiency machining of these materials. In their study, Jiang and Liao [107] observed that during single-abrasive HSG of K4169 alloy, the rapid movement of abrasives induced shear slip in localized regions of the

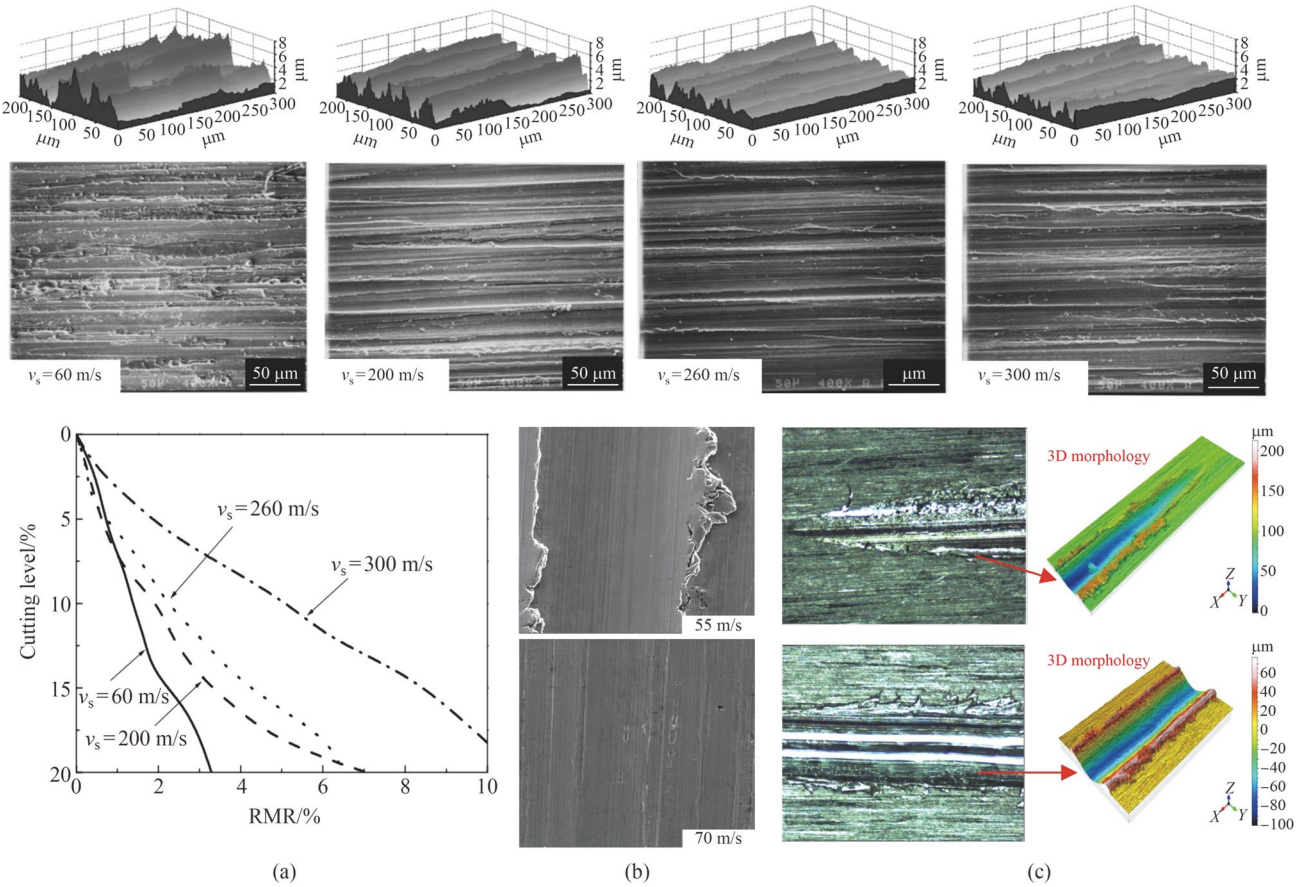

Fig. 16 Relationship between surface morphology of different alloy steel materials and v_s in HSG **a** surface morphology of JIS SUJ2 bearing steel obtained at different grinding speeds [104], **b** surface morphology of single abrasive grinding of AISI 1045 steel at different wheel speeds [47], **c** surface topographic characterization and 3D dimensional morphology of grinding gouges [69]

material, resulting in the formation of shear steps, as illustrated in Fig. 17.

Lin et al. [40] carried out single abrasive grinding of GH4169 alloy and showed that the chip formation line at v_s=165 m/s was more upwardly shifted than at v_s=100 m/s; the critical thickness shifted upward more; the skid marks in the grinding area were more pronounced; the plough zone build-up was higher and wider; the grooves were deeper; and the temperature and plasticity were increased, as shown in Figs. 18a, b. Cheng et al. [28] studied the surface wear characteristics of GH4169 during HSG, observed that the inlet and outlet patterns of abrasions formed by diamond abrasive cutting into and out of the workpiece surface were relatively regular at v_s=150 m/s. The surfaces of abrasions formed by the two types of abrasive were smooth and flat, with localized adherence phenomenon, which was more serious in the case of CBN abrasive, as shown in Fig. 18c.

Huang [108] found that grinding temperature was negatively correlated with workpiece speed and positively correlated with v_s and a_p when grinding titanium alloy TC4 at high speed; grinding force and surface roughness were negatively correlated with v_s and positively correlated with v_w and a_p. Xu et al. [109] conducted HSG of TC4-DT and found that the better grinding surface morphology could be obtained when v_s=60–80 m/s, due to high grinding temperature, the grinding surface was prone to surface burns, microcracks and other thermal damage defects when v_s=100 m/s, as shown in Fig. 19a. Xiao [42] conducted HSG experiments on TC4 and found that with the increase of v_s, the grinding force decreased; the adhesion and adhesion plugging of the grinding wheel were reduced; the workpiece surface roughness decreased; and the cracks decreased, as shown in Figs. 19 b, d.

3.3 Hard and brittle materials

Traditional manufacturing techniques struggle to efficiently process engineering ceramics and other materials

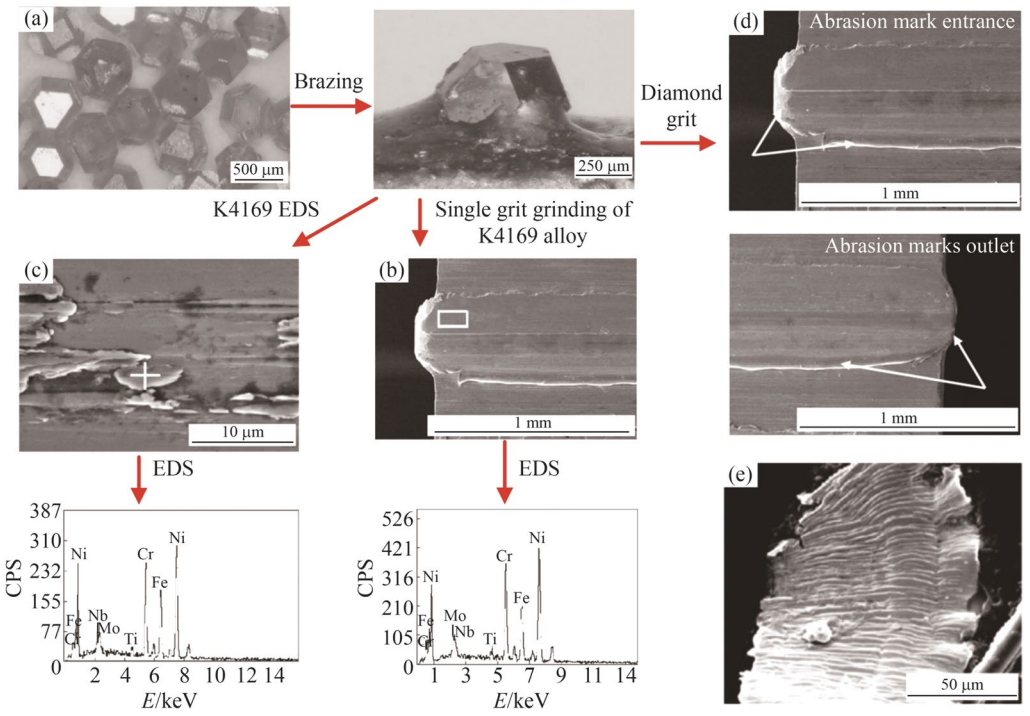

Fig. 17 Surface morphology of different difficult materials under HSG **a** macroscopic morphology of diamond abrasive and abrasive after brazing, **b** grinding morphology and energy spectrum analysis of K4169 alloy, **c** scanning electron microscope morphology of K4169 alloy under HSG, **d** grinding morphology of K4169 alloys under the action of diamond abrasive, **e** abrasive chip morphology of K4169 alloy under HSG [107]

characterized by high hardness and brittleness. HSG has emerged as a viable solution for machining such materials, finding applications in the biomedical, aerospace, and automotive industries. In the aerospace sector, advanced ceramics have demonstrated superiority over metallic superalloys in withstanding the extreme temperatures experienced by structural components and aero-engine parts. Beyond their capability to endure high temperatures, these advanced ceramics are renowned for their exceptional wear resistance, corrosion resistance, and chemical inertness. Shih et al. [110] observed that silicon nitride and zirconium oxide showed less wear of grinding wheels in HSG. Wu [111] found that the surface roughness of HT300 was better during HSG of HT300 and QT600-3 materials, as shown in Fig. 20a. Yin et al and Huang [112] found that the surface quality became smoother and smoother when grinding hard and ductile ceramics at HSG, as shown in Fig. 20b.

Dai [113] found that the plastic removal rate of the grinding surface increased with the increase of v_s, and the pit size, crack damage depth, grinding force and specific grinding energy of the grinding subsurface decreased when a single abrasive grinding was performed on SiC, as shown in Fig. 21a. Li et al. [45] found that the multi-step HSG processing technology of zero-dur glass-ceramics had obvious advantages in terms of material removal rate and surface roughness, as shown in Fig. 21b. Assuming that HSG is performed at different machining allowances, the material removal rate Q_w varies greatly, which the average value is as high as 1 528.3 mm^3/min, so that multistep HSG can easily obtain products with lower surface roughness, as shown in Fig. 21c.

3.4 Composite materials

Metal matrix composites (MMCs) constitute a new class of materials that are garnering significant interest across scientific, technical, and commercial domains. These composites exhibit superior specific strength and stiffness, augmented temperature resistance, and outstanding corrosion resistance compared to their non-reinforced metal alloy counterparts. Owing to these enhanced properties and the escalating performance requirements in various sectors, MMCs are increasingly being adopted as substitutes for traditional materials in a wide array of engineering applications within the aerospace, aircraft, electronics, and automotive industries [67]. Guo et al. [114] conducted HSG experiments on Al/SiCp MMCs and obtained better surface quality at high v_s, as evidenced by grinding

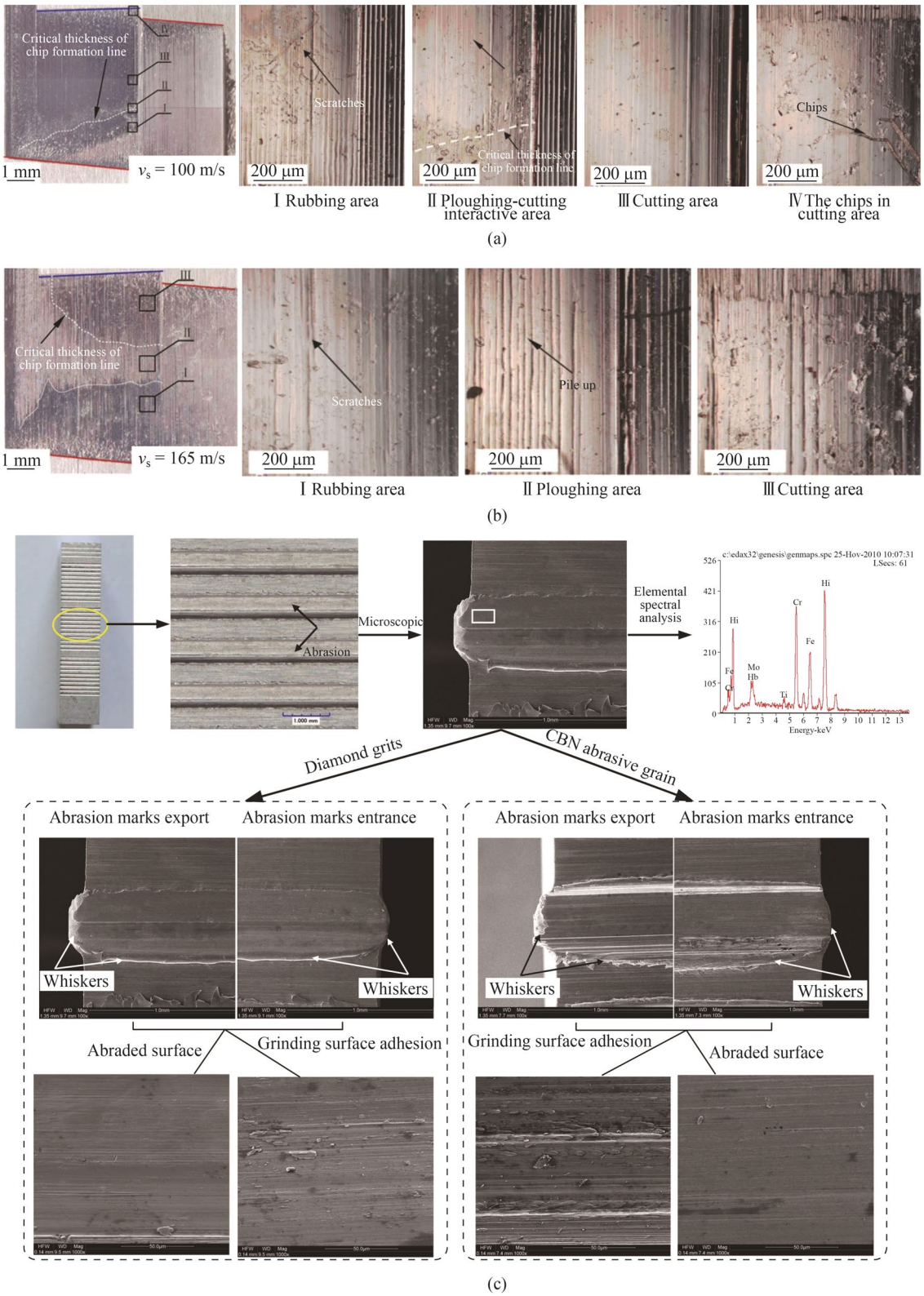

Fig. 18 Surface morphology of GH4169 alloy at different v_s **a** morphology of the surface and its detailed views at v_s=100 m/s [40], **b** morphology of surface and its detailed views at v_s=165 m/s [40], **c** macroscopic and microscopic morphology of the surface of GH4169 alloy, elemental energy spectroscopy, exit and entrance morphology of the abrasive marks formed by diamond abrasive and CBN abrasive, as well as microscopic morphology of the abrasive surface formed by the abrasive marks and adhesion phenomena (v_s=150 m/s) [28]

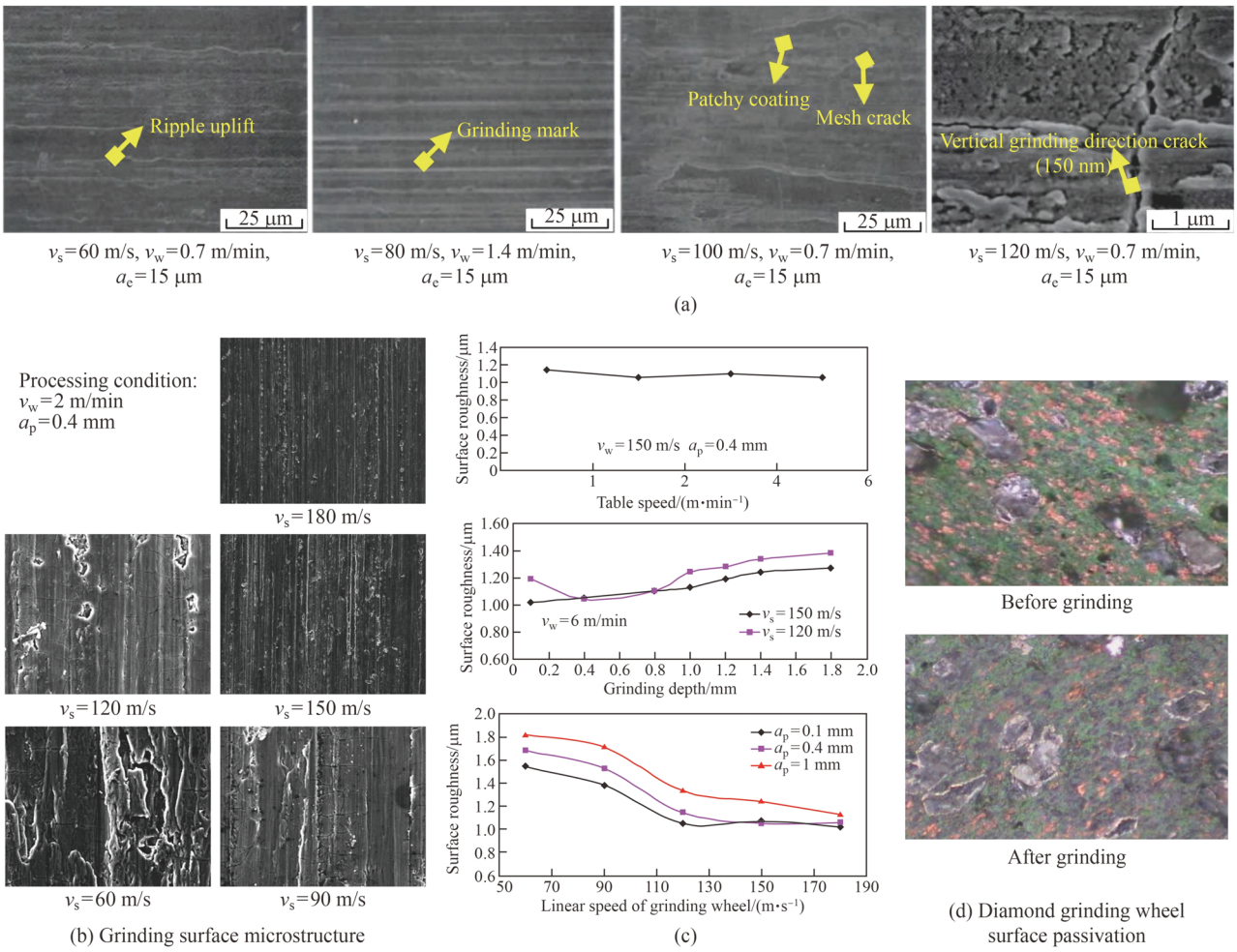

Fig. 19 Surface morphology of titanium alloy at different v_s **a** TC4-DT titanium alloy grinding surface topography [109], **b** effect of the v_s on surface morphology of titanium alloy TC4 [42], **c** influence of the v_s, a_p and v_w on surface roughness [42], **d** grinding wheel morphology before and after grinding [42]

scratches, surface craters and lower surface roughness, as shown in Fig. 22b. Guo et al. [115] conducted HSG experiments on Al/SiCp MMCs and found that grinding scratches, chips, surface craters, and side streams were the main features of the grinding process due to the fragmentation and strong plastic deformation of SiC abrasives.

Abrasive-reinforced titanium matrix composite (PTMCs) is a kind of MMCs. Compared with traditional titanium alloys, PTMCs has high specific stiffness and high specific strength due to the addition of abrasive reinforced phase, and has broad application prospects in aerospace industry [116, 117]. Liu et al. [85] found that the material removal behavior of PTMCs in HSG process could be divided into plastic removal of matrix material, crack initiation of reinforced abrasives, crack propagation of reinforced abrasives and brittle damage of reinforced abrasives, as shown in Fig. 22a.

4 Improvement with using cooling/lubrication methods

In HSG operations, challenges such as inefficient heat dissipation, accelerated wear of the workpiece, and reduced lifespan of the grinding wheel complicate the machining process. An effective strategy to enhance surface quality under these conditions is the application of grinding fluid. This chapter delves into the utilization of techniques such as minimum quantity lubrication (MQL), nano-lubricant minimum quantity lubrication (NMQL), and cryogenic gas-liquid lubrication. These methods are instrumental in achieving lower grinding temperatures and mitigating environmental contamination at high grinding speeds, as elucidated in Fig. 23.

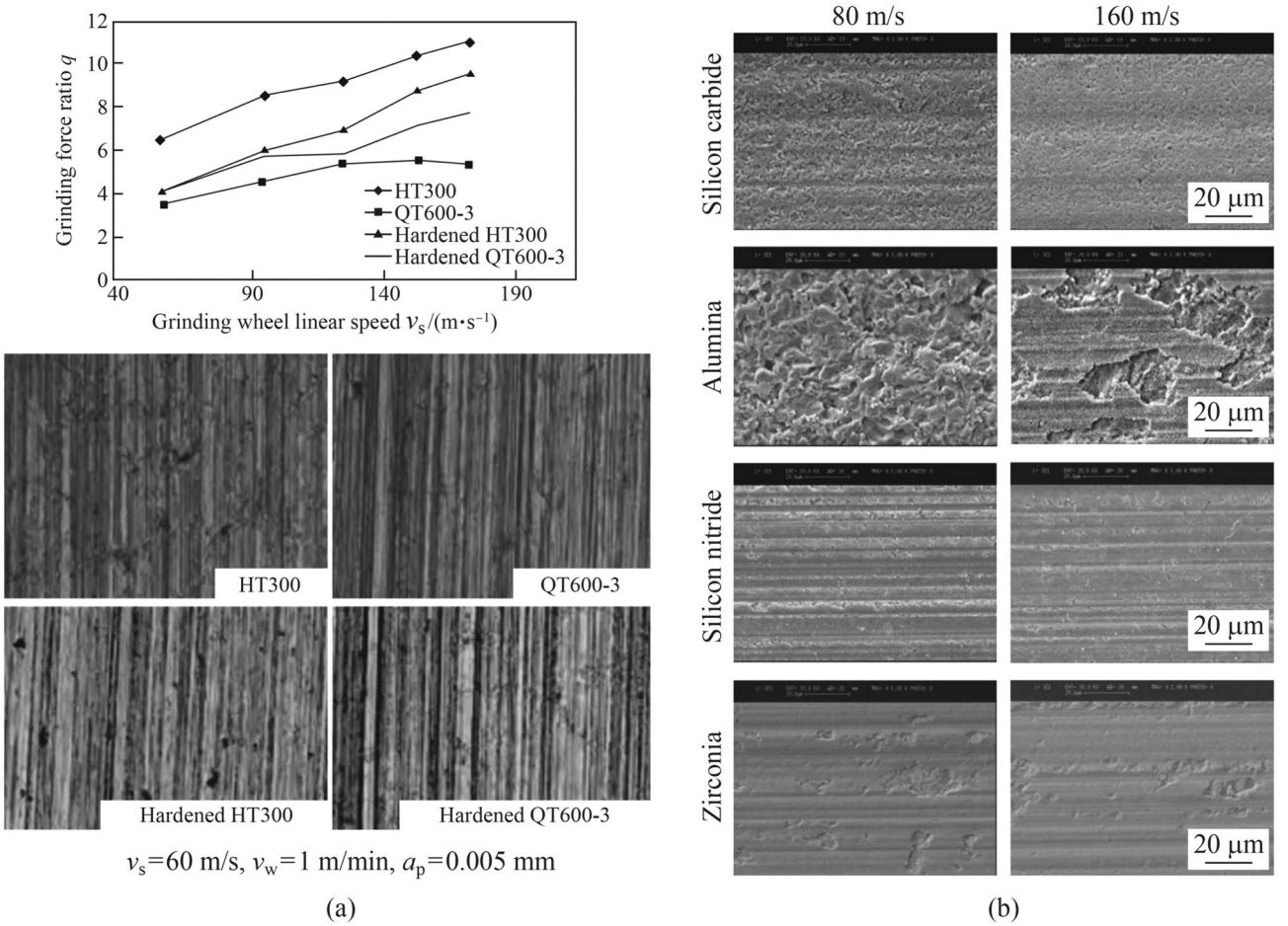

Fig. 20 Changes of surface morphology and grinding force ratio of hard and brittle materials under HSG **a** grinding force ratios of HT300, QT600-3, quenched HT300, and quenched QT600-3 materials at different v_s and surface morphology at v_s=60 m/s [111], **b** SEM micrographs of different materials grinding at different v_s

4.1 MQL

Coolant reduces the grinding zone temperature by removing heat from the grinding zone during the HSG, and access to the grinding zone is an urgent problem to be solved, so MQL comes into being. It can effectively enter the grinding zone to provide lubrication, thereby reducing the grinding zone temperature [133]. Boswell et al. [134] summarized the application of MQL in metal processing to improve machining performance. Tawakoli et al. [135] found that MQL could achieve a good reduction in grinding zone temperature when grinding hardened steel at low speed. Emami et al. [136] found that MQL could effectively reduce grinding force and surface roughness during the HSG. Choudhary et al. [133] found that HSG of alumina in different environments, low friction under MQL pure oil conditions increased the amount of plastic deformation in the grinding area, and its efficient grinding performance achieved high-quality grinding surfaces, as shown in Fig. 24.

Many researchers have found that several advanced ceramics can effectively reduce grinding forces and surface roughness at HSG [112, 137, 138]. Choudhary et al. [139] proposed a new model to demonstrate the interaction of nano-abrasives with brittle materials in the grinding area. Compared with other grinding environments, the straight cutting oil MQL has the highest tangential grinding force and the lowest normal grinding force, as well as the highest specific grinding energy and the highest apparent friction coefficient, as shown in Fig. 25.

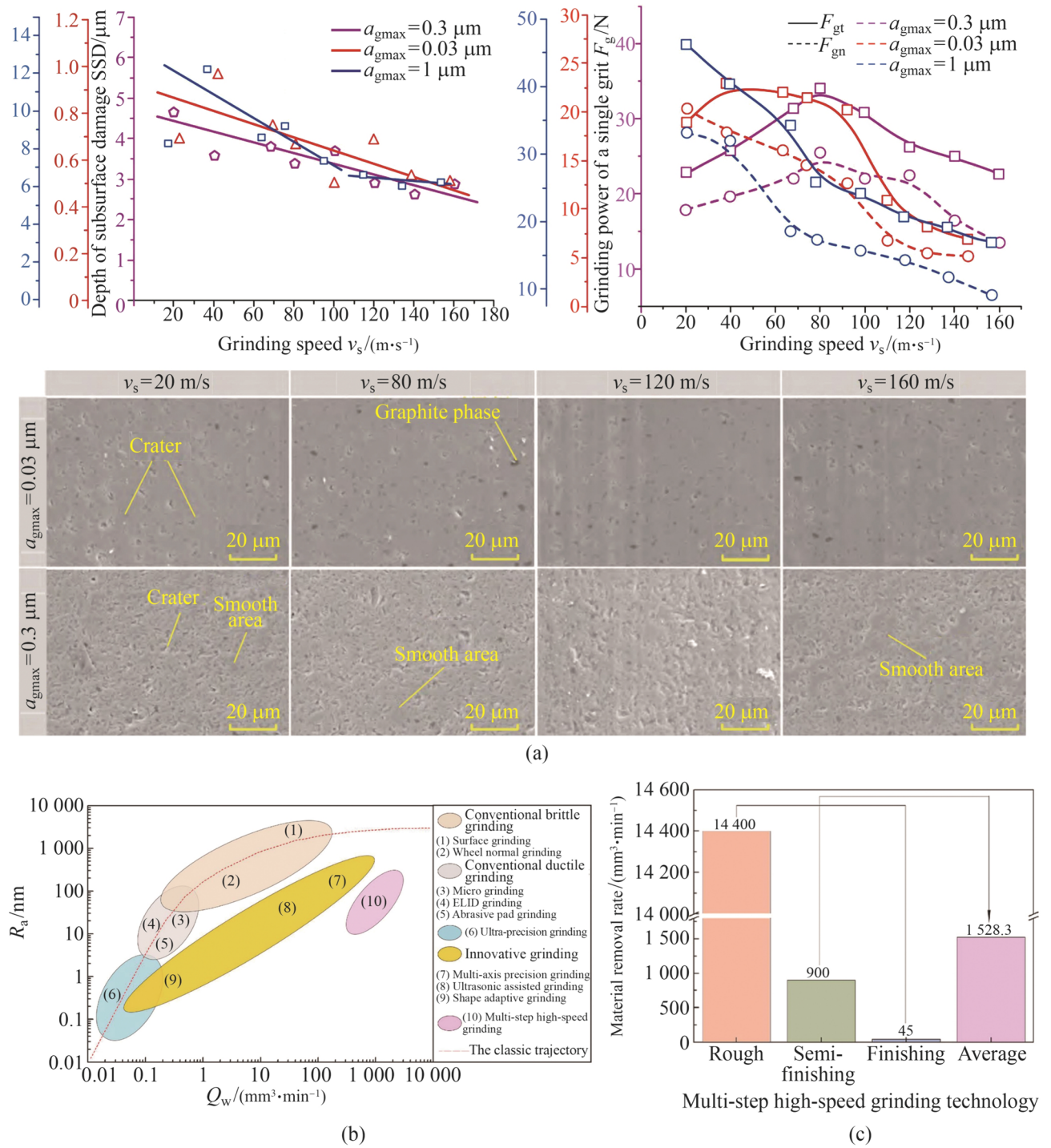

Fig. 21 Change of surface morphology of SiC ceramic materials and the change and advantages of multi-step HSG parameters **a** effect of v_s on surface damage, subsurface damage and grinding force of SiC [113], **b** advantages of multi-step HSG based on material removal rate and surface roughness [45], **c** multi-step HSG grinding parameter optimization [45]

4.2 NMQL

NMQL represents an innovative approach in precision grinding, characterized by its high efficiency, low resource consumption, environmental friendliness, and a low carbon footprint [140]. This method addresses the existing limitations in micro-lubrication applications. The inclusion of nano-abrasives significantly enhances the lubrication

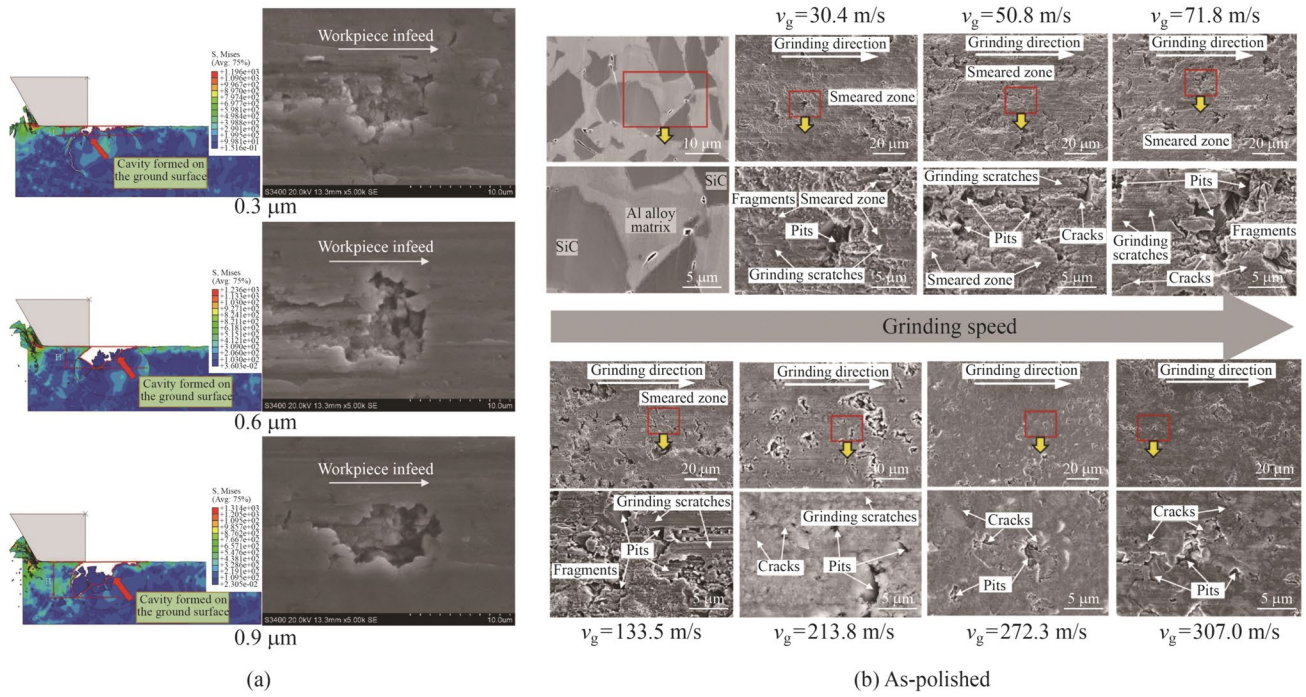

Fig. 22 Change of surface morphology and material removal behavior of composite materials under HSG **a** removal behavior of PTMCs material with different thickness of undeformed chips [85], **b** polishing surface and grinding surface of Al/SiCp MMC workpiece at different v_s [114]

efficacy within the grinding zone, owing to their exceptional anti-wear and anti-friction properties. This advancement not only improves the machining accuracy and surface quality of the workpiece, particularly in terms of surface integrity, but also ameliorates the working environment and boosts the heat transfer efficiency of MQL [141, 142].

Zhang et al. [55] conducted HSG experiments on a single abrasive in different grinding processes, and found that under three lubrication conditions, the scratch cutting efficiency increased with the increase of a_p, as shown in Figs. 26 a, b. Under different conditions, NMQL, due to its excellent cooling lubrication performance, reduces the temperature of the grinding zone and the thermal softening effect of the material to be removed, so that its deformation is more reflected in the fracture of the material, thus entering the cutting stage earlier, achieving higher grinding efficiency and lower unit grinding force, as shown in Fig. 26c. After measuring the scratched surface under different lubrication conditions, the cooling lubrication performance is improved under MQL condition, but the best workpiece surface and cooling lubrication performance are obtained under NMQL condition, as shown in Fig. 26d. Dry grinding formed banded chips due to the thermal softening effect; abrasive chip fracture due to excessive shear layer spacing occurred in the MQL condition; and the fracture was greater in the NMQL condition, as shown in Fig. 26e.

4.3 Cryogenic air

Cryogenic gas-liquid two-phase injection cooling is the use of cryogenic compressed gas to carry a small amount of coolant, spray impact jet injected into the processing area to achieve enhanced heat transfer cooling method. Its core is through the cryogenic spray jet to achieve cryogenic gas-liquid two-way strong convection, full vaporization and jet impact three enhanced heat transfer advantages, make full use of the cryogenic gas-liquid heat transfer potential to obtain a better enhanced heat transfer effect.

Wang [143] conducted HSG experiments on cryogenic gas-liquid two-phase injection technology and found that under the condition of cryogenic gas-liquid cooling, the heat in the grinding process was easily carried away by the vaporized droplets; the surface roughness value was lower; and the surface quality of the machined workpiece was better, as shown in Fig. 27a. With the increase of v_s, the grinding force under both cooling methods decreases; with the increase of v_w, the metal removal rate, cutting thickness, $a_{g\ max}$ and grinding force increase accordingly; with the increase of a_p, the $a_{g\ max}$ of a single abrasive and the length of the workpiece-grinding wheel contact arc increase; the grinding force, and the number of abrasives involved in cutting increase; and the cryogenic gas-liquid grinding force is smaller, as shown in Fig. 27b.

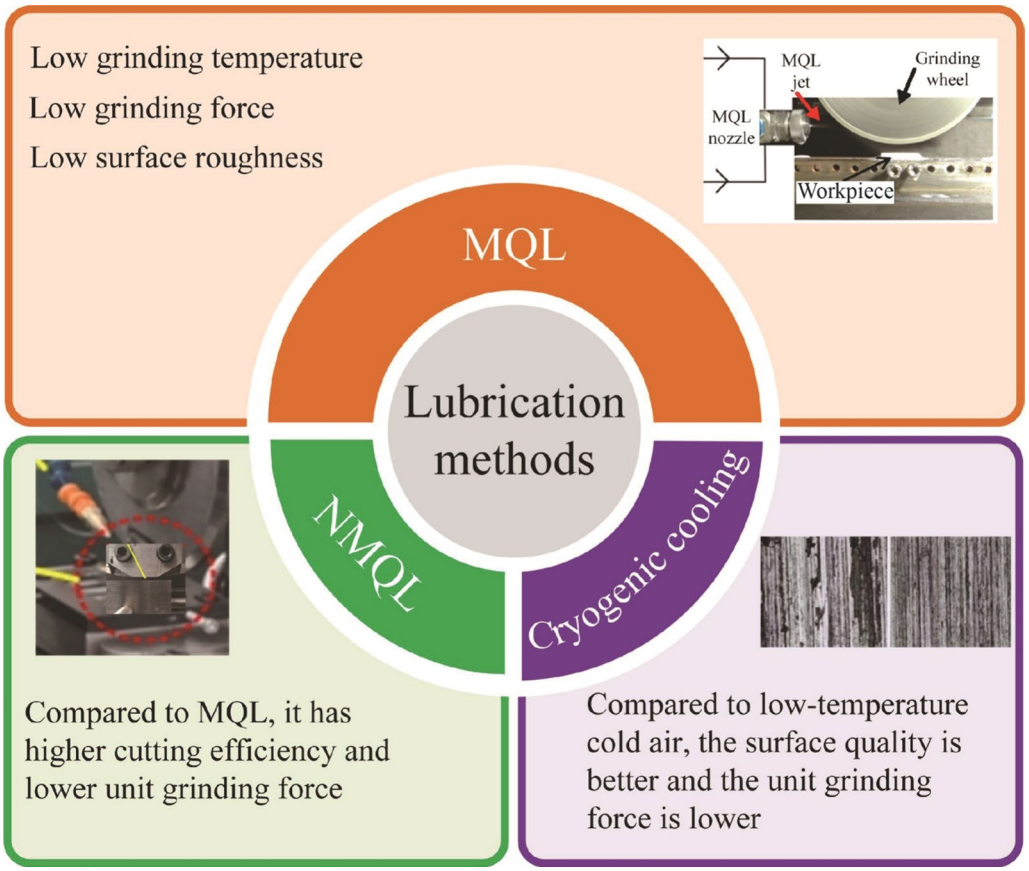

Fig. 23 Structure diagram of experimental results under different lubrication conditions of HSG

5 Key components of HSG grinder

The grinding machine tool is the primary instrument by which high-end precision components achieve their surface and dimensional accuracy, and its manufacturing standards have emerged as a critical benchmark for assessing a nation's high-end manufacturing capabilities. In recent years, significant advancements in grinding technology, both domestically and internationally, have transformed conventional grinding grinders into the current high-speed machining systems, resulting in substantial enhancements in both grinding precision and efficiency, as depicted in Fig. 28.

For ordinary grinding machines, appropriate modifications are needed to enable the realization of HSG [144]. Some of the modifications and requirements include the incorporation of HSG wheel spindle bearings characterized by high rigidity [145], strong vibration absorption capabilities, and minimal temperature elevation. Additionally, there is a need for the augmentation of motor power, enhancements to the dynamic rigidity and vibration resistance of the entire machine tool. Other requirements include the addition of a dynamic balancing device for the grinding wheel adjustment, the implementation of reliable measures to bolster safety and security. Finally, the cooling system should be improved by elevating both pressure and flow rates to ensure that a sufficient quantity of coolant can be introduced into the grinding zone [146]. In this chapter, key components of high-speed machining are examined, as depicted in Fig. 29.

5.1 Structure and stiffness of main body

The traditional structure can result in significant vibrations due to the abrupt increase in spindle speed, leading to inadequate machining quality, buffeting, and increased wear of the grinding wheel. Hence, there is a necessity for the redesign of the support structure of the high-speed surface grinder.

The fundamental components of a grinding machine, such as the bed, column, grinding head, and table, among others, constitute the "major components". They are classified, based on their motion, into stationary supporting components for the bed and column, and mobile supporting components for the grinding head and table. In the case of the stationary supporting components, vibrations in these parts and the entire machine can be induced by dynamic forces, including the dynamic grinding force of the grinding machine, the table's inertia, and the imbalance of the

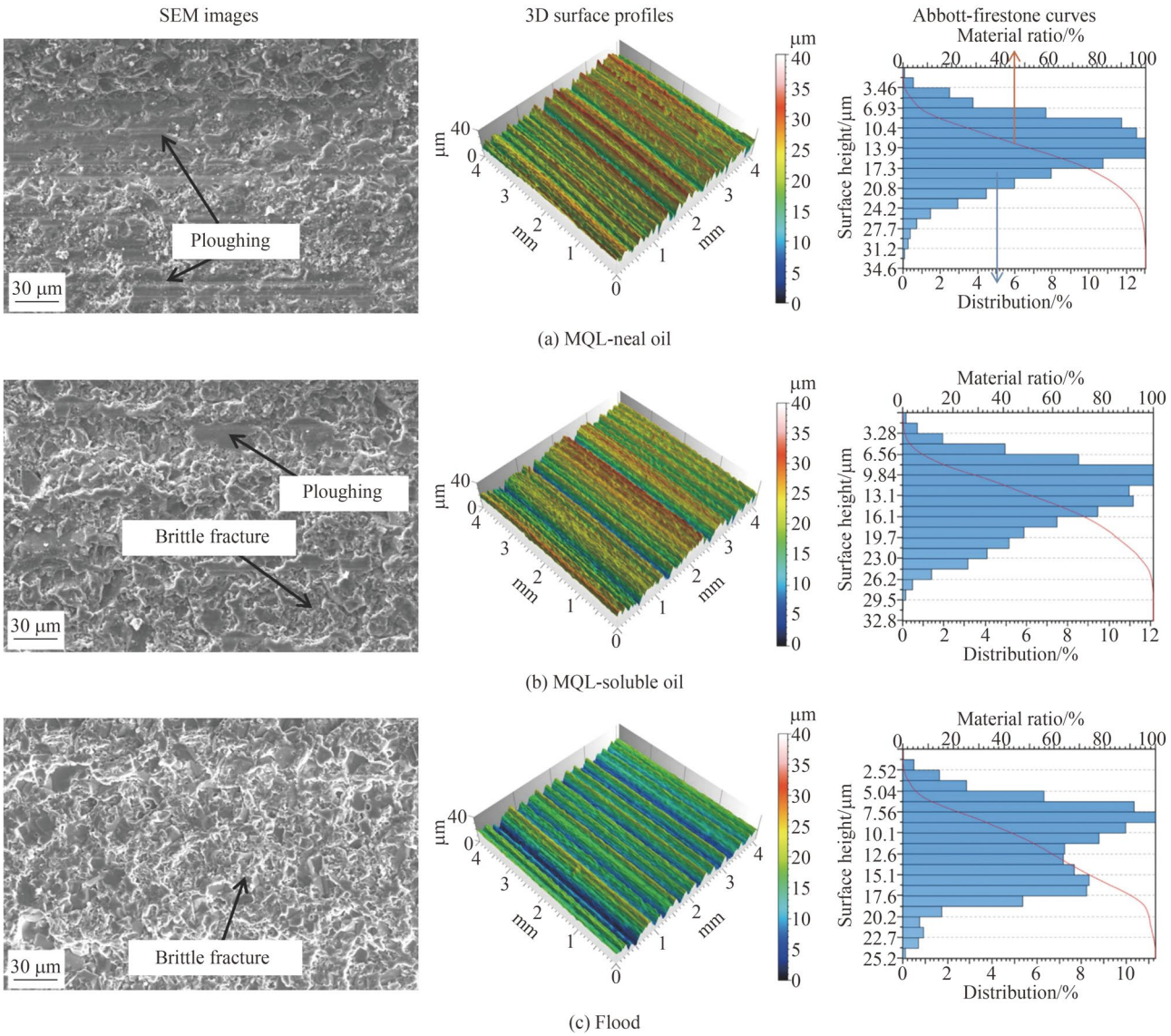

Fig. 24 SEM photos, three-position surface profiles and Abbots-Firestone curves of the ground alumina surface under different lubrication conditions (from left to right) **a** MQL-neal **b** MQL-soluble, **c** conventional flood [133]

grinding wheel. For HSG grinders, the potential for vibration generation increases significantly due to the substantial rise in v_s. It becomes imperative to ensure that the machine's inherent frequency remains beyond the v_s range, thereby necessitating a more rigorous design of the supporting components. In HSG machining, although the grinding force is generally lower compared to conventional grinding, the unbalanced force stemming from the high acceleration and deceleration inertial forces of the grinding wheel is substantial. As a result, sizable components, such as the grinding machine's bed, must possess adequate rigidity and strength. In the design of moving support components, a significant reduction in weight is imperative to ensure the high-speed operation and acceleration of these moving parts. The weight of the grinding machine supports should be reduced by 30%–40% compared to conventional grinding machine structures. This reduction should be achieved through the incorporation of highly rigid fixed supports and lightweight kinematic supports, allowing HSG grinders to exhibit dynamic characteristics that are tenfold higher than those of ordinary grinding machines, as illustrated in Fig. 30.

High-speed machine structures can be optimized by using lightweight or welded steel structures for movable parts, and whole-cast bed post structures to enhance stiffness and vibration resistance. Incorporating new materials like epoxy resin, polymer concrete, and high-nickel cast iron with lower thermal expansion can further improve vibration resistance and thermal stability [149]. The adoption of novel

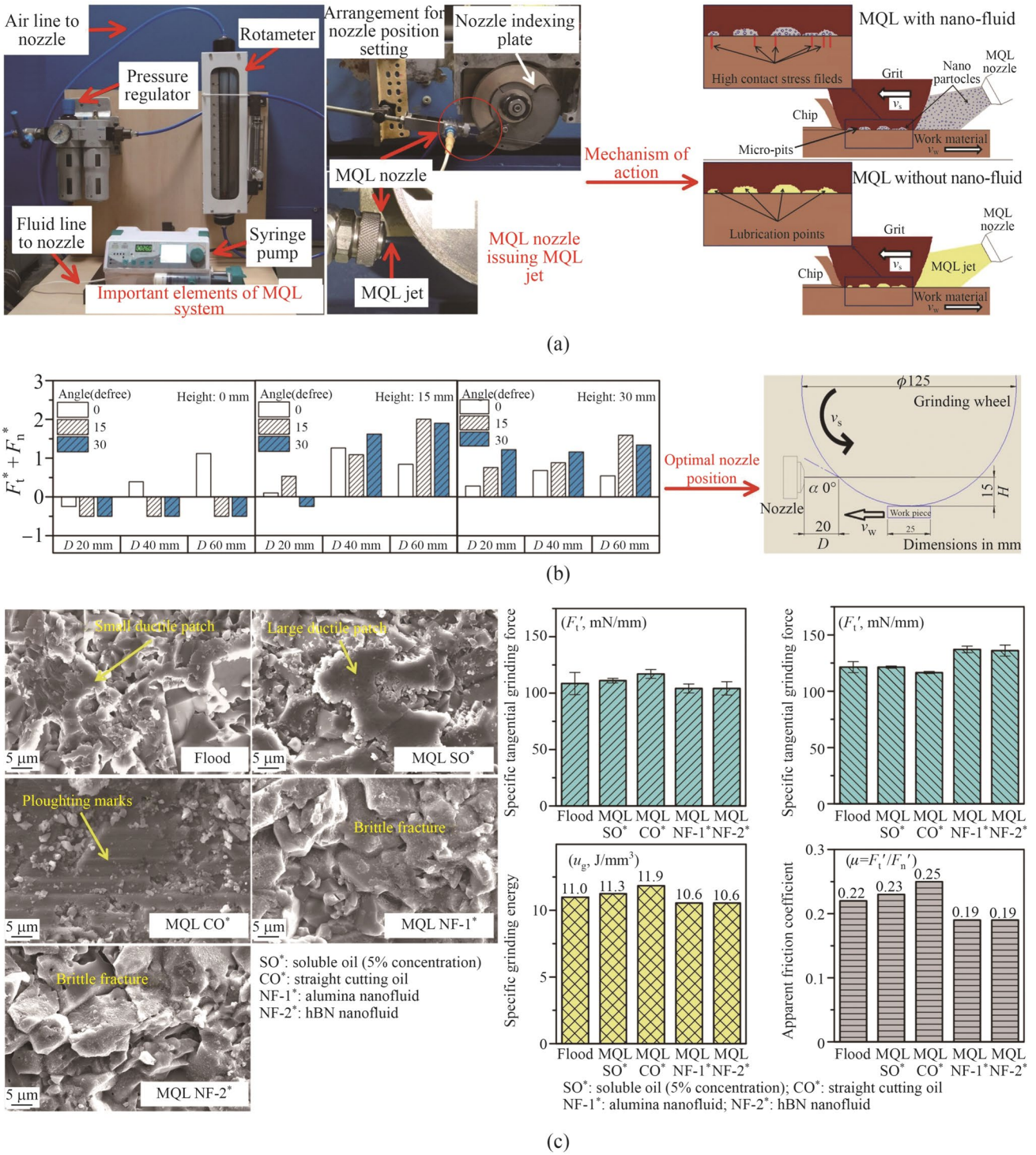

Fig. 25 Grinding mechanism and morphological changes in high-speed grinding using MQL lubrication **a** mechanism of MQL in grinding of hard and brittle materials, **b** effect of different nozzle orientations on the sum of non-dimensional grinding forces, and optimum MQL nozzle position, **c** effect of HSG alumina on surface quality in different grinding environments [139]

principles in motion mechanisms, exemplified by Giddings & Lewis's introduction of the parallel machine known as the Variax machining center, also referred to as the Hexapod, a six-legged machine, and the virtual axis machine. These innovations have emerged as significant advancements in the construction of the new generation of grinders.

The grinding process in high-precision grinding machines demands excellent performance characteristics, including

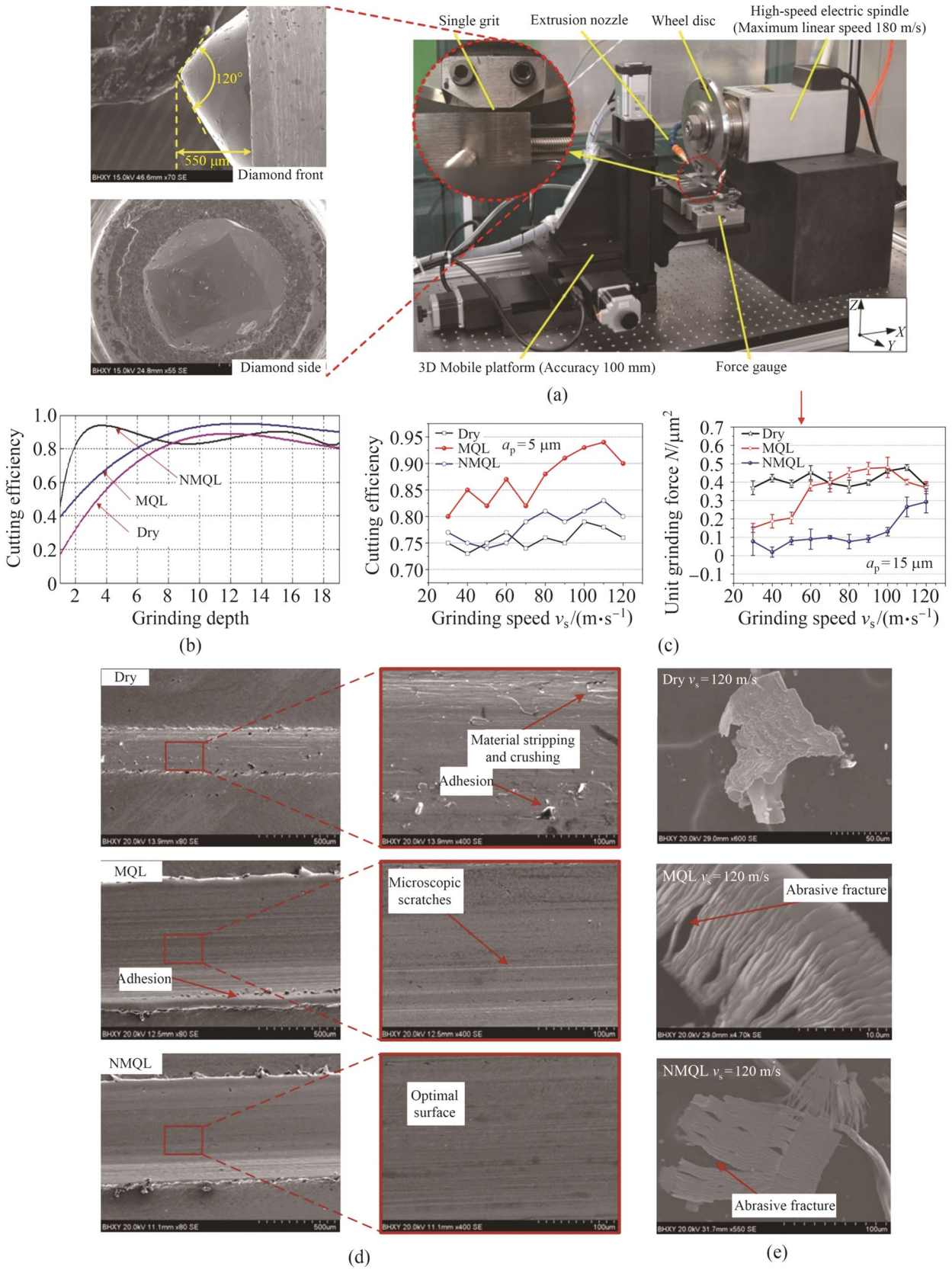
120°
550 μm
Diamond front
Diamond side
Single grit
Extrusion nozzle
Wheel disc
High-speed electric spindle
(Maximum linear speed 180 m/s)
3D Mobile platform (Accuracy 100 mm)
Force gauge
(a)
Cutting efficiency
Grinding depth
NMQL
MQL
Dry
(b)
Cutting efficiency
Grinding speed v_s/(m·s^{-1})
Dry
MQL
NMQL
a_p=5 μm
Unit grinding force N/μm^2
a_p=15 μm
(c)
Dry
Material stripping and crushing
Adhesion
Dry v_s=120 m/s
MQL
Microscopic scratches
Adhesion
MQL v_s=120 m/s
Abrasive fracture
NMQL
Optimal surface
NMQL v_s=120 m/s
Abrasive fracture
(d)
(e)

◂**Fig. 26** Changes of grinding mechanism, grinding force, surface morphology and grinding chips in NMQL lubrication HSG **a** experiment platform of single abrasive cutting test and surface morphology of single diamond abrasive, **b** the effect of the a_p on grinding efficiency, **c** cutting efficiency and unit grinding force under different working conditions, **d** furrow morphology at different lubricating conditions, **e** debris morphology at different lubricating conditions [54]

high precision and stability. To fulfill these requirements, the bed, as a supporting component, needs to possess robust stiffness, thermal stability, and damping properties. Grey cast iron is widely employed in grinder manufacturing due to its favorable attributes such as excellent castability, resistance to abrasion, vibration damping, compressive strength, machinability, minimal volume shrinkage, line shrinkage, and low notch sensitivity. Moreover, as the manufacturing industry advances, materials such as marble, concrete, and steel-fiber-reinforced polymer concrete have been explored for application in grinder beds. Table 4 provides a summary of the physical parameters of these four materials, which are used for analysis and comparison of the dynamic properties of the beds [150–155].

The mechanical structure of the bed remains unaltered, and the dynamic characteristics of the bed crafted from marble are the most superior, followed by those of the beds constructed from HT200 and steel-fiber-reinforced polymer concrete, with the plain concrete bed exhibiting the least desirable properties. Upon comparison, it becomes evident that among the four materials, marble is the most suitable for the fabrication of grinding machine beds due to its exceptional dynamic performance. However, due to its substantial size and higher cost, its practical application is limited. Among the four materials, HT200 offers dynamic performance that falls short of marble but surpasses that of steel-fiber-reinforced polymer concrete and conventional concrete. Additionally, it facilitates the casting of large mechanical structural components in a single operation, making it a commonly utilized material in practice. In actual design, one should thoroughly consider the inherent advantages of each material and incorporate them into the design of critical structural components.

5.2 Structure and rotate speed of spindle

The spindle system comprises the spindle, bearings, spindle motor, drive controller, encoder, and the corresponding communication cable, with its dynamic behavior being influenced by the stiffness of the bearing support and the spindle's own structure [32]. Chen [32] established the finite element model of the HSG grinding machine's spindle and generated vibration pattern cloud diagrams for both unconstrained and constrained conditions. In the constrained state, the frequency of the low-order modes is slightly lower compared to that in the free state. However, the maximum modal displacement is notably reduced, indicating a relationship between the spindle's vibration characteristics and its constrained state. The low-order vibration modes predominantly manifest as bending deformations in various directions, with the maximum displacements primarily occurring at the end of the smaller shaft. Therefore, the improvement of shaft structure can enhance resistance to bending deformation, as depicted in Fig. 31d. Mei [156] found that the grinding electric spindle converted electrical energy into mechanical energy through the built-in motor, and directly acted on the workpiece through the grinding wheel installed on the rotor spindle, making the structure more compact and the transmission accuracy higher [157].

Yang [39] designed a motor-built HSG spindle and carried out finite element static structural analysis in Ansys software, as shown in Fig. 31a, where a vertically upward force was applied to the wheel mounted on the front section of the spindle, and by analyzing the radial deformation cloud diagram of the spindle, the static stiffness value of the spindle could be calculated, as shown in Fig. 31b. According to the results of finite element analysis, it is found that the simulated values of the modal parameters of the whole machine are close to the test values, and the corresponding error between the two is less than 10%, as shown in Fig. 31c. The results show that the optimization and identification results based on the main components such as spindle column and linear motor driving platform can reflect the dynamic characteristics of the grinder of the HSG test equipment.

During the operation of the grinding electric spindle, thermal deformation is induced by the heat generated from the electromagnetic losses of the integrated motor and bearing friction losses, which in turn diminishes the machining accuracy of the grinding electric spindle. Within the grinding electric spindle system, the stator and rotor constitute the primary sources of heat generation for the integrated motor. The effective input power of the integrated motor is as follows

$$P_i = \sqrt{3}UI\cos\varphi. \tag{34}$$

During the operational process of the built-in motor, a significant portion of the effective input power is converted into effective output power to drive external loads, while the remaining portion is transformed into thermal energy and consumed, resulting in motor heating. This consumed energy is referred to as motor losses. The integrated motor used in the introduced grinding spindle is a permanent

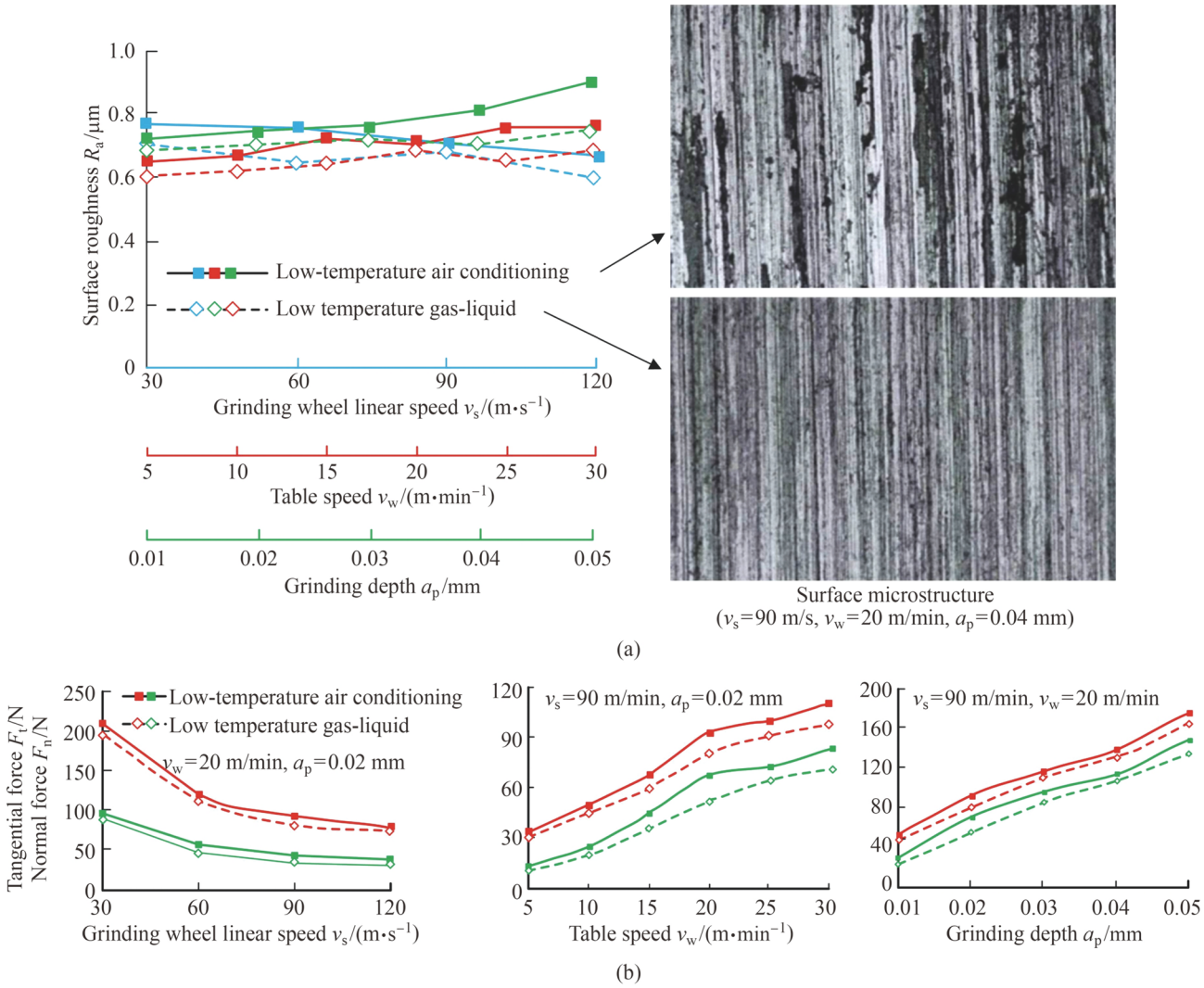

Fig. 27 Changes of surface morphology and grinding force during HSG in low temperature gas-liquid environment **a** variation of surface roughness with the v_s, v_w, a_p and surface microstructure under specific conditions, **b** variation of grinding force with the v_s, v_w, a_p [143]

magnet synchronous motor, with primary motor losses encompassing mechanical losses, winding copper losses, stator core losses, permanent magnet eddy current losses, and additional losses, as shown in Fig. 32 [158], where the additional losses account for only 1%–5% of the motor losses, and therefore can be ignored [159]. The stator core loss is categorized into hysteresis loss and eddy current loss, with eddy current loss further divided into classical eddy current loss and additional loss [158, 160]. Hysteresis loss occurs when the stator core is magnetized by the alternating magnetic field, resulting in friction between magnetic domains and consequent loss. Classical eddy current loss arises when the stator core, subjected to alternating current, generates eddy currents due to closed inductive electromotive forces, leading to the loss known as eddy current loss [161].

Bearings are important mechanical basic parts that reflect the level of industrial development of a country [145, 166]. Magnetic levitation bearings separate the inner and outer rings from each other during rotation and do not produce friction losses due to contact, reducing the system temperature rise, but they are not suitable for large-scale use due to their high cost, as shown in Fig. 33a [170]. Zhang et al. [168] studied a new type of hybrid gas-powered bearing with high structural stiffness and viscous damping, as shown in Fig. 33b. Angular contact ball bearings can bear both axial and radial loads at the same time, with low cost and high limit speed ratio. Two-half inner ring four-point contact ball bearings have the advantages of bearing bidirectional axial forces, high stiffness and small occupied space, as shown in Fig. 33d [172]. Grinding spindle in high-speed operation, steel ball bearings will produce the gyroscopic

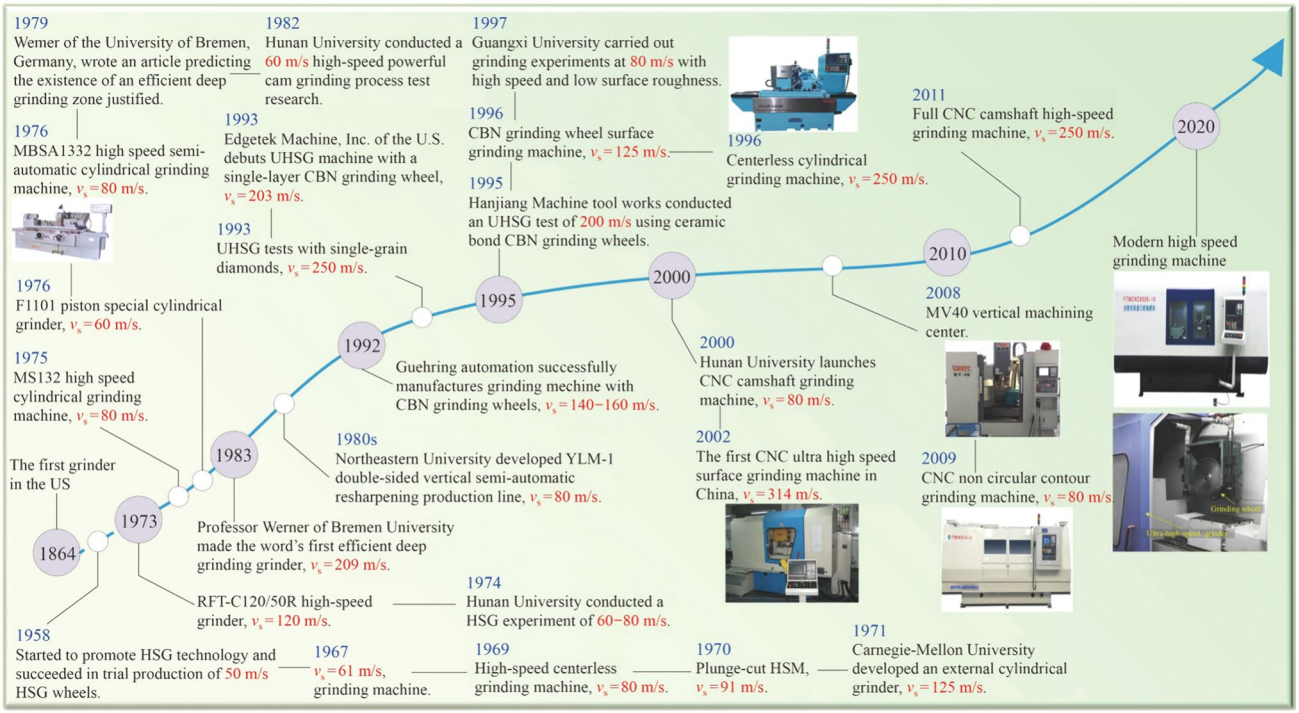

Fig. 28 Development of HSG grinder

torque and centrifugal force, increasing the contact stress, bearing temperature, fatigue pitting and thermal occlusion of the possibility of increasing, so that the bearing life is reduced, in the project more mixed ceramic ball to replace the traditional steel ball. Compared with steel ball bearings, ceramic ball bearings have the advantages of small density, non-conductive, non-conducting, low coefficient of friction, good wear resistance, long service life, self-lubricating and so on, as shown in Fig. 33c [171].

5.3 Structure and principle of dynamic balancing system

In order to meet the higher requirements of HSG, more and more attention is paid to the research of dynamic characteristics and dynamic balancing technology of grinding wheel spindle system [173, 174].

At present, there are three main types of more mature dynamic balancing techniques [36]. Process dynamic balancing: the use of balancing machine to detect and balance the spindle monomer by adding or reducing weight [175]. On-site dynamic balancing: balance the installed rotor system to avoid equipment installation and assembly errors [176]. Online automatic balancing technology: Install a balancing device on the rotor to detect the vibration of the rotor in real time [177]. There are two main types of auto-balancing technology [178]: (i) passive auto-balancing technology relies on the energy generated by the system response to drive the corrected mass, which has the advantages of simple structure and low energy consumption, but the device has the inherent defects of subcritical state exacerbating rotor imbalance and is difficult to design [179]. (ii) active auto-balancing technology achieves the unbalanced mass compensation by means of external energy [180].

Liang [36] found that there was a causal relationship between whether the mass distribution of the rotor was balanced and whether the centrifugal force of the rotor was balanced. They simplified the system of centrifugal force on the mass point of the rotor, reflecting whether the mass distribution of the rotor was balanced and symmetrical, as shown in Fig. 34a. The centrifugal force system of the rotor mass point is simplified to any point as a result of a total of five states, in addition to the rotor center of the main axis of inertia and the axis of rotation coincide with the rotor presents a balanced distribution state, the remaining four imbalance states, as shown in Fig. 34b. Assuming that there is a certain degree of unevenness on each disk axis of the rotor, the unevenness of the whole rigid rotor will be distributed along the *Z*-axis of the random space curve. No matter how asymmetric and uneven the mass distribution of the rigid rotor is, as long as there are two correction measures of concentrated distribution, the balance mass can be reduced or eliminated, which is the basic condition of the mechanical balance of the rigid rotor, as shown in Fig. 34c.

The span between the two bearings of the grinding spindle rotor system is large, and because the rotor body

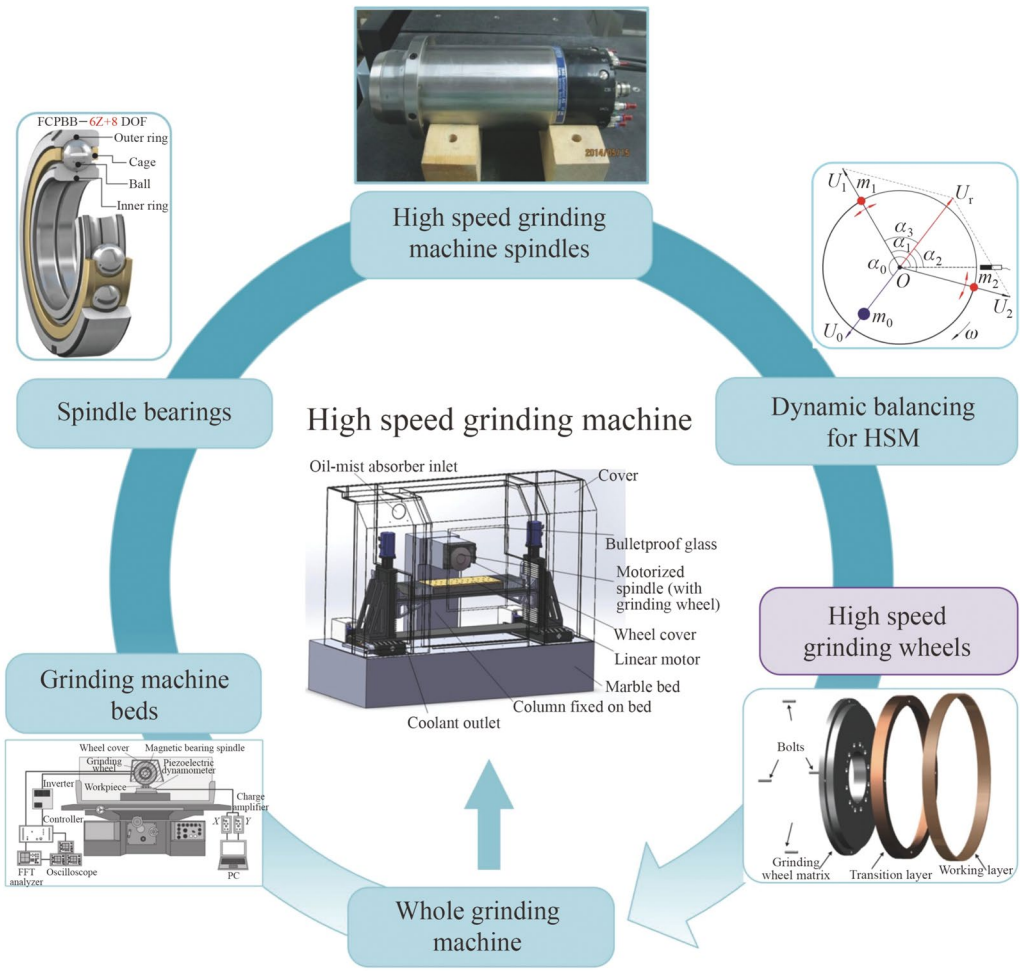

Fig. 29 Analysis structure diagram of HSG machine

rotates with a small axial runout, its imbalance is mainly manifested as its comprehensive imbalance. There are three ways to achieve on-line dynamic balancing including mass compensation method, coordinate rotation automatic balancing strategy and implementation of error analysis, as shown in Fig. 35.

The unbalance vector consists of phase and magnitude, so the error is mainly composed of phase error and magnitude error, assuming that the initial unbalance amount is U_0; the synthetic compensation of the counterweight mass block is U; and the step angle is φ. The phase error arises from the fact that no matter how to regulate the mass block, and it can not be compensated for its synthetic vector and the initial imbalance vector covariant, taking into account that the step angle is generally smaller; the residual imbalance vector and the initial imbalance vector are approximate orthogonal to each other; and the magnitude of the residual imbalance amount is approximated to be , as shown in Fig. 35d,

$$U_{\mathrm{r}} = U_0 \sin\left(\frac{1}{2}\varphi\right). \tag{35}$$

The amplitude error exists only when two counterweight masses are required to rotate simultaneously. After phase balancing, the two mass blocks are located at P_{11} and P_{22} or at P_{12} and P_{21}, respectively, which can be converted into a phase error by means of an optimized regulation algorithm, for example located at P_{12} and P_{21}.

5.4 Structure and strength of grinding wheel

HSG wheel is usually composed of substrate and abrasives with high mechanical properties, which should have good wear resistance, dynamic balance accuracy, crack resistance, damping performance, stiffness and thermal conductivity [19]. Materials with high elastic modulus/density ratio and low thermal expansion coefficient are sought in order to meet the performance requirements of HSG wheels. HSG wheels can be made of corundum, silicon carbide, CBN, and

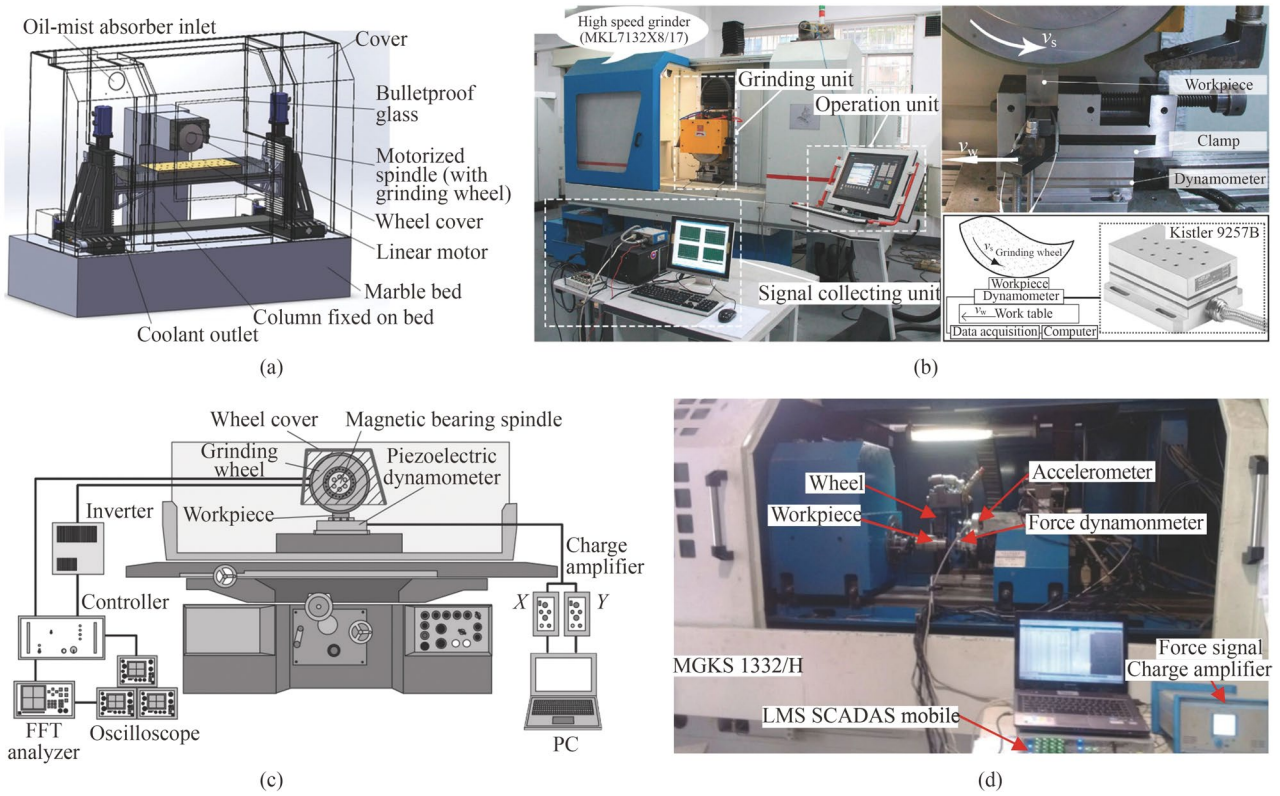

Fig. 30 Several types of HSG grinder **a** double-column HSG grinder [147], **b** zero multi-step HSG grinder, the max speed of the spindle of the machine tool reaches 10 000 r/min [45], **c** a grinding machine with an active magnetic bearing spindle, the max rotational speed and output power are 55 000 r/min and 7.5 kW [104], **d** the MGKS 1332/H CNC cylindrical-grinding grinder [148]

Table 4 Physical parameters of HT200, concrete, steel fiber polymer concrete and marble [32]

Material	HT200	Concrete	Polymer concrete	Marble
Density/ ($kg{\cdot}m^{-3}$)	7 200	2 400	2 400	2 800
Tensile density/MPa	250	50	12	200
Modulus of elasticity /GPa	120	24	30	70
Poisson's ratio	0.25	0.2	0.25	0.25

diamond abrasives, and the bond can be made of ceramic, resin, or metal bond [181]. The maximum speed of the grinding wheel using resin combined with corundum, silicon carbide and cubic boron nitride abrasive has reached 125 m/s; the maximum speed of the single-layer electroplated CBN grinding wheel has reached 250 m/s, which has reached 340 m/s in tests; and the maximum speed of the ceramic bonded grinding wheel has reached 200 m/s [182]. Compared to other types of wheels, ceramic-bonded grinding wheels are easy to trim and can be obtained with a wide range of porosity by changing the production process.

Performance requirements for grinding wheel substrates for HSG [39] including (i) static characteristics: the extremely high speed of the HSG spindle system and the small rotor diameter limit the power of the internal motor of the grinding spindle structurally; (ii) dynamic characteristics: higher natural frequency can improve the working speed of the spindle system in the resonance range; (iii) grinding performance: the grinding wheel substrate itself has good static and dynamic performance and dynamic balance.

Emerging applications of HSG technologies mainly include high efficiency deep grinding (HEDG), ultra high-speed grinding (UHSG), quick point grinding (QPG), and high-speed stroke grinding (HSSG). UHSG wheels consist of an abrasive layer and a grinding wheel substrate, and their working layer consists of a binder, a void, and an abrasive, and several typical grinding wheels, as shown in Fig. [36, 39, 181, 183–187].

CBN wheels including electroplated and brazed wheels, typically consist of a single layer of super abrasives nickel-coated or brazed filler bonded to a metal wheel substrate, as shown in Fig. 37a. Ghosh and Chattopadhyay [188] proposed a possible failure mode for CBN abrasive in electroplated wheels, as shown in Fig. 37b. At low levels of plating, abrasives are easily pulled out from the Ni-bond encapsulation, on the contrary at high levels of plating, abrasive failure is determined by the defect structure of the CBN abrasive. For single-layer brazed CBN wheels, abrasive pull out and

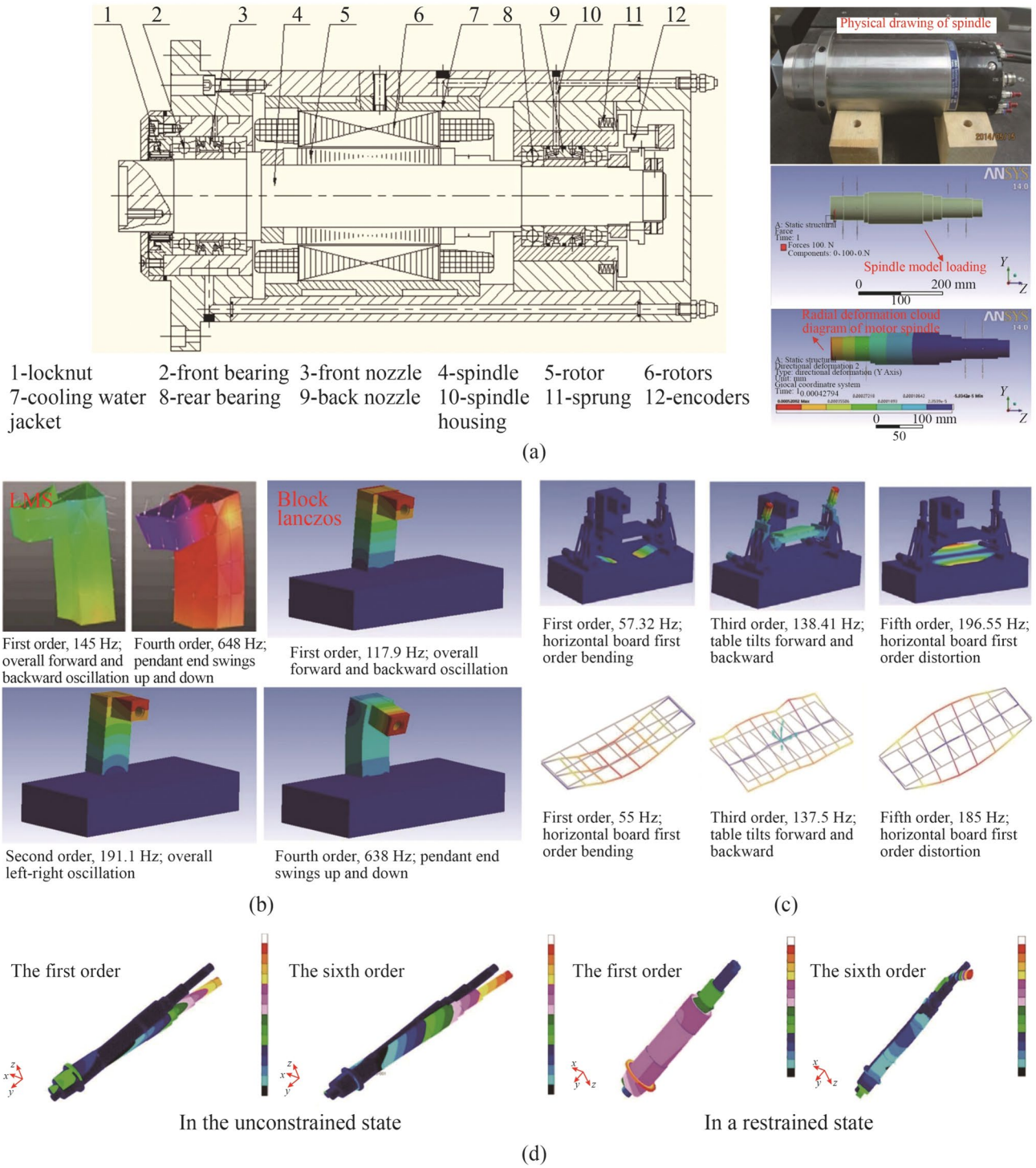

Fig. 31 Structure diagram and dynamic simulation model analysis of HSG spindle **a** general design unit diagram of electric spindle unit, **b** the first four orders of intrinsic frequency and vibration pattern of spindle column test mode and the results of finite element modal analysis of spindle column, **c** analysis results of the whole machine modal test and finite element mode shapes [39], **d** HSG grinding machines spindle finite element mode, the first and sixth orders of the spindle vibration pattern HSG grinding machines in the unconstrained state and in a restrained state [32]

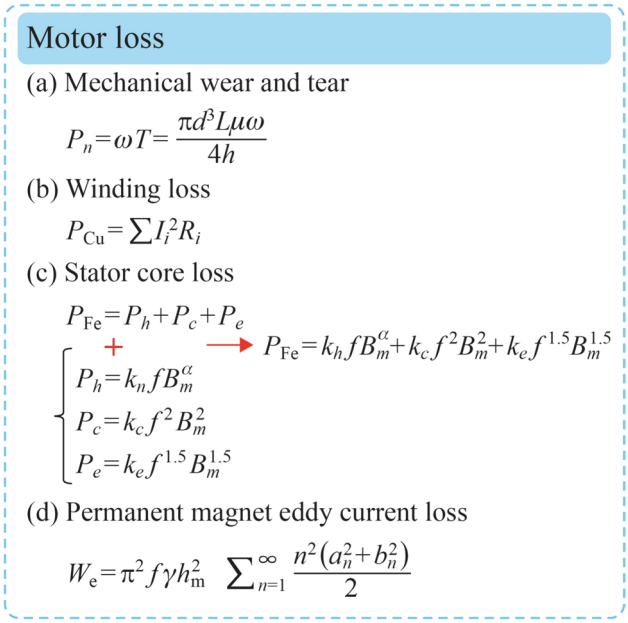

Fig. 32 Internal motor of the grinding spindle is the main motor loss in the permanent magnet synchronous motor **a** mechanical wear and tear [162], **b** winding loss [163], **c** stator core loss [156, 164], **d** permanent magnet eddy current loss [165]

bond shear may be due to poor surface wettability of CBN abrasives or low alloy strength, as shown in Fig. 37c [191].

There were three types of grinding wheel wear during the grinding, namely, abrasion, abrasive fracture and bond fracture [192, 193]. CBN wheels often have special requirements for resistance to breakage and wear resistance, and also require good damping characteristics, rigidity and thermal conductivity [194]. In this case, the HSG wheel usually needs to consist of a wheel body with high strength and a thin layer of CBN super abrasive coating, which is attached to the wheel body using a high strength adhesive, and only a single layer of CBN wheel can achieve the highest v_s. Electro-plated wheels consist of a single layer of abrasive, which enables maximal material removal rates, as shown inFig. 38 [195].

Liu et al. [196] proposed a fabrication process for brazed diamond grinding wheels, in which the blade portion of a diamond saw was brazed in a high-vacuum furnace, and then the brazed blade was welded to a steel substrate by laser, as shown in Fig. 39.

Based on CFRP material light weight, high specific strength, high specific modulus of elasticity, good damping and vibration resistance and other excellent properties. Yang et al. [197] found that the natural frequencies of each order of CFRP wheel were higher than the natural frequencies of the spindle system of steel-based wheel, and with the increase of v_s and v_w, the surface roughness of CFRP wheel was lower than that of steel-based wheel. Yang [39] conducted high-speed grinding tests with self-developed CFRP wheel and found that with the increase of v_s, the radial deformation and equal effectiveness of the substrate of CFRP wheel under three layering methods increased significantly, as shown in Fig. 40 [198]. Subsequently, an experimental study on HSG with CFRP wheel and rigid matrix wheel was carried out, and it was found that as the v_s increased, its no-load power consumption, radial deformation, amplitude and temperature of the grinding wheel substrate also increased. However, the ratio of no-load power consumption, radial deformation and amplitude of the CFRP wheel were lower compared to those of the steel matrix grinding wheel, and the gradient of the temperature rise of the CFRP wheel was significantly higher than that of the steel matrix wheel. The grinding force was reduced with the increase in the v_s, and the CFRP wheel produced a much lower grinding force [39].

6 Conclusions and prospect

6.1 Conclusions

By reviewing the progress of HSG, the MRM, machined surface integrity, grinding force and temperature, as well as the key equipment for HSG in the HSG process are summarized and discussed. The main conclusions are drawn as follows.

(i) Based on the MRM study of HSG, the deformation mechanism and mechanical behavior of workpiece materials in the abrasive forming area are sorted out. The calculation formulas of strain rates in the first and second deformation zones were established, and the mechanism of chip formation under the combined effect of strain hardening, strain rate strengthening and heat softening were revealed. The theoretical model of grinding force and grinding temperature is established. The effects of geometric parameters of simplified model on grinding force and grinding temperature were studied. The differences of material removal constitutive models and grinding properties of different workpiece materials under high strain rate were analyzed.

(ii) Through the study of surface topography of difficult-to-machine materials, hard and brittle materials, alloy steels and composite materials after HSG, it is found that the surface roughness of the surface roughness is better than that of conventional grinding, and the grinding force is smaller. The research of different workpiece materials is extended, which provides the basis for establishing the database.

(iii) In the HSG process, adding some cooling processes such as MQL, NMQL, cryogenic air, etc., will obtain

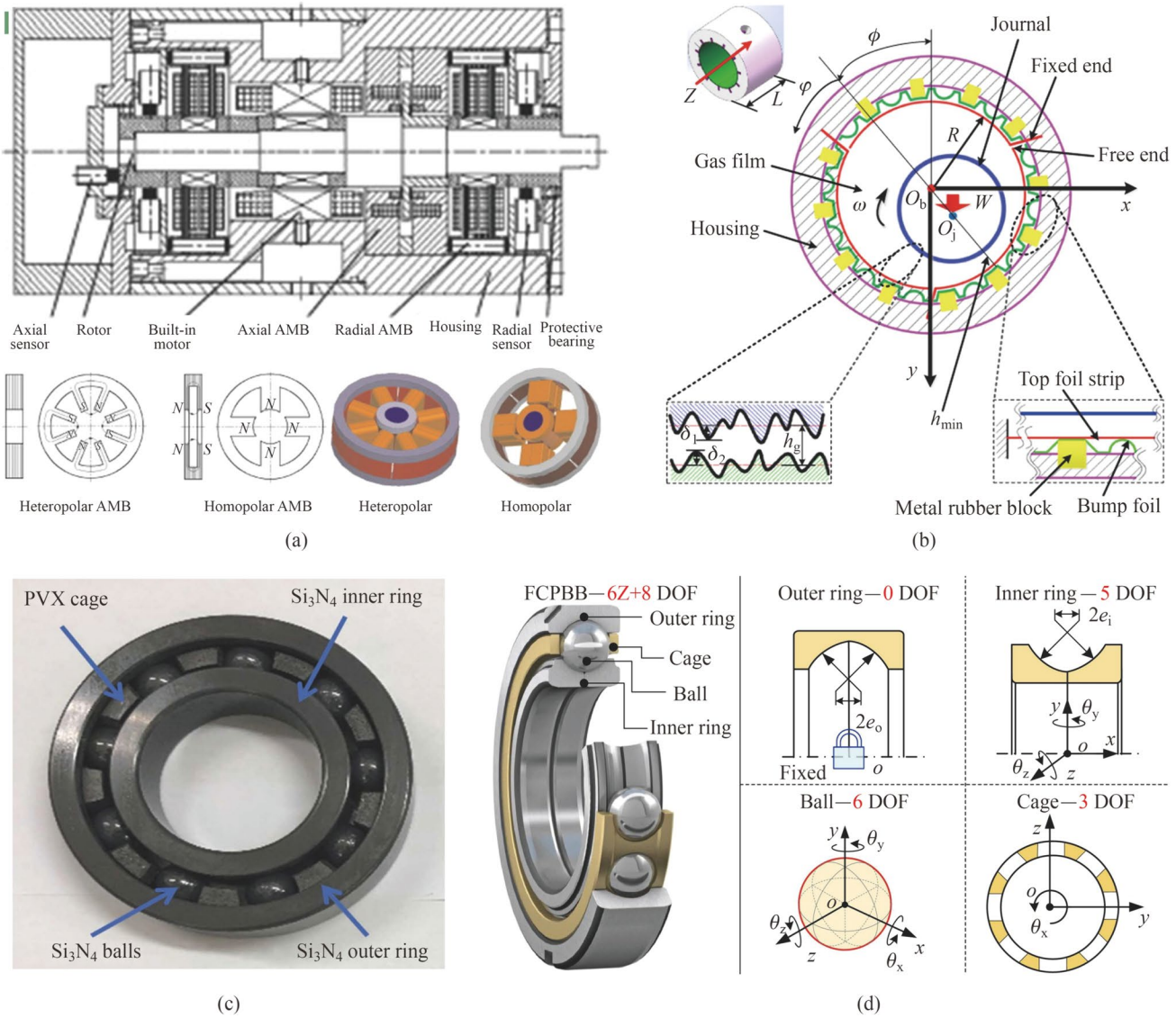

Fig. 33 Schematic diagram of different bearings used in HSG **a** mechanical structure of motorized spindle and schematic diagram of magnetic bearing [170], **b** schematic diagram of the novel hybrid gas dynamic bearing (HGDB) [168], **c** schematic diagram of ceramic ball bearing [171], **d** structural diagram of double half inner ring four-point contact ball bearings (FPCBB), which consists of outer ring, inner ring, cage and ball [172]

lower grinding force, grinding temperature and surface roughness than ordinary grinding. By comparing the surface roughness of three cooling processes: NMQL < MQL < cryogenic air, it is found that NMQL can obtain better HSG surface topography. In summary, NMQL has better cooling lubrication effect and surface quality after grinding.

(iv) The HSM from the supporting parts to the spindle, the grinding wheel is the main structure of the grinder, and HT200 material can be selected as the bed structure of the grinder. The dynamic characteristics of the main shaft, the conditions of the dynamic balance of the main shaft and the strength of HSG grinding wheel are described.

6.2 Prospect

In recent years, the research progress of HSG on MRM, material constitutive model, grinding force model, grinding temperature model, microstructural changes of typical materials under HSG, the laws generated by different grinding processes and the research progress in HSG key components such as the body mechanism, grinding wheels, spindles, dynamic balancing, etc., which has an important

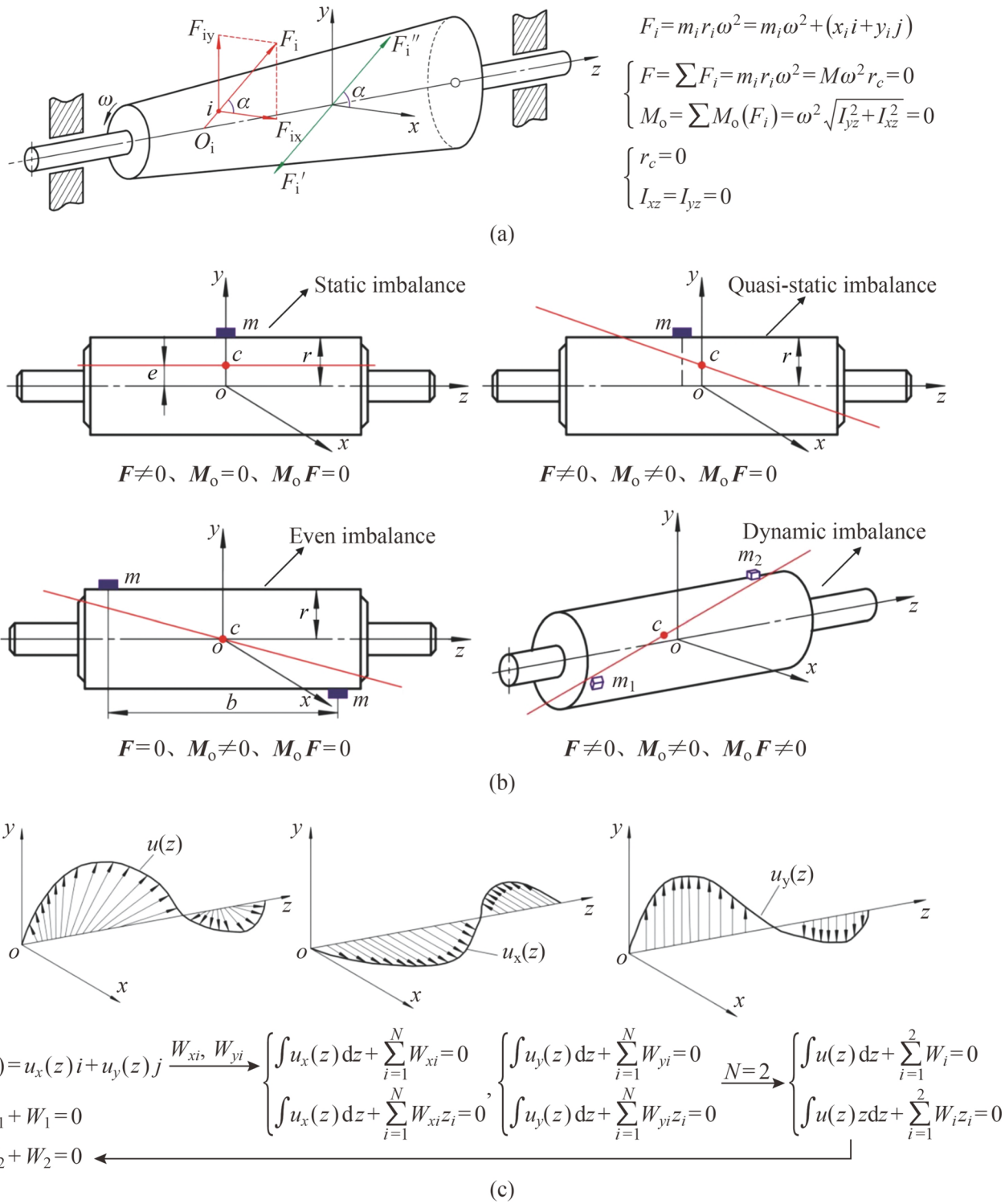

Fig. 34 Unbalanced state of spindle rotor and the corrective measures for balance **a** simplification of the centrifugal force system at the rotor mass point, **b** the rotor with four states of imbalance, **c** unbalance curves for rigid rotors [36]

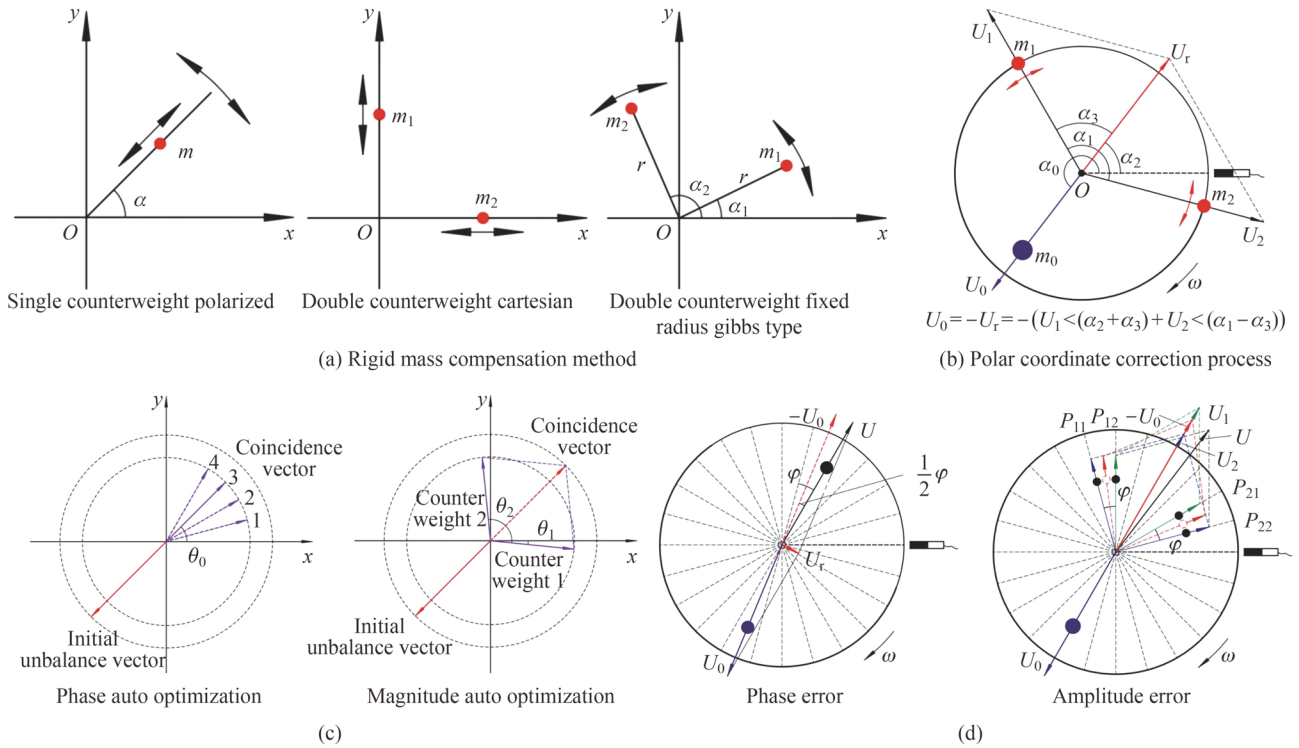

Fig. 35 Methods for realizing on-line dynamic balancing **a** mass compensation method, **b** polar coordinate balancing process with fixed radius for double counterweights, **c** coordinate rotation auto-balancing strategy, **d** execution error analysis [36]

practical significance at the present stage, and scholars still have a lot of work to do in this regard, as shown in Fig. 41.

Combined with the research review in this paper, several future research directions are proposed.

(i) The development trend of HSG is reviewed in this paper. By summarizing the strain hardening effect, strain rate strengthening effect and heat softening effect of materials produced by HSG, it is found that the increase of grinding speed brings some urgent problems to the research of grinding mechanism. At present, the constitutive model is found through the Hopkinson pressure bar test. As the increase of grinding speed, shear, plastic deformation and heat-affected zone formation, as well as the change of temperature and pressure in the grinding zone, lead to the change of physical properties of the material, which makes it difficult to establish the constitutive model and residual stress model of material removal. The material constitutive model needs to be theoretically simulated by molecular dynamics experiment and experimentally explored by a single abrasive slip test. For the efficient deep grinding combined with HSG and deep grinding, it is difficult to achieve high power and high speed of the spindle, which requires scholars to continue their research in the future. At present, due to the lack of some research data, the

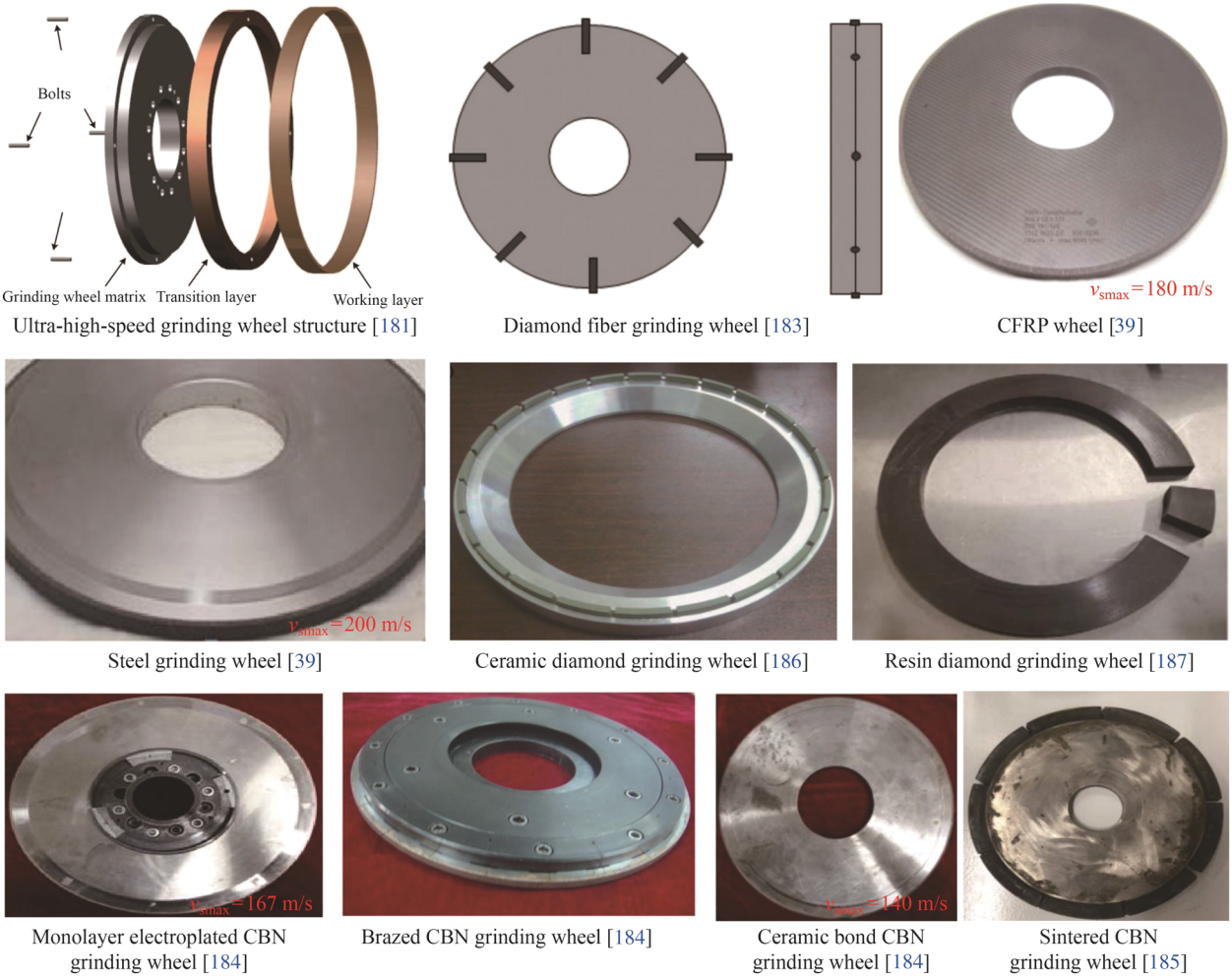

Ultra-high-speed grinding wheel structure [181] | Diamond fiber grinding wheel [183] | CFRP wheel [39]

Steel grinding wheel [39] | Ceramic diamond grinding wheel [186] | Resin diamond grinding wheel [187]

Monolayer electroplated CBN grinding wheel [184] | Brazed CBN grinding wheel [184] | Ceramic bond CBN grinding wheel [184] | Sintered CBN grinding wheel [185]

Fig. 36 Several typical HSG wheels [39, 181, 183–187]

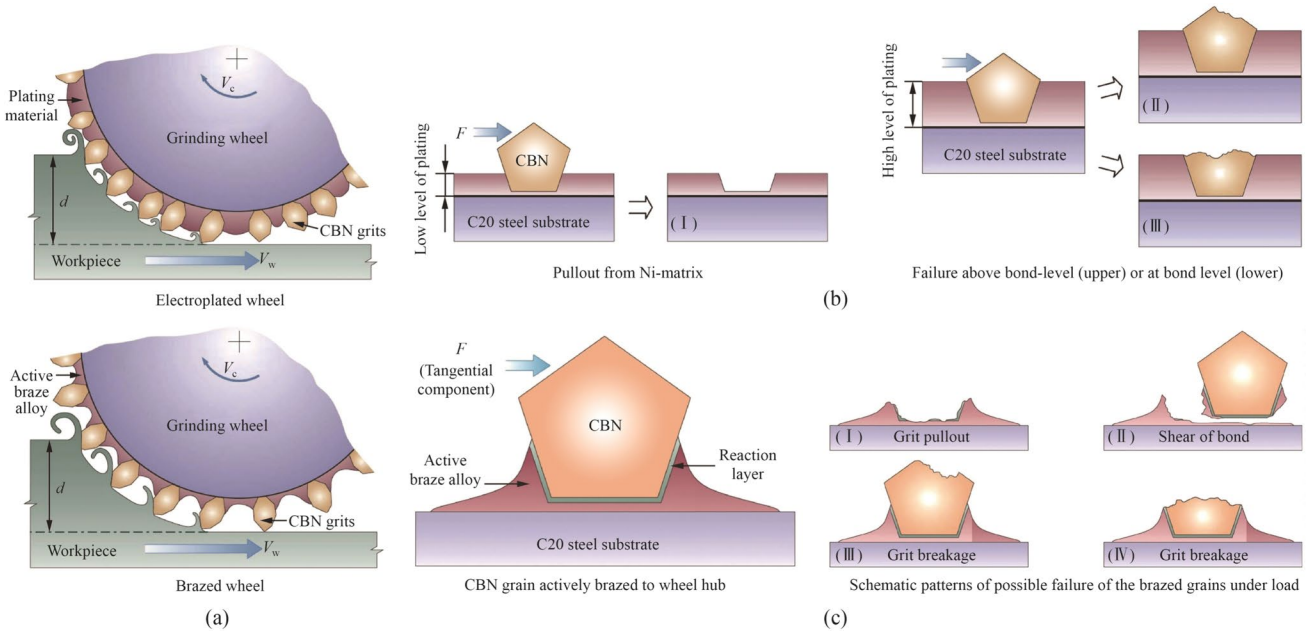

Fig. 37 Possible abrasive failure modes of single-layer brazed CBN grinding wheel and electroplated CBN grinding wheel **a** schematic diagram of single-layer plated and brazed CBN wheel, **b** possible abrasive failure modes in electroplated CBN wheels, **c** possible abrasive failure modes in brazed CBN wheels [191]

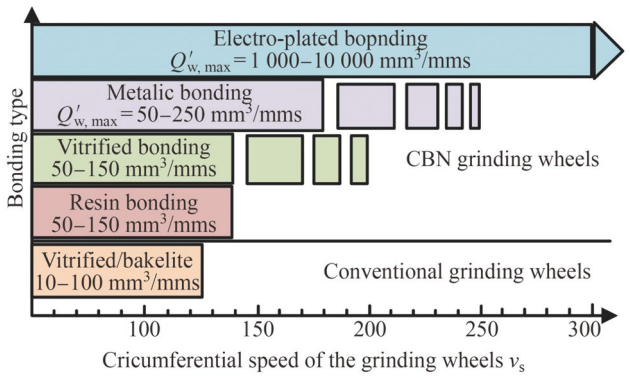

Fig. 38 Affordable the v_s and materials removal rates of different CBN wheels [195]

development law cannot be well summarized, and it is necessary to conduct a large number of research experiments on some difficult materials in the future, and establish a complete material constitutive model, residual stress model and other databases. In view of the complexity of the grinding force modeling formula caused by the change of grinding force under the action of HSG, it has become an urgent problem to be solved. At present, the measurement of grinding temperature is mostly through thermodynamic coupling, which is not accurate enough, and the heat source model of grinding temperature modeling has some limitations. Due to the increase of grinding speed, grinding temperature changes too fast, and the collection of grinding temperature in grinding zone is still a bottleneck to be explored by young scholars.

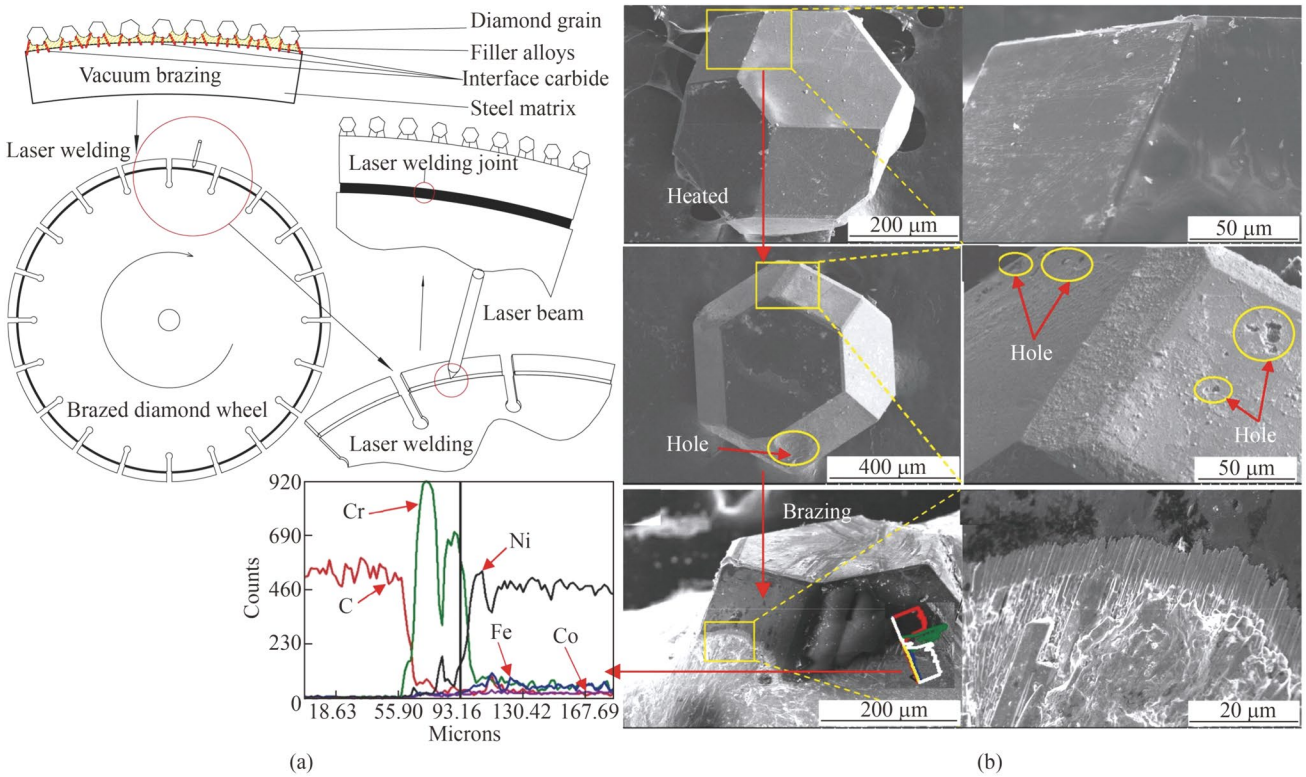

Fig. 39 Production process and microstructure of brazed diamond grinding wheel **a** production process of brazed diamond wheel, **b** initial, heated, and brazed microstructures of diamond abrasives [196]

The study of grinding chips is also a reliable way to determine the grinding mechanism. At present, it is difficult to collect abrasive dust at the current level of research, and future scholars will need to spend a lot of time to study the collection of abrasive dust.

(ii) An in-depth study of the material removal behavior of different types of workpiece materials under high-speed grinding, especially some difficult materials such as high-entropy alloys and composites used in aerospace. In order to better help future scholars to understand the research faster, the future needs to establish a complete database through the analysis of its system, including grinding force, grinding temperature, surface roughness, sub-surface roughness and grinding abrasive collection and research.

(iii) In this study, the research results of MQL, NMQL and HSG workpiece under low temperature cold air. In view of the limitations of the grinding process introduced at present, more new grinding processes can be introduced in the future, for example, For the nanofluids in NMQL, different additives, electrostatic atomization minimum quantity lubrication and electrostatic atomization minimum quantity lubrication (some low temperature cooling conditions can be added) can be selected, and efficient cooling lubrication methods can be found by studying different lubrication conditions under HSG and analyzing different grinding

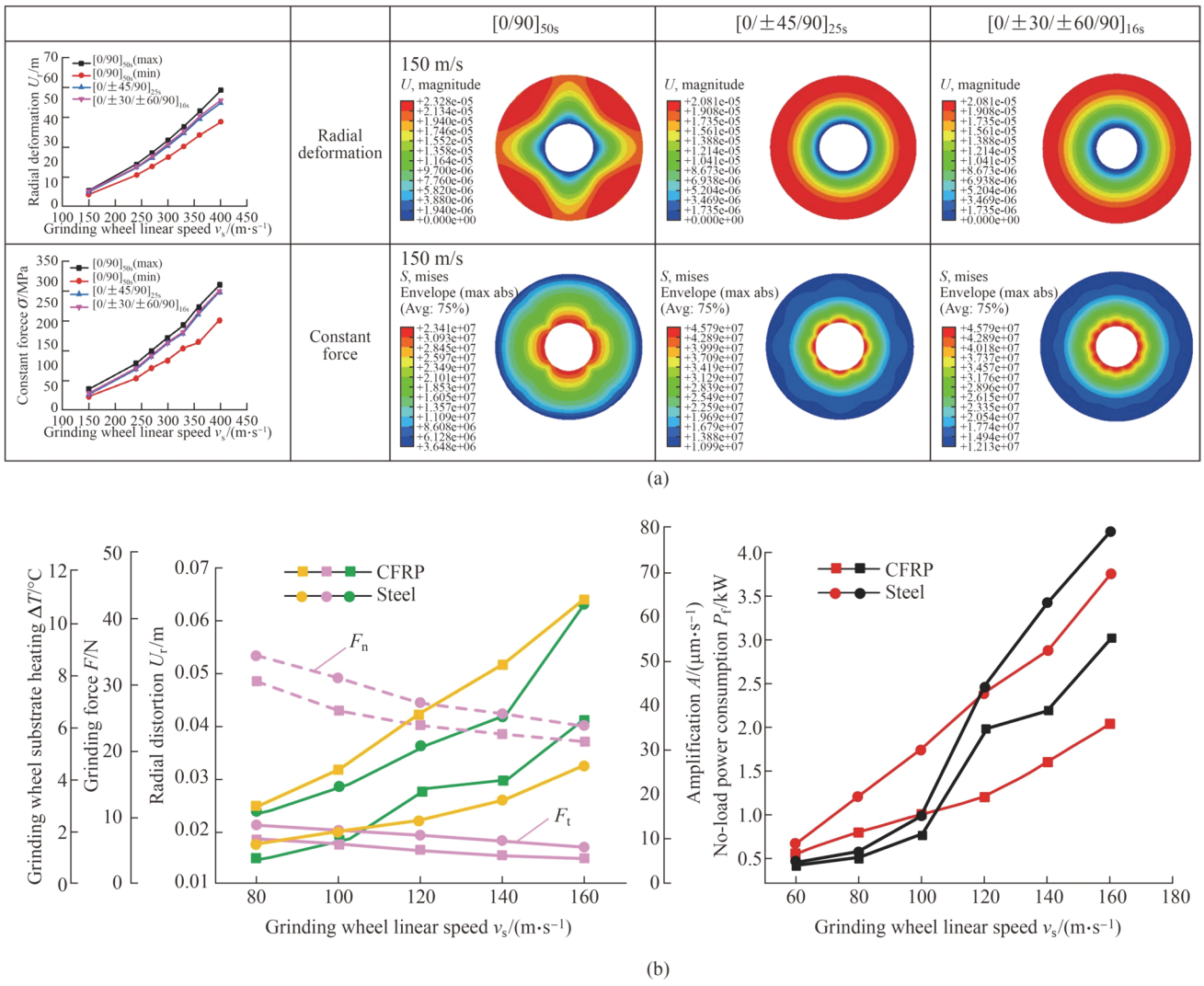

Fig. 40 Results of radial deformation and equivalence of CFRP grinding wheel under different layering methods and different grinding experimental parameters **a** variation of radial deformation and equivalent stress of CFRP wheel substrate with speed and deformation distribution of CFRP wheel substrate with different layups at v_s=150 m/s, **b** influence of CFRP and steel grinding wheels on no-load power consumption, radial deformation, temperature rise of the wheel, amplitude and grinding force as the v_s increases [198]

parameters. It is best to establish a complete database through a large number of studies on HSG of different workpiece materials under different lubrication methods, so as to provide research ideas for young scholars and facilitate future scientific research.

(iv) According to the content summarized in this review, it is found that the stiffness and strength of the main structure of the grinder is still not high enough, and better materials can be explored through research to make the main weight of the grinder 50% lighter than the traditional grinder, and improve the dynamic balance of the spindle. For the spindle part of the grinding machine, the test platform can be optimized by reducing the weight and step angle, and the dynamic balance test speed can be increased to solve the dynamic balance problem of high-speed grinding. From the current point of view, after long-term development, the manufacturing and application technology of ordinary grinding wheel has been very mature, but the preparation method of HSG wheel is relatively simple and the price is relatively expensive, and the current HSG wheel has the risk of grinding wheel explosion, and the adhesive at the interface between the grinding wheel matrix and the abrasive layer is unstable, uneven and aging. Once the adhesive fails, the stress of the abrasive layer will increase

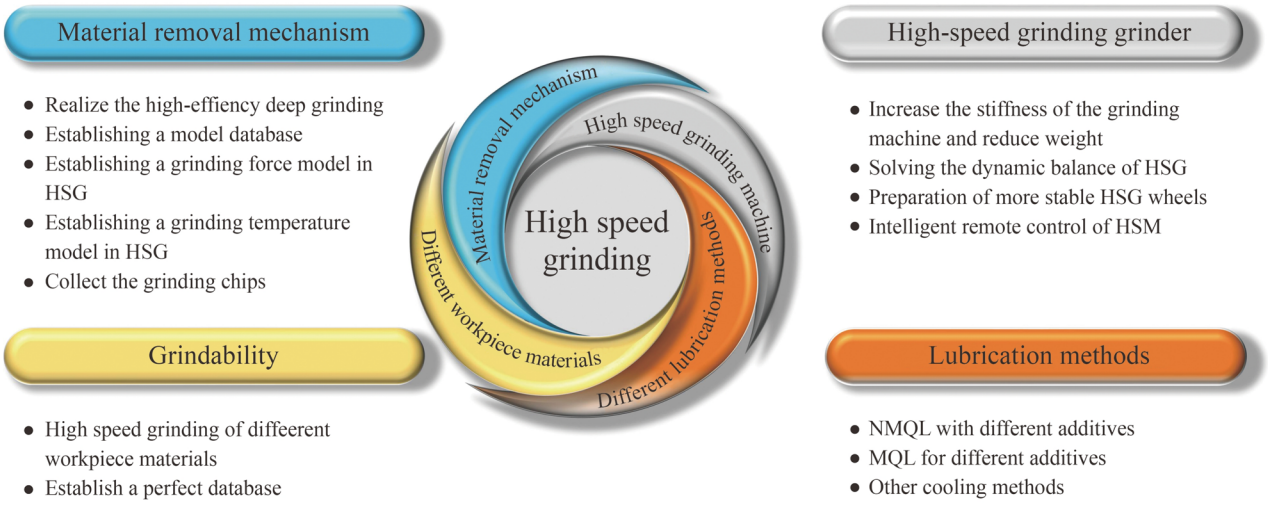

Fig. 41 Outlook of HSG

dramatically, and the risk of wheel explosion will also increase, which is an urgent problem that needs to be solved. At present, with the development of intelligent grinding, improving the correction accuracy and automation of the grinding wheel is the current development direction, and the future needs scholars to study and explore the intelligent control and remote control of the grinding machine to achieve the safe operation of the grinder and ensure the safety of the operator.

Acknowledgements This research was financially supported by the Special Fund of Taishan Scholars Project (Grant No.tsqn202211179), the National Natural Science Foundation of China (Grant No. 52105457), the Youth Talent Promotion Project in Shandong (Grant No. SDAST2021qt12), the National Natural Science Foundation of China (Grant No. 52375447)

Data availability Data is not available due to consent restrictions. [The study participants have not given written permission to share their data publicly.

References

1. Gong P, Zhang YB, Li CH et al (2023) Residual stress generation in grinding: mechanism and modeling. J Mater Process Tech 324:118262. https://doi.org/10.1016/j.jmatprotec.2023.118262
2. Cui X, Li CH, Yang M et al (2023) Enhanced grindability and mechanism in the magnetic traction nanolubricant grinding of Ti-6Al-4V. Tribol Int 186:108603. https://doi.org/10.1016/j.triboint.2023.108603
3. Liu MZ, Li CH, Yang M et al (2023) Mechanism and enhanced grindability of cryogenic air combined with biolubricant grinding titanium alloy. Tribol Int 187:108704. https://doi.org/10.1016/j.triboint.2023.108704
4. Cui X, Li CH, Zhang YB et al (2022) Grindability of titanium alloy using cryogenic nanolubricant minimum quantity lubrication. J Manuf Process 80:273–286
5. Yang M, Kong M, Li CH et al (2023) Temperature field model in surface grinding: a comparative assessment. Int J Extreme Manuf 5(4):042011. https://doi.org/10.1088/2631-7990/ACF4D4
6. Wang H, Huang LJ, Yao C et al (2015) Integrated analysis method of thin-walled turbine blade precise machining. Int J Precis Eng Manuf 16:1011–1019
7. Zhao GL, Zhao B, Ding WF et al (2024) Nontraditional energy-assisted mechanical machining of difficult-to-cut materials and components in aerospace community: a comparative analysis. Int J Extrem Manuf 6(2):022007. https://doi.org/10.1088/2631-7990/ad16d6
8. Wang BX, Zhao YJ, Liu GY et al (2023) Preventing thermal osteonecrosis through 3D printed ceramic grinding tool. Addit Manuf 78:103878. https://doi.org/10.1016/j.addma.2023.103878
9. Huang WH, Yan JW (2023) Effect of tool geometry on ultra-precision machining of soft-brittle materials: a comprehensive review. Int J Extrem Manuf 5(1):012003. https://doi.org/10.1088/2631-7990/acab3f
10. Liang XL, Liu CQ, Wang B et al (2023) Friction behaviors in the metal cutting process: state of the art and future perspectives. Int J Extrem Manuf 5(1):012002. https://doi.org/10.1088/2631-7990/ac9e27
11. Song YX, Li CH, Zhou ZM et al (2024) Nanobiolubricant grinding: a comprehensive review. Adv Manuf 12(1) 1–42

12. Choi YJ, Park KH, Hong YH et al (2013) Effect of ultrasonic vibration in grinding; horn design and experiment. Int J Precis Eng Manuf 14(11):1873–1879
13. Sun C, Xiu SC, Hong Y et al (2020) Prediction on residual stress with mechanical-thermal and transformation coupled in DGH. Int J Mech Sci 179:105629. https://doi.org/10.1016/j.ijmecsci.2020.105629
14. Yang L, Chu CH, Fu YC et al (2015) CFRP grinding wheels for high speed and ultra-high speed grinding: a review of current technologies and research strategies. Int J Precis Eng Manuf 16(12):2599–2606
15. Li BZ, Ni JM, Yang JG et al (2014) Study on high-speed grinding mechanisms for quality and process efficiency. Int J Adv Manuf Tech 70:813–819
16. Zhu Y (2021) Exploration of the application of ultra-high speed grinding technology in machinery manufacturing. Intern Combus Eng Parts 3:109–110
17. Yuan JL, Deng ZH, Xiong WL et al (2010) Development and prospect of high-efficiency grinding technology and equipment. Aeronaut Manuf Tech 5:66–70
18. Akilu S, Sharma KV, Baheta AT et al (2016) A review of thermophysical properties of water based composite nanofluids. Renew Sust Energ Rev 66:654–678
19. Li C, Hu YX, Wei ZZ et al (2024) Damage evolution and removal behaviors of GaN crystals involved in double-grits grinding. Int J Extrem Manuf 6(2):025103. https://doi.org/10.1088/2631-7990/ad207f
20. Zhao JS, Zhao B, Ding WF et al (2023) Grinding characteristics of MoS_2-coated brazed CBN grinding wheels in dry grinding of titanium alloy. Chin J Mech Eng-En 36(1):109. https://doi.org/10.1186/s10033-023-00936-z
21. Qian N, Chen JJ, Khan AM et al (2024) Towards sustainable grinding of difficult-to-cut alloys–a little longer a holistic review and trends. Chin J Mech Eng-En 37(1):23. https://doi.org/10.1186/s10033-024-01002-y
22. Zhao HH, Gao XJ, Cai GQ (2006) Experimental study of impact chip formation mechanism in ultra-high speed grinding. China Mech Eng 42(9):43–47
23. Zhao HH, Cai GQ, Gao XJ (2006) Research on grinding mechanism of natural marble by ultra-high speed impact grinding. China Mech Eng 7:677–680
24. Zhao HH, Cai GQ (2004) Construction of impact chip formation model and mechanism research of ultra-high speed grinding. China Mech Eng 12:6–9
25. Zhao HH, Gao XJ, Cai GQ (2006) Experimental study on chip formation mechanism due to shock of ultra-high speed grinding. China Mech Eng 42(9):43–47
26. Zhang QL, To S, Zhao QL et al (2016) Surface generation mechanism of WC/Co and RB-SiC/Si composites under high spindle speed grinding (HSSG). Int J Refract Met H 56:123–131
27. Yin JF, Xu JH, Ding WF et al (2021) Effects of grinding speed on the material removal mechanism in single grain grinding of SiCf/SiC ceramic matrix composite. Ceram Int 47(9):12795–12802
28. Cheng Z, Xu JH, Ding WF (2011) Simulation study on chip formation process of titanium alloy TC4 grinding with single abrasive particle. Diamond Abrasives Eng 31(2):17–21
29. Wang ML (2015) Study on material removel mechanism of ultra-high-speed grrinding. Dissertation, Taiyuan Universityof Technology
30. Li DH (2013) Research on chip-formation mechanism of high-speed grinding for material of difficult machining. Dissertation, Donghua University
31. Zhou H, Ding WF, Liu CJ (2019) Material removal mechanism of PTMCs in high-speed grinding when considering consecutive action of two abrasive grains. Int J Adv Manuf Tech 100(1/4):153–165
32. Chen GP (2018) Study on dynamic characteristics and structure optimization of the high speed grinder. Dissertation, Hunan University
33. Yeo SH, Ramesh K, Zhong ZW (2002) Ultra-high-speed grinding spindle characteristics upon using oil/air mist lubrication. Int J Mach Tool Manu 42(7):815–823
34. Sun XY, Yao ZQ (2019) Research on thermal characteristics of high-speed grinding spindles and their influencing factors. Mod Mach Tool Autom Manuf Tech 11:17–21
35. Liu Y, Ma YX, Meng QY et al (2018) Improved thermal resistance network model of motorized spindle system considering temperature variation of cooling system. Adv Manuf 6(4):384–400
36. Liang JW (2021) Study and development of online dynamic balancing system for high speed grinder. Dissertation, Henan University of Technology
37. Guo S, Zhang JQ, Jiang QH et al (2022) Surface integrity in high-speed grinding of Al6061T6 alloy. CIRP ANN-Manuf Techn 71(1):281–284
38. Qiao GW, Zhang B, Guo S et al (2023) Surface morphology in high-speed grinding of TMCs fabricated by selective laser melting. J Manuf Process 97:200–209
39. Yang L (2017) Fundamental research on the ultra-high speed grinding of nickel-based superalloy with CFRP wheels. Dissertation, Nanjing University of Aeronautics and Astronautics
40. Lin T, Fu YC, Xu JH et al (2015) The influence of speed on material removal mechanism in high speed grinding with single grit. Int J Mach Tool Manu 89:192–201
41. Zhan YJ (2013) Mechanisms research on high speed grinding of cemented carbide with vitrified diamond wheels. Dissertation, Huaqiao University
42. Xiao P (2009) Study on surface integrity of titanium alloy TC4 in ultra high speed grinding process. Dissertation, Hunan University
43. Yin L, Huang H, Ramesh K et al (2005) High speed versus conventional grinding in high removal rate machining of alumina and alumina-titania. Int J Mach Tool Manu 45(7):897–907
44. Dai LZ, Chen GY, Shan ZZ (2021) Study on ultra-high speed nano-grinding of monocrystalline copper with V-shaped diamond abrasive grains based on molecular dynamics method. Diam Relat Mater 111:108224. https://doi.org/10.1016/j.diamond.2020.108224
45. Li P, Chen SY, Jin T et al (2021) Machining behaviors of glass-ceramics in multi-step high-speed grinding: grinding parameter effects and optimization. Ceram Int 47(4):4659–4673
46. Li Z, Ding WF, Shen L et al (2016) Comparative investigation on high-speed grinding of TiCp/Ti-6Al-4V particulate reinforced titanium matrix composites with single-layer electroplated and brazed CBN wheels. Chin J Aeronaut 29(5):1414–1424
47. Zhang Z (2017) The investigations of high speed grinding mechanisms on AISI 1045 steel components with narrow deep groove structure. Dissertation, Taiyuan University of Technology
48. Ren J, Hao MR, Lv M et al (2018) Molecular dynamics research on ultra-high-speed grinding mechanism of monocrystalline nickel. Appl Surf Sci 455:629–634
49. Ma ZF (2019) Numerical and experimental analysis on high speed grinding Ti6Al4V with single grit. Dissertation, Taiyuan University of Technology
50. Xu H (2012) Grinding temperature simulation research in high speed grinding of cemented carbides using finite element method. Dissertation, Hunan University
51. Lu SX, Yang XX, Zhang JQ et al (2022) Rational thinking on removal mechanisms and processing damage of hard and brittle materials. Chin J Mech Eng-En 58(15):31–45
52. Wang B, Liu ZQ, Su GS et al (2015) Brittle removal mechanism of ductile materials with ultrahigh-speed machining. J

Manuf Sci Eng 137(6):061002. https://doi.org/10.1115/1.4030826
53. Yang X, Zhang B (2019) Material embrittlement in high strain-rate loading. Int J Extrem Manuf 1(2):022003. https://doi.org/10.1088/2631-7990/ab263f
54. Chen ZZ, Xu JH, Ding WF et al (2014) Grinding performance evaluation of porous composite-bonded CBN wheels for Inconel 718. Chin J Aeronaut 27(4):1022–1029
55. Zhang YB (2018) Grinding mechanism, force prediction model and experimental validation of vegetable oil based nanofluids minimum quantity lubrication. Dissertation, Qingdao University of Technology
56. Mao C, Wang JL, Zhang MJ et al (2023) Prediction of grinding force by an electroplated grinding wheel with orderly-micro-grooves. Chin J Mech Eng-En 36(1):116. https://doi.org/10.1186/s10033-023-00937-y
57. Jin T, Cai GQ (1999) Strain rate strengthening of materials and size effects in grinding. Chin Mech Eng 10(12):1401–1403
58. Jin T, Stephenson DJ (2006) Heat flux distributions and convective heat transfer in deep grinding. Inter J Mach Tool Manu 46(14)1862–1868
59. Umbrello D, Micari F, Jawahir IS (2012) The effects of cryogenic cooling on surface integrity in hard machining: a comparison with dry machining. CIRP Ann-Manuf Techn 61(1):103–106
60. Zhang B, Yin JF (2019) The "skin effect" of subsurface damage distribution in materials subjected to high-speed machining. Int J Extrem Manuf 1(1):012007. https://doi.org/10.1088/2631-7990/ab103b
61. Wu ZW, Fan WA, Qian C et al (2023) Contact mechanism of rail grinding with open-structured abrasive belt based on pressure grinding plate. Chin J Mech Eng-En 36(1):42. https://doi.org/10.1186/s10033-023-00862-0
62. Liu XB, Zhang B, Deng ZH (2002) Grinding of nanostructured ceramic coatings: surface observations and material removal mechanisms. Int J Mach Tool Manu 42(15):1665–1676
63. Wang B, Liu ZQ, Song QH et al (2016) Proper selection of cutting parameters and cutting tool angle to lower the specific cutting energy during high speed machining of 7050–T7451 aluminum alloy. J Clean Prod 129:292–304
64. Ma W, Chen X, Shuang F (2017) The chip-flow behaviors and formation mechanisms in the orthogonal cutting process of Ti6Al4V alloy. J Mech Phys Solids 98:245–270
65. Zhang YQ, Lu Y, Hao H (2004) Analysis of fragment size and ejection velocity at high strain rate. Int J Mech Sci 46(1):27–34
66. Dai JB, Ding WF, Zhang LC et al (2015) Understanding the effects of grinding speed and undeformed chip thickness on the chip formation in high-speed grinding. Int J Adv Manuf Tech 81:995–1005
67. Li LY, Zhang YB, Cui X et al (2023) Mechanical behavior and modeling of grinding force: a comparative analysis. J Manuf Process 102:921–954
68. Xia J (2020) Experimental and simulation research on ultra-high speed grinding of nickel-based superalloys based on single abrasive grain. Dissertation, Nanjing University of Aeronautics and Astronautics
69. Fan ZL (2018) Simulation and experimental study on grinding mechanism of high-speed grinding AISI 1045 steel with single abrasive grain. Dissertation, Taiyuan University of Technology
70. Liu CJ (2018) Removal mechanism of particulate reinforced titanium matrix composites in high-speed grinding. Dissertation, Nanjing University of Aeronautics and Astronautics
71. Fu DK, Ding WF, Yang SB et al (2017) Formation mechanism and geometry characteristics of exit-direction burrs generated in surface grinding of Ti-6Al-4V titanium alloy. Int J Adv Manuf Tech 89:2299–2313
72. Yu J, Liu Z, Wu Y et al (2015) Simulation study of high-speed grinding of alloy steel 20CrMo with single grits. Manuf Tech Mach Tool 12:97–102
73. Cheng Z, Xu J, Ding W et al (2011) Simulation study of chip formation process in single grit grinding of titanium alloy TC4. Diamond Abrasives Eng 31(2):17–21
74. Holmquist TJ, Johnson GR (2011) A computational constitutive model for glass subjected to large strains, high strain rates and high pressures. J Appl Mech-t ASME 78(5):051003. https://doi.org/10.1115/1.4004326
75. Johnson GR, Holmquist TJ (1994) An improved computational constitutive model for brittle materials. Am Inst Phys Conf Proc 309(1):981–984
76. Wang B, Liu ZQ, Cai YK et al (2021) Advancements in material removal mechanism and surface integrity of high speed metal cutting: a review. Int J Mach Tool Manu 166:103744. https://doi.org/10.1016/j.ijmachtools.2021.103744
77. Andrade U, Meyers M, Vecchio K et al (1994) Dynamic recrystallization in high-strain, high-strain-rate plastic deformation of copper. Acta Mater 42(9):3183–3195
78. Fu XL, Ai X, Zhang S et al (2006) Constitutive equation for 7050 aluminum alloy at high temperatures. Mater Sci Forum 532/533:125–128
79. Calamaz M, Coupard D, Girot F (2008) A new material model for 2D numerical simulation of serrated chip formation when machining titanium alloy Ti-6Al-4V. Int J Mach Tool Manu 48(3/4):275–288
80. Sheikh-Ahmad JY, Bailey JA (1995) A constitutive model for commercially pure titanium. J Eng Mater Technol 117(2):139–144
81. Li GH, Wang MJ, Duan CZ (2009) Adiabatic shear critical condition in the high-speed cutting. J Mater Process Tech 209(3):1362–1367
82. Wang XY, Huang CZ, Zou B et al (2013) Dynamic behavior and a modified Johnson-Cook constitutive model of Inconel 718 at high strain rate and elevated temperature. Mater Sci Eng A 580:385–390
83. Ugodilinwa NE, Khoshdarregi M, Ojo OA (2019) Analysis and constitutive modeling of high strain rate deformation behavior of Haynes 282 aerospace superalloy. Mater Today Commun 20:100545. https://doi.org/10.1016/j.mtcomm.2019.100545
84. Wang B, Liu ZQ, Song QH et al (2019) A modified Johnson-Cook constitutive model and its application to high speed machining of 7050–T7451 aluminum alloy. J Manuf Sci Eng 141(1):011012. https://doi.org/10.1115/1.4041915
85. Liu CJ, Ding WF, Yu TY et al (2018) Materials removal mechanism in high-speed grinding of particulate reinforced titanium matrix composites. Precis Eng 51:68–77
86. Wu SX, Gong X, Ni YQ et al (2022) Material removal and surface damage in high-speed grinding of enamel. J Mech Behav Biomed 136:105532. https://doi.org/10.1016/j.jmbbm.2022.105532
87. Setti D, Sinha MK, Ghosh S et al (2015) Performance evaluation of Ti-6Al-4V grinding using chip formation and coefficient of friction under the influence of nanofluids. Int J Mach Tool Manu 88:237–248
88. Doyle ED, Dean SK (1980) An insight into grinding from a materials viewpoint. CIRP Ann-Manuf Techn 29(2):571–575
89. Doyle ED, Aghan RL (1975) Mechanism of metal removal in the polishing and fine grinding of hard metals. Metall Mater Trans B 6:143–147
90. Xia J, Ding WF, Qiu B et al (2020) 3D simulation study on the chip formation process of nickel-based high-temperature alloy high-speed ultra-high-speed grinding. Diamond Abrasives Eng 40(6):58–69
91. Sun JG, Li C, Zhou ZM et al (2023) Material removal mechanism and force modeling in ultrasonic vibration-assisted

micro-grinding biological bone. Chin J Mech Eng-En 36(1):129. https://doi.org/10.1186/s10033-023-00957-8
92. Liu XC, Chen F, Zhao C et al (2016) Simulation and research of single abrasive cutting based on DEFORM-3D. Mach Des Manuf 10:69–73
93. Yao CF, Wang T, Xiao W et al (2014) Experimental study on grinding force and grinding temperature of Aermet 100 steel in surface grinding. J Mater Process Tech 214(11):2191–2199
94. Sun S, Brandt M, Dargusch MS (2009) Characteristics of cutting forces and chip formation in machining of titanium alloys. Int J Mach Tool Manu 49(7/8):561–568
95. Liu YF, Wang D, Chen X (2016) Experimental study of grinding force and specific grinding energy for high-speed grinding of 18CrNiMo7-6. Manuf Tech Mach Tool 8:94–97
96. Patidar A, Kumar MA, Kumar Chaudhary A (2021) High speed super abrasive grinding of sintered yttria stabilised zirconia (YSZ) using single layer electroplated diamond grinding wheels. Mater Today Proc 45:4660–4665
97. Wang XM, Song YX, Li CH et al (2023) Nanofluids application in machining: a comprehensive review. Int J Adv Manuf Tech 1–52
98. Sun C, Hong Y, Xiu SC et al (2023) Surface strengthening mechanism of the active grinding carburization. Tribol Int 185:108569. https://doi.org/10.1016/j.triboint.2023.108569
99. Rowe WB (2001) Thermal analysis of high efficiency deep grinding. Int J Mach Tool Manu 41(1):1–19
100. Guo ZF (2012) Experimental investigations and FEM simulation of temperature field in ultra-high speed grinding of 9SiCr. Dissertation, Hunan University
101. Makino H, Suto T, Fukushima E (1966) An experimental investigation of the grinding process. Gov Mech Lab J 20(1):11–23
102. Tönshoff HK, Wobker HG, Brunner G (1995) CBN grinding with small wheels. CIRP Ann-Manuf Techn 44(1):311–316
103. Guo C, Malkin S (1996) Effectiveness of cooling in grinding. Trans Namri Sme 111–118
104. Ichida Y, Sato R, Morimoto Y et al (2006) Formation mechanism of finished surface in ultrahigh-speed grinding with cubic boron nitride (cBN) wheels. JSME Int J C-Mech Sy 49(1):100–105
105. Chen X, Wang D, Liu YF (2016) Effect of high speed grinding of 18CrNiMo7-6 gear steel on residual stresses. Mach Des Manuf 9:80–82
106. Xiao ZQ (2016) Experimental research on high-speed cylindrical grinding of GCr15 steel. Dissertation, Hunan University of Science and Technology
107. Jiang F, Liao WM (2017) High-speed grinding and morphological characterisation of K4169 alloy. Foundry Tech 38(8):1822–1825
108. Huang YC (2016) Experimental study on high speed cylindrical grinding of TC4 titanium alloy. Dissertation, Hunan University of Science and Technology
109. Xu J, Lu WZ, Wang H et al (2013) Ceramic bond CBN grinding wheel for high speed grinding of titanium alloy TC4-DT. Diamond Abrasives Eng 33(5):12–16
110. Shih A, Mcspadden S, Morris T et al (2000) High speed and high material removal rate grinding of ceramics using the vitreous bond CBN wheel. Mach Sci Technol 4(1):43–58
111. Wu P (2012) The experimental study on high speed grinding technology in HT300 and QT600-3. Dissertation, Hunan University
112. Yin L, Huang H (2004) Ceramic response to high speed grinding. Mach Sci Technol 8(1):21–37
113. Dai JB (2019) Research on grinding damage formation mechanisms and influence mechanism of polycrystalline silicon carbide ceramics based on fracture mechanics. Dissertation, Nanjing University of Aeronautics and Astronautics
114. Guo S, Lu SX, Zhang B et al (2022) Surface integrity and material removal mechanisms in high-speed grinding of Al/SiCp metal matrix composites. Int J Mach Tool Manu 178:103906. https://doi.org/10.1016/j.ijmachtools.2022.103906
115. Guo S, Cheung C, Ho L et al (2023) Microstructural evolution in ultra-precision grinding of Al/SiCp metal matrix composites. Precis Eng 83:12–21
116. Rastegari HA, Asgari S, Abbasi SM (2011) Producing Ti-6Al-4V/TiC composite with good ductility by vacuum induction melting furnace and hot rolling process. Mater Des 32(10):5010–5014
117. Huang LJ, Geng L, Peng HX (2010) In situ (TiBw+TiCp)/Ti6Al4V composites with a network reinforcement distribution. Mat Sci Eng A-Struct 527(24/25):6723–6727
118. Feng CB, Xie GZ, Sheng XM et al (2013) Experimental study on ultra-high speed grinding of stainless steel. Chin J Mech Eng 24(3):322–326
119. Zhang Y, Yang X, Yuan S et al (2021) Residual stresses in high-speed cylindrical grinding of 18CrNiMo7-6 steel. Chin J Mech Eng 32(5):540–546
120. Chen X, Wang D, Liu Y (2017) Effect of high speed grinding of 18CrNiMo7-6 gear steel on residual stresses. Mach Des Manuf 9:80–82
121. Cheng Q, Liang GX, Hao JY et al (2020) Wear study of single PCBN grits for high-speed grinding of Inconel 718. J Mech Electr Eng 37(10):1225–1230
122. Qian Y, Xu J, Fu Y et al (2011) Study on grinding force and specific grinding energy of nickel-based high temperature alloy by cBN grinding wheel at high speeds. Diamond Abrasives Eng 31(6):33–37
123. Dai C, Ding W, Zhu Y et al (2018) Grinding temperature and power consumption in high speed grinding of Inconel 718 nickel-based superalloy with a vitrified CBN wheel. Precis Eng 52:192–200
124. Xiao LX (2017). Experimental study of surface quality in high speed cylindrical grinding of titanium alloy. Dissertation, Hunan University of Science and Technology
125. Tian L, Fu YC, Yang L et al (2014) Experimental study of high-speed grinding of titanium alloy Ti6Al4V. Chin J Mech Eng 25(22):3056–3060
126. Cheng M, Yu JW, Xie GZ et al (2011) Experimental study on high-speed grinding process of cemented carbide YG8. Manuf Tech Mach Tool 1:25–29
127. Li S (2015) Experimental study on high-speed grinding of YG6 cemented carbide. Pract Electr 8:45. https://doi.org/10.16589/j.cnki.cn11-3571/tn.2015.08.019
128. Cheng M (2011) The research on super high-speed grinding technology in YG8 and PA30 cemented carbide. Dissertation, Hunan University
129. Li Z, Ding WF, Zhou H et al (2019) High-speed grinding temperature study of particle-reinforced titanium-based composites based on a hybrid material model. J Mech Eng 55(21):186–198
130. Chen XC, Qi W, Wang C et al (2016) Study on the prediction of high-speed grinding force of WC-10Co4Cr coating. Intell Manuf 10:31–36
131. Choudhary A, Paul S (2021) Surface generation in high-speed grinding of brittle and tough ceramics. Ceram Int 47(21):30546–30562
132. Wu CJ, Li BZ, Pang JZ et al (2016) Ductile grinding of Silicon carbide in high-speed grinding. J Adv Mech Des Syst 10(2):Jamdsm0020. https://doi.org/10.1299/jamdsm.2016jamdsm0020
133. Choudhary A, Naskar A, Paul S (2018) Effect of minimum quantity lubrication on surface integrity in high-speed grinding of sintered alumina using single layer diamond grinding wheel. Ceram Int 44(14):17013–17021

134. Boswell B, Islam MN, Davies IJ et al (2017) A review identifying the effectiveness of minimum quantity lubrication (MQL) during conventional machining. Int J Adv Manuf Tech 92(1/4):321–340
135. Tawakoli T, Hadad MJ, Sadeghi MH (2010) Investigation on minimum quantity lubricant-MQL grinding of 100Cr6 hardened steel using different abrasive and coolant-lubricant types. Int J Mach Tool Manu 50(8):698–708
136. Emami M, Sadeghi MH, Sarhan AAD (2013) Investigating the effects of liquid atomization and delivery parameters of minimum quantity lubrication on the grinding process of Al_2O_3 engineering ceramics. J Manuf Process 15(3):374–388
137. Li X (2014) Application of self-inhaling internal cooling wheel in vertical surface grinding. Chin J Mech Eng 27(1):86–91
138. Miao Q, Ding WF, Xu JH et al (2021) Creep feed grinding induced gradient microstructures in the superficial layer of turbine blade root of single crystal nickel-based superalloy. Int J Extreme Manuf 3(4):045102. https://doi.org/10.1088/2631-7990/AC1E05
139. Choudhary A, Naskar A, Paul S (2018) An investigation on application of nano-fluids in high-speed grinding of sintered alumina. J Manuf Process 35:624–633
140. Zhang YB, Li CH, Yang M et al (2016) Experimental evaluation of cooling performance by friction coefficient and specific friction energy in nanofluid minimum quantity lubrication grinding with different types of vegetable oil. J Clean Prod 139:685–705
141. Xu WH, Li CH, Zhang YB et al (2022) Electrostatic atomization minimum quantity lubrication machining: from mechanism to application. Int J Extreme Manuf 4(4):042003. https://doi.org/10.1088/2631-7990/ac9652
142. Li Q, Xuan YM (2006) Enhanced heat transfer behaviors of new heat carrier for spacecraft thermal management. J Spacecraft Rockets 43(3):687–690
143. Wang P (2014) A research on steel rail material processed by high-speed grinding with cryogenic gas-liquid two-phase supplying technique. Dissertation, Hunan University
144. Jun S, Hiroshi E (2002) Simulation and experimental analysis of super high-speed grinding of ductile material. J Mater Process Tech 129(1):19–24
145. Chang Z, Jia Q, Hu L (2023) Design and development of a high-speed precision internal grinding machine and the associated grinding processes. Processes 11(1):64. https://doi.org/10.3390/PR11010064
146. Li CS, Sun L, Chen ZX et al (2022) Wheel setting error modeling and compensation for arc envelope grinding of large-aperture aspherical optics. Chin J Mech Eng-En 35(1):108. https://doi.org/10.1186/s10033-022-00782-5
147. Yang L, Fu YC, Xu JH (2015) Development of a novel supersonic grinding machine tool. Int J Adv Manuf Tech 81:2039–2052
148. Guo MX, Li BZ (2016) A frequency-domain grinding force model-based approach to evaluate the dynamic performance of high-speed grinding machine tools. Mach Sci Technol 20(1):115–131
149. Zhang BL, Yang QD, Chen CN (2003) High-speed cutting technology and application. Mech Electr Eng Tech 4:85–86
150. Zheng TY (2022) Dynamic analysis and optimization design ofof machine tools. Dissertation, Southeast University
151. Xu HW, Zhang GP, Huang YM et al (2011) Study on influence of marble machine bed on temperature field distribution of headstock. China Mech Eng 22(11):1274–1278
152. Song Z, Shang Y, Zhao J (2008) Application of artificial marble bed in general CNC grinding machine. Precis Manuf Autom 2:27–36
153. Xu HW, Zhang GP, Huang YM et al (2011) Study on the effect of marble machine bed on the temperature field distribution of spindle box. China Mech Eng 22(11):1274–1278
154. Yuan L (2008) Introduction to the processing of artificial marble beds. Metal Working 9:39–40
155. Yuan QK, Chen JJ, Du YN et al (2012) ANSYS-based finite element analysis of the marble bed of a grinding machine. Manuf Autom 34(3):99–101
156. Mei JW (2021) Analysis of vibration characteristics of ultra-high speed grinding electric spindle under the action of magneto-thermal. Dissertation, Henan University of Technology
157. Zhang XL (2019) New type of high-speed electric spindle bearing-core thermal field distribution law and experimental research. Dissertation, Harbin University of Science and Technology
158. Yin H (2015) Permanent magnet synchronous motor loss calculation and temperature field analysis. Dissertation, Harbin University of Science and Technology
159. Zhang B (2010) Analysis of thermal characteristic & optimization design on direct-drive lathe. Dissertation, Chongqing University
160. Emad D (2008) A simplified iron loss model for laminated magnetic cores. IEEE T Magn 44(11):3169–3172
161. Liu RF, Ma X, Cao JC et al (2020) The performance comparison between amorphous and silicon steel in the stator core of permanent magnet synchronous motor. Electr Mach Control 24(1):61–68
162. Guo J (2005) Research on thermal characteristics of electric spindle based on thermal contact analysis. Dissertation, Guangdong University of Technology
163. Cui XK (2018) Research on temperature distribution and thermal displacement of high speed spindle. Dissertation, Shenyang Jianzhu University
164. Bertotti G (1988) General properties of power losses in soft ferromagnetic materials. IEEE T Magn 24(1):621–630
165. Wang XY, Li J, Qi LX et al (2007) Calculation of eddy current loss density in permanent magnet rotor permanent magnets of permanent magnet synchronous motors. J Shenyang Univ Technol 1:48–51
166. Huang ZH, Li CH, Zhou ZM et al (2024) Magnetic bearing: structure, model, and control strategy. Int J Adv Manuf Tech 131:3287–3333
167. Tang SM, Mei L, Ouyang HM (2013) Application status of magnetic levitation bearing technology in fan and pump equipment. Small Spec Electr Mach 41(8):68–70
168. Zhang CB, Ao HR, Jiang HY (2021) Static and dynamic bearing performances of hybrid gas dynamic bearings. Tribol Int 160:107036. https://doi.org/10.1016/j.triboint.2021.107036
169. Yun XL, Mei XS, Jiang GD et al (2019) Analysis and test method of dynamic stiffness of high-speed spindle angular contact ball bearings. J Vib Meas Diag 39(4):892–897
170. Xie ZY, Yu K, Wen LT et al (2014) Characteristics of motorized spindle supported by active magnetic bearings. Chin J Aeronaut 27(6):1619–1624
171. Xia ZX, Wu YH, Ma TB et al (2022) Experimental study on adaptability of full ceramic ball bearings under extreme conditions of cryogenics and heavy loads. Tribol Int 175:107849. https://doi.org/10.1016/j.triboint.2022.107849
172. Ma SJ, He GB, Yan K et al (2022) Structural optimization of ball bearings with three-point contact at high-speed. Int J Mech Sci 229:107494. https://doi.org/10.1016/j.ijmecsci.2022.107494
173. Rong LR (2003) Current status and development prospects of high-speed grinding technology. Mechatronics 1:6–10
174. Yin MQ, Jing MQ, Liu H et al (2011) Hardware design of on-line dynamic balancing system for high-speed grinding. Manuf Tech Mach Tool 6:156–159
175. Liu J, Pan SX, Yang KJ et al (2006) Key technology research on fully automatic dynamic balancing machine. J Zhejiang Univ Eng Sci 5:777–782

176. Zhang LL, Duan ZH, Li DM et al (2012) Research progress of on-site dynamic balancing technology. Chem Eng Mach 39(6):690–694
177. Zhou DS, Wu LS (2008) Overview of on-line dynamic balancing technology for machine tool spindles. Mod Manuf Eng 7:121–124
178. Xia SB, Liu YG, Li Y et al (1999) Overview of automatic dynamic balancing of rotating machinery. China Mech Eng 458–460
179. Zhu GX, Tan Q, Jiang B (2019) Stability study of ball-type automatic balancing device based on bifurcation theory. Noise Vib Control 39(6):36–43
180. Fan HW, Jing MQ, Liu H (2012) A review of research on automatic balancing device for active hybrid grinding wheel-spindle system. J Vib Shock 31(5):26–30
181. Wu Y, Lu P, Lin FH et al (2021) Explosion accident analysis of ultra-high-speed grinding wheel. Eng Fail Anal 122:105209. https://doi.org/10.1016/j.engfailanal.2020.105209
182. Li CH (2024) Thermodynamic mechanism of MQL grinding with nano bio-lubricant. Springer Nature. https://doi.org/10.1007/978-981-99-6265-5.2
183. Deng ZH, Wu QP, Zhang GF et al (2010) New grinding wheel research progress and its outlook. China Mech Eng 21(21):2632–2638
184. Hei HZ (2011) Experimental research on high speed grinding titanium alloy with CBN wheels. Dissertation, Nanjing University of Aeronautics and Astronautics
185. Wu QP, Ouyang ZY, Wang Y et al (2019) Precision grinding of engineering ceramic based on the electrolytic dressing of a multi-layer brazed diamond wheel. Diam Relat Mater 100:107552. https://doi.org/10.1016/j.diamond.2019.107552
186. Xuan C, Wang CC, Bai FH et al (2022) Ceramic bond diamond grinding wheels based on hollow alumina microspheres for pore creation. Diamond Abrasives Eng 42(4):442–448
187. Sun YK (2022) Experimental research on laser dressing of V-shaped resin-bonded diamond grinding wheel. Dissertation, Hunan University of Science and Technology
188. Ghosh A, Chattopadhyay AK (2007) On grit-failure of an indigenously developed single layer brazed CBN wheel. Ind Do Rev 67(1):59–64
189. Ding WF, Xu JH, Shen M et al (2007) Development and performance of monolayer brazed CBN grinding tools. Int J Adv Manuf Tech 34(5):491–495
190. Ding WF, Xu JH, Chen ZZ et al (2010) Wear behavior and mechanism of single-layer brazed CBN abrasive wheels during creep-feed grinding cast nickel-based superalloy. Int J Adv Manuf Tech 51(5):541–550
191. Ding W, Linke B, Zhu Y et al (2017) Review on monolayer CBN superabrasive wheels for grinding metallic materials. Chin J Aeronaut 30(1):109–134
192. Stetiu G, Lal G (1974) Wear of grinding wheels. Wear 30(2):229–236
193. Malkin S, Cook N (1971) The wear of grinding wheels: part 1—attritious wear. J Eng Ind 93(4): 1120-1128
194. Jackson M, Davis C, Hitchiner M et al (2001) High-speed grinding with CBN grinding wheels—applications and future technology. J Mater Process Tech 110(1):78–88
195. Klocke F, Brinksmeier E, Evans CJ et al (1997) High-speed grinding-fundamentals and state of the art in Europe, Japan, and the USA.
196. Liu SX, Liu MM, Liu TH et al (2023) Wear characteristics of brazing diamond abrasive wheel on high efficiency grinding ferrous metals. Wear 514/515:204580. https://doi.org/10.1016/j.wear.2022.204580
197. Yang HW, Feng W, Zhu JH et al (2021) Dynamics of CFRP grinding wheels and steel matrix grinding wheels in high-speed grinding process. Diamond Abrasives Eng 41(5):52–58
198. Yang L, Fu YC, Xu JH et al (2015) Structural design of a carbon fiber-reinforced polymer wheel for ultra-high speed grinding. Mater Design 88:827–836

Yu-Long Wang is a master of Qingdao University of Technology, China. His current research interests focus on intelligent and clean precision grinding.

Yan-Bin Zhang is a professor of Qingdao University of Technology. He is a Hong Kong Scholar from The Hong Kong Polytechnic University. He received his Ph.D. degree from Qingdao University of Technology in 2018. His current research interests focus on intelligent and clean precision manufacturing.

Xin Cui is an associate-professor of Qingdao University of Technology. She received her Ph.D. degree from Qingdao University of Technology in 2023. Her current research interests focus on intelligent and clean precision grinding.

Xiao-Liang Liang received his Ph.D. degree from the Ministry of Education's Key Laboratory of Efficient and Clean Machinery Manufacturing, School of Mechanical Engineering, Shandong University in March 2021. Mainly engaged in research on surface control technology and equipment for efficient and high-quality cutting of difficult-to-machine materials, and carried out work on high-quality and efficient cutting technology, tool wear assessment, material cutting performance, surface integrity and anti-fatigue manufacturing, etc.

Run-Ze Li received his B.S. degree in Biomedical Engineering from Huazhong University of Science and Technology, Wuhan, China in 2014, and M.S. degree in Biomedical Engineering from University of Southern California, Los Angeles, CA, in 2017. He received his Ph.D. degree at the Department of Biomedical Engineering of University of Southern California. His research interests include development of high frequency transducer, ultrasonic elastography and optical coherence elastography.

Ruo-Xin Wang received B.E. degree in mechanical design, manufacture and automation from the University of Shanghai for Science and Technology, Shanghai, in 2015. She received the M.E. degree in mechanical engineering from the Southwest Jiao University, Chengdu, in 2018. She is currently pursuing the Ph.D. degree with the Hong Kong Polytechnic University, Hong Kong, China. Her current research interests include machine learning-based surface characterization, smart measurement, and knowledge graph.

Shubham Sharma is a senior lecturer in the Department of Mechanical Engineering, IK Gujral Punjab Technical University. His current research interests focus on advances in mechanical engineering, industrial and production engineering, manufacturing technology, advanced materials science and various characterizations.

Ming-Zheng Liu is a associate-professor of Qingdao University of Technology. He received his Ph.D. degree from Qingdao University of Technology in 2023. His current research interests focus on intelligent and clean precision grinding.

Teng Gao is a doctor of Qingdao University of Technology, China. His current research interests focus on intelligent and clean precision grinding.

Zong-Ming Zhou is currently a Chairman of Hanergy (Qingdao) Lubrication Technology Co., Ltd.. He received his master's degree from Beihang University in 2021. The major is Information Engineering.

Xiao-Ming Wang is a doctor of Qingdao University of Technology, China. His current research interests focus on intelligent and clean precision grinding.

Yusuf Suleiman Dambatta received his Ph.D. degree from University of Malaya. His current research interests focus on manufacturing and precision machining.

Chang-He Li is a professor of Qingdao University of Technology. He is a special expert of Taishan Scholars in Shandong Province, China. He received his Ph.D. degree from Northeastern University, China, in 2006. His current research interests focus on intelligent and clean precision manufacturing.